UNIVERSITY OF OKLAHOMA

GRADUATE COLLEGE

SATELLITE-BASED CHARACTERIZATION OF CROP TYPE AND PRODUCTIVITY OF AGROECOSYSTEMS: CASE STUDIES IN NORTHEAST CHINA, SOUTHERN AFRICA, AND CONTERMINOUS USA

A DISSERTATION

SUBMITTED TO THE GRADUATE FACULTY

in partial fulfillment of the requirements for the

Degree of

DOCTOR OF PHILOSOPHY

By

CUI JIN
Norman, Oklahoma
2016

Downloaded from SHAREOK. Persistent Handle URL: https://hdl.handle.net/11244/34579

SATELLITE-BASED CHARACTERIZATION OF CROP TYPE AND PRODUCTIVITY OF AGROECOSYSTEMS: CASE STUDIES IN NORTHEAST CHINA, SOUTHERN AFRICA, AND CONTERMINOUS USA

A DISSERTATION APPROVED FOR THE
GRADUATE COLLEGE

BY

_____
Dr. Xiangming Xiao, Chair

_____
Dr. Jeffrey Basara

_____
Dr. Jinwei Dong

_____
Dr. Jean Steiner

_____
Dr. Heather McCarthy

© Copyright by CUI JIN 2016
All Rights Reserved.

This dissertation is dedicated to my husband Dr. Yu Wang, to my parents, and to my parents-in-law, for their unconditional love and support.

Acknowledgements

I would like to express my deepest gratitude to my advisor, Prof. Xiangming Xiao for his excellent guidance, caring, patience, and support during last five years of my Ph.D. study. I have been so fortunate to have an advisor who gave me the freedom to explore scientific questions. Without his supports, I couldn't have overcome so many difficult situations and finished my dissertation. In one day, I hope I would become as a good advisor as Dr. Xiao does.

I would also like to thank other members of my advisory committee, Prof. Jinwei Dong, Prof. Jean Steiner, Prof. Heather McCarty, and Prof. Jeffrey Basara, for all advices through the development of my dissertation research.

I extend my heartfelt thanks to all members of Prof. Xiao's lab, Prof. Jinwei Dong, Dr. Geli Zhang, Dr. Yuanwei Qin, Dr. Pradeep Wagle, Yuting Zhou, Jie Wang, Yao Zhang, Rajen Bajgain, and my friends Xuecheng Chen and Xiaodi Yu. Their friendship is my truly life treasure. We, like a big family, support and take care of each other.

I wish to express my thanks to my dear husband, Dr. Yu Wang. I could never have accomplished this dissertation without his love, support, and understanding. I am extremely grateful to my father Zhaoyi Jin, and my mother Fengying Zhang, who raised me and taught me to study hard and to give priority in my life to the quest for knowledge.

Last but certainly not least, I gratefully acknowledge research grants that made my Ph.D. work possible. I could not have gone through the doctoral program overseas without the financial support. I would like to express my full appreciation to the staffs of the Center for Spatial Analysis, especially Ms. Melissa Scott, and Ms. Leah Nash for their assistance.

Table of Contents

Acknowledgements iv

List of Tables x

List of Figures xii

Abstract xx

Chapter 1: Introduction 1

1.1 Research background 1

1.2 Overall research objectives 4

1.3 Organization of the dissertation 4

1.4 List of Publications from the Dissertation 5

Chapter 2: Mapping paddy rice distribution using multi-temporal Landsat imagery in the Sanjiang Plain, northeast China 7

Abstract 7

2.1 Introduction 7

2.2 Materials and methods 10

2.2.1 Study area 10

2.2.2 Landsat images and preprocessing 13

2.2.3 Algorithm for mapping paddy rice during the flooding/transplanting phase 15

2.2.4 Algorithm for mapping paddy rice during the ripening phase 16

2.2.5 Implementation of algorithms 19

2.2.6 Validation of the Landsat-based paddy rice map of the Sanjiang Plain 20

2.2.7 Comparison with other paddy rice datasets 21

2.3 Results 22
2.3.1 Maps of the flooding/transplanting phase of paddy rice 22
2.3.2 Maps of the ripening phase of paddy rice 24
2.3.3 Paddy rice map of the Sanjiang Plain and accuracy assessment 25
2.3.4 A comparison of the Landsat paddy rice map with the other paddy rice area estimate datasets 26
2.4 Discussion 28
2.5 Conclusion 31
Chapter 3: Phenology and gross primary production of two dominant savanna woodland ecosystems in Southern Africa 33
Abstract 33
3.1 Introduction 34
3.2 Materials and methods 37
3.2.1 Study sites 37
3.2.2 Site-specific meteorological data and CO_2 flux data 38
3.2.3 MODIS land surface reflectance, vegetation indices, and MODIS GPP products 41
3.2.4 The Vegetation Photosynthesis Model (VPM) 44
3.3 Results 46
3.3.1 Land surface phenology as delineated by CO_2 flux data and vegetation indices 46
3.3.2 Quantitative relationships between vegetation indices and GPP_{EC} 48

3.3.3 Seasonal dynamics of GPP from the Vegetation Photosynthesis Model (GPP_{VPM}) 50
3.4 Discussion 53
3.5 Conclusion 60
Chapter 4: Effects of in-situ and reanalysis climate data on estimation of cropland gross primary production using the Vegetation Photosynthesis Model 61
Abstract 61
4.1 Introduction 62
4.2 Data and methods 65
4.2.1 NARR 65
4.2.2 MODIS land surface reflectance, vegetation indices products 65
4.2.3 In-situ meteorological observations and CO_2 flux data 66
4.2.4 The Vegetation Photosynthesis Model (VPM) 69
4.2.5 Statistical analysis 70
4.3 Results 71
4.3.1 Comparison of air temperature 71
4.3.2 Comparison of downward shortwave radiation 75
4.3.3 Comparison of VPM-based (GPP_{VPM}) and the flux tower-based (GPP_{EC}) estimates 78
4.4 Discussion 85
4.4.1 Uncertainties of the NARR air temperature 85
4.4.2 Uncertainties of the NARR downward shortwave radiation 85
4.4.3 Sensitivity of PEMs to various climate inputs 87

4.4.4 Challenges in comparing GPP_{VPM} with GPP_{EC} 88
4.5 Conclusion 90
Supplementary materials 91
Chapter 5: The 2012 flash drought threatened the U.S. Midwest agroecosystems 92
Abstract 92
5.1 Introduction 93
5.2 Materials and methods 95
5.2.1 In-situ climate and CO_2 flux data from the AmeriFlux data 95
5.2.2 The regional data for the 2012 drought assessment 96
5.2.3 The regional data for GPP estimation of the Vegetation Photosynthesis Model (VPM) 97
5.2.4 Other regional datasets 98
5.2.5 Regional GPP estimation of the VPM 99
5.2.6 Data analysis 100
5.3 Results 101
5.3.1 Assessment of 2012 flash drought based on climate data 101
5.3.2 Impacts of droughts on the U.S. Midwest ecosystems at AmeriFlux sites 104
5.3.3 Impacts of droughts on the U.S. Midwest ecosystems at regional scale . 108
5.4 Discussion 115
5.4.1 The 2012 flash drought in the U.S. Midwest 115
5.4.2 Impacts of 2012 flash drought on the U.S. Midwest ecosystems 116
5.4.3 Challenges in terrestrial ecosystem models for agroecosystems 117

5.5 Conclusion 120

Supplementary materials 121

Chapter 6: Conclusions and perspectives 125

References 127

List of Tables

Table 2.1 A list of Landsat images collected for mapping the paddy rice distribution in the Sanjiang Plain, northeast China 13

Table 2.2 The threshold values as the inputs of rule-bases decision trees for the Landsat images during the rice ripening phase 18

Table 2.3 Accuracy assessment of the 30 m Landsat paddy rice map in the Sanjiang Plain, northeast China 26

Table 3.1 A summary description of the two savanna woodland flux tower sites 38

Table 3.2 Land surface phenology (leaf-on and Leaf-off dates) of the savanna woodland flux tower sites in Botswana and Zambia, as delineated by the estimated Gross Primary Production (GPP) data from the flux towers and a NIR/SWIR-based vegetation index (LSWI) 47

Table 3.3 A summary of gross primary production (GPP) estimated from the flux tower measurements (GPP_{EC}) and the predictions from the VPM model (GPP_{VPM}) at the savanna woodland flux tower sites in Botswana and Zambia. GPP_{EC}: seasonal sum of GPP estimated from the eddy covariance flux tower observations in g C m^{-2}, GPP_{VPM}: seasonal sum of GPP predicted by the VPM in g C m^{-2}, GPP%RE: relative error in GPP sums calculated as $[(GPP_{VPM} - GPP_{EC})/GPP_{EC}]\times100$, RMSD: Root Mean Squared deviation51

Table 4.1 A summary description of the AmeriFlux eddy flux crop sites 68

Table 4.2 Statistics of the comparison of the 8-day NARR air temperature, original, and adjusted downward shortwave radiation with the AmeriFlux observations for the individual crop sites 74

Table 4.3 A summary of the performances of the VPM driven by three sets of climate inputs at the crop sites 84

Table 5.1 Changes in climate, soil moisture, vegetation phenology, and seasonal CO_2 fluxes between 2012 and 2010–2014 mean at four AmeriFlux sites during the growing season 107

Table 5.2 Annual and total GPP estimates for each biome of the U.S. Midwest from 2010 to 2014 112

List of Figures

Figure 2.1(a) Geographic location of the Sanjiang Plain, northeast China; (b) location of all Landsat footprints, high-resolution images available on Google Earth, and ground truth pointes collected in 2011 12

Figure 2.2(a) Rice cropping calendar in the Sanjiang Plain; (b) rice transplanting stage (06/18/2013); (c) stem elongation stage (07/10/2013); (d) panicle initiation stage (07/21/2013); (e) mature stage (08/24/2011) 12

Figure 2.3 Workflow for mapping paddy rice distribution using the multi-temporal Landsat images 14

Figure 2.4 Seasonal dynamics of Landsat-based vegetation indices (NDVI, EVI, and LSWI) for typical land types 15

Figure 2.5 Statistic distribution of LSWI, NDVI, and (NDVI+EVI)/2-LSWI for paddy rice, dry cropland, forest, and built-up area on the 116/027-254/2011 (acc. represents accuracy)..... 17

Figure 2.6 (a)–(c), Landsat FCC images (R/G/B = SWIR /NIR/Red); (d)–(f), LSWI-EVI maps; (g)–(i), LSWI-NDVI maps; (j)–(l), flooding/transplanting rice maps for 114/027-176/2011, 114/028-176/2011, and 115/027-178/2012 23

Figure 2.7 (a)–(c), Landsat FCC images (R/G/B = LSWI / NDVI / (NDVI+EVI)/2-LSWI); (d)–(f), ripening rice maps for 116/027-254/2011, 114/028-264/2011, and 114/028-251/2012..... 24

Figure 2.8 (a) 30 m Landsat-based paddy rice map ($RICE_{Landsat}$); (b) 1 km^2 area fraction of paddy rice on the 2010 NLCD ($RICE_{NLCD}$); (c) 1 km^2 area fraction difference map between the $RICE_{Landsat}$ and the $RICE_{NLCD}$ 25

Figure 2.9 Classification accuracy based on POIs 26

Figure 2.10 (a) County-level comparison of paddy rice area estimates between the $RICE_{Landsat}$ and the $RICE_{NLCD}$; (b) county-level comparison of paddy rice area estimates between the $RICE_{Landsat}$ and the $RICE_{Census}$ 27

Figure 2.11 Evaluation of the discrepancy between the $RICE_{Landsat}$ and the $RICE_{NLCD}$: (a) and (c), the high-resolution images on Google Earth; (b) and (d), seasonal dynamics of 500 m MODIS vegetation indices (NDVI, EVI, LSWI) during 2000–2012..... 30

Figure 3.1 A simple illustration of the study sites, including (a) geo-locations of both savanna woodland flux sites in Botswana and Zambia; (b) landscapes at the Mongu site, Zambia, background image - Google Earth on 09/18/2005; (c) landscapes at the Maun site, Botswana, background image – Google Earth on 07/06/2011. The red square line in (b) and (c) corresponds to the size of a MODIS image pixel at 500-m spatial resolution, and the red dots represent the locations of the flux towers. The website http://eomf.ou.edu/visualization/gmap/ provides visualization of flux tower site locations and MODIS pixel boundary 38

Figure 3.2 Seasonal dynamics and interannual variations of precipitation (Precip), photosynthetically active radiation (PAR), soil water content at the upper 100 cm of soil (SWC), and air temperature (T_{air}) observed at the two savanna woodland flux sites in Africa. (a) Maun, Botswana, during 1999 - 2001; (b) Mongu, Zambia, during 2007 - 2009 39

Figure 3.3 Seasonal dynamics and interannual variations of observed net ecosystem exchange of CO_2 (NEE_{EC}) and estimated gross primary production (GPP_{EC}) at the two

savanna woodland sites, with the growing seasons highlighted. (a) the Maun site, Botswana, during 1999 - 2001; (b) the Mongu site, Zambia, during 2007 - 2009..... 40

Figure 3.4 Seasonal dynamics and interannual variations of three MODIS-derived vegetation indices at the two savanna woodland flux sites, with the growing seasons highlighted (a) the Maun site, Botswana, during 1999 - 2001; (b) the Mongu site, Zambia, during 2007 - 2009 43

Figure 3.5 The relationships between two vegetation indices (NDVI, EVI) and gross primary production (GPP_{EC}) during the vegetation growth season at the two savanna woodland flux sites. (a) and (b) the Maun site, Botswana, during 1999 - 2001; (c) and (d) Mongu, Zambia, Africa, during 2007 - 2009 49

Figure 3.6 Seasonal dynamics and interannual variations of gross primary production at the Maun site, Botswana, during 1999 – 2001, with the growing seasons highlighted. GPP_{EC} - estimated GPP from the flux tower data; GPP_{VPM} - predicted GPP from the VPM model 50

Figure 3.7 A comparison between GPP_{EC} and GPP_{VPM} at the Maun site, Botswana, during (a) 1999/2000, (b) 2000/2001..... 51

Figure 3.8 Seasonal dynamics and interannual variations of GPP_{EC} and GPP_{VPM} at the Mongu site, Zambia, during 2007-2009, with the growing seasons highlighted 52

Figure 3.9 Comparison between GPP_{EC} and GPP_{VPM} at the Mongu site, Zambia, during (a) 2007/2008, (b) 2008/2009..... 53

Figure 3.10 Sensitivity analysis of the VPM model at the Maun site, Botswana. It includes three cases of VPM simulations related to W_{scalar} and T_{scalar}: (1) without W_{scalar}, i.e., $\varepsilon_g = \varepsilon_0 \times T_{scalar}$; (2) without T_{scalar}, i.e., $\varepsilon_g = \varepsilon_0 \times W_{scalar}$; and (3) without both W_{scalar} and T_{scalar},

i.e., $\varepsilon_g = \varepsilon_{0.}$ (a) 1999/2000 season; (b) 2000/2001 season, (c) both 1999/2000 and 2000/2001 seasons. See also Table 4 for the slopes and R^2 values of individual simple linear regression models 56

Figure 3.11 Sensitivity analysis of the VPM model at the Mongu site, Zambia, including three cases of VPM simulations related to W_{scalar} and T_{scalar}: (1) without W_{scalar}, i.e., $\varepsilon_g = \varepsilon_0 \times T_{scalar} \times P_{scalar}$; (2) without T_{scalar}, i.e., $\varepsilon_g = \varepsilon_0 \times W_{scalar} \times P_{scalar}$; and (3) without both W_{scalar} and T_{scalar}, i.e., $\varepsilon_g = \varepsilon_0 \times P_{scalar}$. (a) 2007/2008 season; (b) 2008/2009 season, (c) both 2007/2008 and 2008/2009 seasons. See also Table 4 for the slopes and R^2 values of individual simple linear regression models 57

Figure 3.12 Comparison of GPP_{EC} and GPP_{VPM} as well as GPP derived from the MOD17A2 data product ($GPP_{MOD17A2}$). (a) the Maun site, Botswana, during 1999 - 2001; (b) the Mongu site, Zambia, during 2007 - 2009 59

Figure 4.1 Location of the AmeriFlux eddy flux sites. Circles denote the non-crop sites for accuracy assessment of the NARR and stars denote the crop sites used to evaluate the VPM-based GPP estimates. The base map is the 2013 Cropland Data Layer (CDL) from the National Agricultural Statistics Service (NASS)..... 67

Figure 4.2 Distribution histograms of correlation coefficient ($\boldsymbol{\rho}$), ratio of standard deviation ($\boldsymbol{\sigma ratio}$), bias, root-mean-square-error (RMSE), and regression coefficient (α) for 8-day air temperature from AmeriFlux (T_{EC}) and NARR (T_{NARR}) across the non-crop site-years..... 72

Figure 4.3 Contributions of correlation ($\boldsymbol{\rho}$), consistency of variation ($\boldsymbol{\sigma ratio}$), and bias to the Mean Squared Error (MSE) for the 8-day NARR air temperature (T_{NARR}) across the non-crop site-years 72

Figure 4.4 Comparisons of 8-day air temperature between AmeriFlux (T_{EC}) and NARR (T_{NARR}) across all crop site-years 73

Figure 4.5 Distribution histograms of correlation coefficient ($\boldsymbol{\rho}$), ratio of standard deviation ($\boldsymbol{\sigma ratio}$), bias, root-mean-square-error (RMSE), and regression coefficient (α) for 8-day downward shortwave radiation between AmeriFlux (R_{EC}) and NARR (R_{NARR}) across the non-crop site-years 75

Figure 4.6 Contributions of correlation ($\boldsymbol{\rho}$), consistency of variation ($\boldsymbol{\sigma ratio}$), and bias to the Mean Squared Error (MSE) for the 8-day NARR downward shortwave radiation (R_{NARR}) across the non-crop site-years..... 76

Figure 4.7 Spatial patterns of regression coefficient (α) between 8-day downward shortwave radiation from AmeriFlux (R_{EC}) and NARR (R_{NARR}), with geographical distribution of crop sites highlighted: (a) α averaged along the 2.5° latitude gradient and (b) α averaged along the 5° longitude gradient 77

Figure 4.8 Comparisons of 8-day downward shortwave radiation between AmeriFlux (R_{EC}) and the NARR before and after adjustment (R_{NARR}, $R_{adjNARR}$) for all crop site-years 77

Figure 4.9 Seasonal dynamics and interannual variations of GPP_{EC}, $GPP_{VPM(EC)}$, $GPP_{VPM(NARR)}$, and $GPP_{VPM(adjNARR)}$ for the crop site-years. The soybean site-years are highlighted..... 79

Figure 4.10 Comparisons of $GPP_{VPM(EC)}$, $GPP_{VPM(NARR)}$, and $GPP_{VPM(adjNARR)}$ with GPP_{EC} for individual crop: (a) irrigated maize, (b) rainfed maize, (c) irrigates soybean, and (d) rainfed soybean..... 81

Figure 4.11 Performances of the VPM driven by three climate datasets for individual crop-site: (a) and (b) $GPP_{VPM(EC)}$ vs. $GPP_{VPM(NARR)}$ and $GPP_{VPM(EC)}$ vs. $GPP_{VPM(adjNARR)}$ for the irrigated and rainfed maize; (c) and (d) $GPP_{VPM(EC)}$ vs. $GPP_{VPM(NARR)}$ and $GPP_{VPM(EC)}$ vs. $GPP_{VPM(adjNARR)}$ for the irrigated and rainfed soybean. The locations of the heads and tails of arrows quantify how GPP_{VPM} matches with GPP_{EC}, and the arrows show how the agreement of GPP_{VPM} with GPP_{EC} changes using different climate inputs. The distance to the origin is the ratio of the standard deviations of GPP_{VPM} and GPP_{EC} (Normalized standard deviation, $\boldsymbol{\sigma ratio}$). The azimuthal angle is the correlation ($\boldsymbol{\rho}$) showing the similarity of variation patterns between GPP_{VPM} and GPP_{EC}. The most ideal GPP_{VPM} estimate is the point "observed" with $\boldsymbol{\sigma ratio}$ = 1 and $\boldsymbol{\rho}$ = 1 83

Figure S4.1 Landscape analyses for seven crop sites. (a) - (g) are landscapes from the high-resolution Google Earth images; (h) - (n) are land cover maps from the 2011 Cropland Data Layer (CDL), which are crop classification maps derived from high-resolution (30 m or 56 m) satellite data. The polygons with red and blue outlines are 1 km and 500 m MODIS pixels covering flux towers, respectively 91

Figure 5.1 Land use and land cover map of the U.S. Midwest. Red circles represent AmeriFlux eddy covariance sites. Vegetation type is coded according to IGBP designations: ENF - evergreen needle forest, DBF - deciduous broadleaf forest, MF - mixed forest, GRA - grassland, CRO - cropland, and CRO/NVM - cropland/natural vegetation mosaic 96

Figure 5.2 Comparison of time series of 8-day average air temperature (a) and precipitation (b) from PRISM over the U.S. Midwest between a drought year of 2012 and the mean for 2010-2014 (excluding 2012). Vertical error bars indicate mean ± standard

deviation; shade areas represent 2012 anomalies relative to the mean values for 2010–2014 101

Figure 5.3 Spatial pattern of drought severity and climate anomalies during the 2012 growing season (May–September) over the U.S. Midwest. 1-month SPI mean and minimum (a and b, respectively), month of SPI minimum (c), anomalies of air temperature and total precipitation for the 2012 growing season relative to the mean values for 2010–2014 (d and e, respectively)..... 103

Figure 5.4 Observed climate, soil water content, and CO_2 fluxes at four AmeriFlux sites 106

Figure 5.5 Comparison of seasonal dynamics of the spatially averaged MODIS 8-day vegetation indices (NDVI, EVI, and LSWI), SIF, and GPP_{VPM} for six different biomes between a drought year of 2012 and the mean for 2010-2014 (excluding 2012). DOY: day of year. Red lines with markers represent 2012; black lines represent the 2010–2014 mean (excluding 2012), and vertical bars represent mean ± standard deviation; and shaded areas represent 2012 anomalies relative to the mean values for 2010–2014..... 109

Figure 5.6 Midwest-wide relative change rate (RCR, %) and response date of 8-day MODIS vegetation indices (NDVI, EVI, LSWI) and productivity (GPP_{VPM} and SIF) during a drought year of 2012 relative to the mean for 2010–2014 (excluding 2012?). RCR during April–June (AMJ, a), July–September (JAS, b), and growing season (GS, c). Response date to drought (d) - the first date when three 8-day composites in 2012 were continuously lower than the mean values for 2010–2014. The insets show the frequency histograms of RCR and response date..... 111

Figure 5.7 Relative change (%) of GPP_{VPM} and NASS yield statistics ($Yield_{NASS}$) over Midwest states for maize (a), soybean (b), and pasture/grassland (c). To avoid statistic errors in regions with sparse agriculture cultivation, analyses are limited to states where maize, soybean, or pasture/grassland account for > 20% of the total state area 114

Figure 5.8 Comparison of GOME-2 SIF and GPP estimates from three diagnostic models (VPM, MOD17, and MPI-BGC), and four process-based DGVMs (ORCHIDEE, JPL_GUESS, JPL, and VEGAS - as part of TRENDY project, http://dgvm.ceh.ac.uk/node/21) in July 2010 120

Figure S5.1 Seasonal dynamics of 8-day GPP at the AmeriFlux sites in the U.S. Midwest. US-Ne1, US-Ne2, US-Ne3, US-Ro1, US-Ro3, US-IB1, and US-Bo1 are CRO sites for maize and soybean (soybean was highlighted in grey); US-Syv is MF site; US-MMS, US-WCr, and US-UMB are DBF sites. GPP_{EC} - estimated GPP from in-situ eddy tower data; GPP_{VPM} - simulated GPP from the VPM 121

Figure S5.2 Scatter plot of biweekly SIF vs. GPP_{VPM} averaged for each biomes during 2010 – 2014 123

Figure S5.3 Spatial distribution of linear regression (R^2, slope, and intercept) between SIF and GPP_{VPM} and crop area fraction on 0.5 grid cell during 2010 – 2014..... 124

Abstract

Agroecosystem, or agricultural ecosystems, is the important anthropogenic ecosystem to meet the human demand for food, fiber, and feed, and it covers approximately 40-50% of the earth's land surface. Accurate estimates of agricultural land use and land cover and Gross Primary Production (GPP) are indispensable for global food security and understanding variations in the terrestrial carbon budgets. This dissertation aimed to strengthen the capacities of remote sensing to produce the high-quality products of crop type maps and primary productivity on large regional scales.

In chapter 2, we designed simple algorithms to identify paddy rice of two different phenological phases (flooding/transplanting and ripening) at regional scales using 30-m multi-temporal Landsat images. Sixteen Landsat images from 2010 - 2012 were used to generate the paddy rice map in the Sanjiang Plain, northeast China - one of the intensive paddy rice cultivation regions in Northern Asia. The user and producer accuracies of paddy rice on the resultant Landsat-based paddy rice map were 90% and 94%, respectively, and was an improvement over the paddy rice dataset derived through visual interpretation and digitalization on the fine-resolution satellite images and traditional agricultural census data.

Chapter 3 evaluated the capacities of the temporal MODIS vegetation indices and the satellite-based Vegetation Photosynthesis Model (VPM) to describe phenology and model the seasonal dynamics of GPP for savanna woodlands in Southern Africa on the site level. The results showed that the VPM-based GPP estimates tracked the seasonal dynamics and interannual variation of GPP estimated from eddy covariance measurements at flux tower sites. This study suggests that the VPM is a valuable tool for

estimating GPP of semi-arid and semi-humid savanna woodland ecosystems in Southern Africa.

Chapter 4 assessed the accuracies of air temperature and downward shortwave radiation of the North America Regional Reanalysis (NARR) by the National Centers for Environmental Prediction (NCEP), and evaluated impacts of the accuracies of regional climate inputs on the VPM-based GPP estimates for U.S. Midwest cropland. The results implied that the bias of NARR downward shortwave radiation introduced significant uncertainties into the VPM-based GPP estimates, suggesting that more accurate surface radiation datasets are needed to estimate primary production of terrestrial ecosystems at regional and global scales.

Chapter 5 presented independent and complementary analyses of the impact of 2012 flash drought on productivity in the U.S. Midwest using multiple sources of evidences, i.e., in-situ AmeriFlux CO_2 data, satellite observations of vegetation indices and solar-induced chlorophyll fluorescence (SIF), and scaled ecosystem modeling. The results showed that phenological activities of all biomes advanced 1-2 weeks earlier in 2012 compared to other years of 2010-2014, and the drought threatened the U.S. Midwest agroecosystems. The growth of grassland/prairie and cropland was suppressed from June and it didn't recover until the end of the growing season. As the frequency and severity of droughts have been predicted to increase in future, this study provides better insights into the impacts of flash droughts on vegetation productivity and carbon cycling of major biomes in the U.S. Midwest.

Chapter 1: Introduction

1.1 Research background

Agroecosystem, or agricultural ecosystems, is the important anthropogenic ecosystem to meet the human demand for food, fiber, and feed, and it covers approximately 40-50% of the earth's land surface (Fuhrer 2003). Meanwhile, it is a major driver of global environment change through altering land cover pattern and modifying terrestrial ecosystem structure and function (Ramankutty and Foley 1998; Spiegelaar and Tsuji 2013; Tilman et al. 2001). Agricultural land largely contributes to global greenhouse gas (GHG) emission, accounting for around 60% and 50% of anthropogenic N_2O and CH_4 emission, respectively (Smith et al. 2007). In addition, agricultural expansion results in biodiversity loss (Donald 2004), water resource shortage (Hanjra and Qureshi 2010), and soil erosion (Montgomery 2007). Efforts to address food security along with the impacts of agriculture on environment need the accurate geospatial datasets of agricultural land use and land cover (Monfreda et al. 2008; Ramankutty et al. 2008a).

The agroecosystem's role in the terrestrial carbon cycle is significant. A recent modeling study estimated a ~24% reduction in global vegetation carbon from agriculture (Alberte et al. 2007). However, carbon budget of cropland is still of great uncertainties due to different cultivation, and management practices, including biomass burning, residue removal, and crop-rotation, as well as soil erosion (Van Oost et al. 2007; West and Marland 2002). Gross Primary Production (GPP), the starting point of terrestrial ecosystem carbon, is the carbon uptake rate by terrestrial vegetation through photosynthesis (Suyker et al. 2005). Accurate estimates of GPP at canopy, ecosystem,

and landscape scales is imperative estimating agroecosystem carbon budgets and crop yield (Ciais et al. 2010; Moureaux et al. 2008; Zhangcai et al. 2012). The rate of photosynthesis at the chloroplast, leaf, and individual plant can be accurately measured using various instruments, such as potable photosynthesis system. However, how to scale up the estimates of GPP to the canopy and regional levels is still a challenging scientific question.

Remote sensing has become an increasingly attractive technology in classifying and mapping land use and land cover changes (LULCC). Especially, for large-scale (i.e. regional, continental, global) LULCC, remote sensing is a practical, efficient, and economical approach due to its consistency, reproducibility, and data coverage in regions where ground knowledge is limited (DeFries et al. 1995). Enormous efforts have been made by research communities to produce global LULCC products, such as global land cover database for the year 2000 (GLC2000) based on SPOT/Vegetation (Bartholome and Belward 2005), 1 km IGBP-DISCover (Loveland et al. 2000) and Global Land Cover Facility (GLCF) datasets from NOAA/AVHRR (Hansen et al. 2000), 1 km and 500 m MODIS land cover type products from MODIS/Terra and Aqua (Friedl et al. 2002). 30 m Finer Resolution Observation and Monitoring-Global Land Cover (FROM-GLC) from Landsat/ETM+ (Gong et al. 2013). However, the classification schemes of these LULUC datasets are either on biome-level or focus on the classification of natural land cover types, such as the types of forest and grassland, and define all crop types as one category.

Timely crop-based LULUC datasets are limited in the intense agricultural regions, e.g. Northern and Southeast Asia, where detailed information of crop types are needed as inputs for studies of food security and biogeochemical models. Recently, efforts have

been made to generate remote sensing-derived crop maps over these regions, including paddy rice maps (Xiao et al. 2002a; Xiao et al. 2006a; Xiao et al. 2005a), and maize, wheat, and cotton maps (Ren et al. 2008; Zhang et al. 2008a). The classification accuracy of these crop datasets, however, was questionable due to the mixed pixels, as these datasets were mostly derived from satellite data with coarse spatial resolution (500 m to 1 km). Thus, to obtain the fine-resolution and high-accuracy crop datasets using satellite data over large regions is still a challenging task.

Remote sensing has been a useful tool to scale up the estimates of GPP from individual leaves to canopy, ecosystem, and landscape scales via the Production Efficiency Models (PEMs), which are based on the principle of radiation-use efficiency (RUE) or light-use efficiency (LUE). A number of PEMs have been developed to estimate gross primary production with the use of satellite and climate data (Field et al. 1995; Potter et al. 1993; Prince and Goward 1995; Running et al. 1994; Xiao et al. 2004c), including the Global Production Efficiency Model (GLO-PEM) (Prince and Goward 1995), the Vegetation Photosynthesis Model (VPM) (Xiao et al. 2004a), the Terrestrial Uptake and Release of Carbon model (TRUC) (Ruimy et al. 1996), and the MODIS Daily Photosynthesis model (PSN) (Running et al. 2000b). The VPM is based on the conceptual partitioning of chlorophyll and non-photosynthetically active vegetation (NPV) in a canopy. It estimates GPP over the plant growing season at daily or weekly intervals. Studies have shown the capabilities of the VPM to model the GPP for rainfed and irrigated maize (Kalfas et al. 2011b; Wang et al. 2010b), soybean (Wagle et al. 2015), winter wheat (Yan et al. 2009), and grassland (Wagle et al. 2014; Wu et al. 2008) on in-

situ levels; thus, one hypnosis is that the VPM has the potential to simulate seasonal dynamic and interannual variation of the GPP for agroecoystems over regional scales.

1.2 Overall research objectives

The goal of this dissertation is to strengthen remote sensing's capacities to produce high-quality products of crop types and primary productivity on regional and global scales. Especially, I am interested in exploring the potential of the multi-temporal Landsat imagery for mapping specific crop type at the spatial resolution of 30 m. I am also interested in improving the large-scale crop GPP modeling with satellite-driven PEMs. My dissertation focuses on three largest commodity crops (paddy rice, corn, soybean) and two dominant savanna woodlands across the typical agroecosystems of Northeast China, Southern Africa, and conterminous USA.

1.3 Organization of the dissertation

This dissertation consists of one introductory chapter, four main chapters, and one summary chapter. Chapters 2, 3, 4 have been published on three peer-reviewed journals, and Chapter 5 will be submitted to one peer-reviewed journal.

Chapter 2 aims to develop simple and robust algorithms to generate 30-m paddy rice map on the regional scale. This chapter identifies the unique spectral or phenological signatures of paddy rice across the entire rice growth stages using the multi-temporal 30-m Landsat imagery, and develops the phenology-based and decision tree-based algorithms to classify paddy rice in the flooding/transplanting and ripening phases, respectively. The discussion focuses on the advantages and uncertainties of the resultant 30-m Landsat-based paddy rice map, and the potential application of the algorithms over the entire Northern Asia.

Chapter 3 is a site-level study to evaluate the capacities of the temporal MODIS vegetation indices and the VPM to describe phenology and model the GPP seasonal dynamics of savanna woodlands in Southern Africa. Two savanna woodland species across a precipitation gradient were chosen in order to assess the VPM robustness. Model accuracy, parameter sensitivity as well as the improvements of the VPM over other satellite-based PEMs are discussed.

Chapter 4 assesses the accuracies of climate variables from the North America Regional Reanalysis (NARR) by the National Centers for Environmental Prediction (NCEP), i.e. air temperature and downward shortwave radiation, which are two important model inputs of the VPM when simulating the GPP at regional and global scales. It also investigates the uncertainties in GPP estimates from the VPM from climate inputs at seven sites in the U.S. Midwest region as compared with eddy covariance-based GPP. This chapter highlights the importance of accurate surface radiation datasets to estimate primary production of terrestrial ecosystems at regional and global scales.

Chapter 5 develops the strategy to accurately model GPP over the U.S. Midwest, one of the most intense agricultural regions in the world. On the basis of regional GPP modeling, another objective is to quantify the impacts of 2012 flash drought on phenology, greenness and productivity of major biomes in the U.S. Midwest.

1.4 List of Publications from the Dissertation

Chapter 2

Jin, C., Xiao, X., Dong, J., Qin, Y., & Wang, Z. (2015). Mapping paddy rice distribution using multi-temporal Landsat imagery in the Sanjiang Plain, northeast China. Frontiers of Earth Science, 10, 49-62.

Chapter 3

Jin, C., Xiao, X.M., Merbold, L., Arneth, A., Veenendaal, E., & Kutsch, W.L. (2013). Phenology and gross primary production of two dominant savanna woodland ecosystems in Southern Africa. Remote Sensing of Environment, 135, 189-201.

Chapter 4

Jin, C., Xiao, X.M., Wagle, P., Griffis, T., Dong, J.W., Wu, C.Y., Qin, Y.W., & Cook, D.R. (2015). Effects of in-situ and reanalysis climate data on estimation of cropland gross primary production using the Vegetation Photosynthesis Model. Agricultural and Forest Meteorology, 213, 240-250.

Chapter 5

Jin, C., Xiao, X.M., Zhang, Y., Wagle, P., Dong, J.W., Steiner J., & Basara, J.. (2016). The 2012 flash drought threatened the U.S. Midwest agroecosystems. (to be submitted)

Chapter 2: Mapping paddy rice distribution using multi-temporal Landsat imagery in the Sanjiang Plain, northeast China

Abstract

Information of paddy rice distribution is essential for food production and methane emission calculation. Phenology-based algorithms have been utilized in the mapping of paddy rice fields by identifying the unique flooding and seedling transplanting phases using multi-temporal moderate resolution (500 m to 1 km) images. In this study, we developed simple algorithms to identify paddy rice at a fine resolution at the regional scale using multi-temporal Landsat imagery. Sixteen Landsat images from 2010 - 2012 were used to generate the 30 m paddy rice map in the Sanjiang Plain, northeast China - one of the major paddy rice cultivation regions in China. Three vegetation indices, Normalized Difference Vegetation Index (NDVI), Enhanced Vegetation Index (EVI), and Land Surface Water Index (LSWI), were used to identify rice fields during the flooding/transplanting and ripening phases. The user and producer accuracies of paddy rice on the resultant Landsat-based paddy rice map were 90% and 94%, respectively. The Landsat-based paddy rice map was an improvement over the paddy rice layer on the National Land Cover Dataset, which was generated through visual interpretation and digitalization on the fine-resolution images. The agricultural census data substantially underreported paddy rice area, raising serious concern about its use for studies on food security.

2.1 Introduction

Rice is the world's second-largest crop and is a major food staple, feeding more than half of the world's population (Nguyen and Ferrero 2006). It plays an important role

in ensuring global food security. Global rice consumption has been predicted to exceed rice production (Kuenzer and Knauer 2013). Approximately 95% of global rice is cultivated on flooded soil (Belder et al. 2004). Irrigation for rice cultivation requires large amounts of water and has an important impact on water quality. In addition, rice fields are one of the main sources of greenhouse gas emissions (Li et al. 2004). Therefore, accurate high-resolution maps of paddy rice distribution are critical for food production, water management, agriculture migration, and agriculture adaption under global climate change (Doll 2002).

Remote sensing is an efficient tool for generating paddy rice maps. The potentials of fine-resolution satellite imagery, such as 20 m SPOT and 30/79 m Landsat, for classifying paddy rice fields have been explored (Laba et al. 1997; McCloy et al. 1987; Okamoto and Fukuhara 1996; Okamoto et al. 1998; Panigrahy and Parihar 1992; Turner and Congalton 1998). Single images were typically used in earlier studies due to the limited availability of satellite imagery. Rice fields were visually interpreted from color composite images, and their boundaries were then artificially digitalized onscreen (Liu et al. 2005; Qiu et al. 2003; Rao and Rao 1987). Other studies used the supervised or unsupervised classification algorithms to identify the spectral cluster of paddy rice (Laba et al. 1997; Okamoto et al. 1998; Panigrahy and Parihar 1992; Turner and Congalton 1998). However, the application of these two approaches at regional or national scales is often labor-intensive and time-consuming. Changes in research personnel and methods over time make it particularly difficult to obtain consistent classification results in the projects that analyze multiple-year images.

The Moderate Resolution Imaging Spectroradiometer (MODIS) provides global coverage of imagery every 1- 2 days at 250 m, 500 m, and 1 km, and is free to the public. The phenology-based algorithm developed on the multi-temporal MODIS data has shown a great potential for tracking the dynamics of the vegetation-to-water ratio during the rice growth, and can consistently map the annual paddy rice distribution at regional scales (Biradar and Xiao 2011; Sakamoto et al. 2006; Sakamoto et al. 2009; Xiao et al. 2006a; Xiao et al. 2005a). However, the accuracy of the MODIS phenology-based paddy rice maps was still questionable due to the mixed pixels caused by the coarse spatial resolution; a problem especially relevant in Asia, with over 200 million smallholding farms, typically under 1 hectare (Sun et al. 2009; Xiao et al. 2006a). One solution is the use of multi-temporal high-resolution imagery (Xiao et al. 2006a).

The United States Geological Survey (USGS) Earth Resources Observation and Science (EROS) Center has offered free historical and new Landsat imagery to the public since 2008. This provided a great opportunity for regional-scale land cover classification. One significant accomplishment was the capability to track forest cover dynamics by using multi-temporal Landsat imagery (Hansen et al. 2013). Some studies tracked the continuous dynamics of spectral features derived from all available Landsat imagery across multi-years to identify forest and forest disturbance (Huang et al. 2010a; Masek et al. 2008; Zhu et al. 2012). Several others extracted the annual trajectory of image features from yearly Landsat imagery, such as using one image within the peak of the annual growing season (Cohen et al. 2010; Kennedy et al. 2010). Another study evaluated the spectral features of the forest during different phenological phases, then screened the

specific phases when the forest showed spectral features that were distinguishable from other land types (Dong et al. 2013).

The potential of multi-temporal Landsat imagery to monitor crops has been underestimated due to their spectral and phenological variability features (Zhong et al. 2014). Recent studies have highlighted the capability of intra-annual Landsat to identify corn and soybean (Zhong et al. 2014). Therefore, we hypothesize that paddy rice distribution mapping will benefit from the phenological features captured by multi-temporal Landsat imagery. We examined if single dates of phenological or spectral characteristics from the Landsat imagery with low-observation frequency could be extracted for paddy rice. For example, could multi-temporal Landsat imagery track the dynamics of the vegetation-to-water ratio for rice fields similarly to the use of MODIS data?

The objective of this study is to: (i) develop the Landsat phenology-based scheme to identify paddy rice fields during two phenological (flooding/transplanting and ripening) phases at regional scales, and (ii) systematically evaluate the accuracy and uncertainties of the resultant Landsat-based paddy rice map.

2.2 Materials and methods

2.2.1 Study area

The Sanjiang Plain is located in the northeast region of Heilongjiang Province, China (132.14°E–133.94°E, 45.37°N–46.61°N). It covers 23 counties with a total area of 10.88×10^4 km^2. Approximately 80% of the Sanjiang Plain is relatively flat with an elevation < 200 m (Figure 2.1(a)). The plain is characterized by a temperate and sub-humid continental monsoon climate, with a mean annual precipitation of 500 - 650 mm,

the majority of which falls between July and September. The mean monthly temperature varies from –18°C in January to 22 °C in July. The typical land cover types were cropland, woodland, and natural wetland, accounting for 55.2%, 30.3%, and 7.4% of the entire area, respectively (Huang et al. 2010b).

The abundant water resources and fertile soils, along with the flat topography, make the Sanjiang Plain favorable for paddy rice cultivation. Rice cultivation is relatively identical across the entire Sanjiang Plain. One rice crop per year is cultivated in this region with a rice growth cycle duration of approximately 140 - 150 days (Figure 2.2(a)). From mid-April to early May, rice fields are prepared by plowing, overturning, flooding, and leveling. In mid- to late May, rice seedlings are transplanted to flooded fields. During these two phases, rice fields are mostly dominated by water (Figure 2.2(b)). Rice canopy starts to rise rapidly during the vegetative growing phase (tillering and stem elongation) from mid-June to early July (Figure 2.2(c)), resulting in changes of the vegetation-to-water ratio. The reproductive phase starts in mid-July (panicle initiation, Figure 2.2(d)), the vegetation-to-water ratio reaches its maximum value in late July, and then remains stable or slightly decreases during the ripening phase from late August to September (Figure 2.2(e)). Rice is harvested from late September to early October.

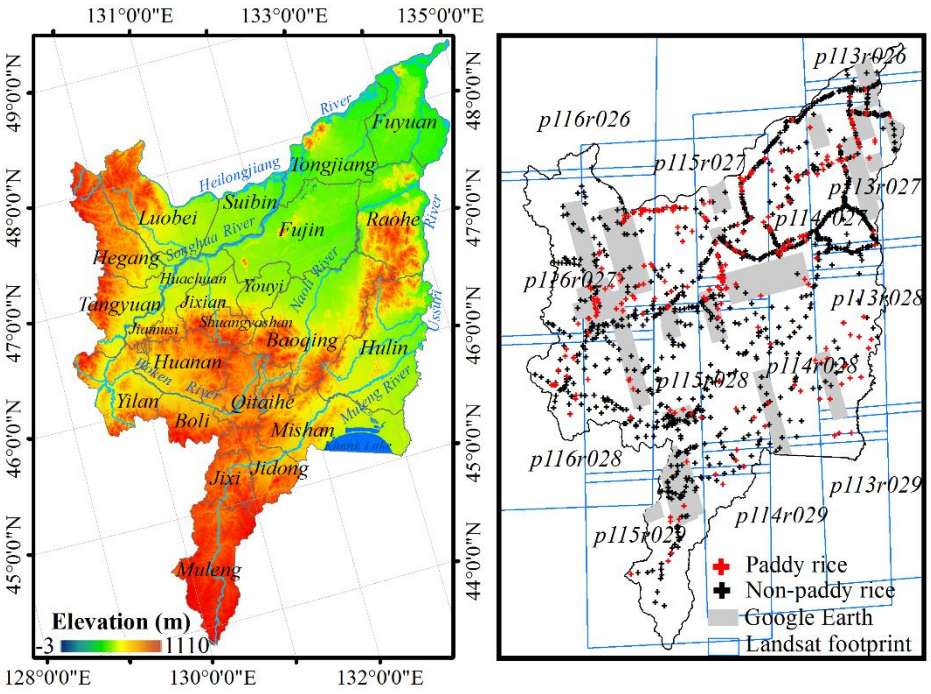


Figure 2.1(a) Geographic location of the Sanjiang Plain, northeast China; (b) location of all Landsat footprints, high-resolution images available on Google Earth, and ground truth pointes collected in 2011

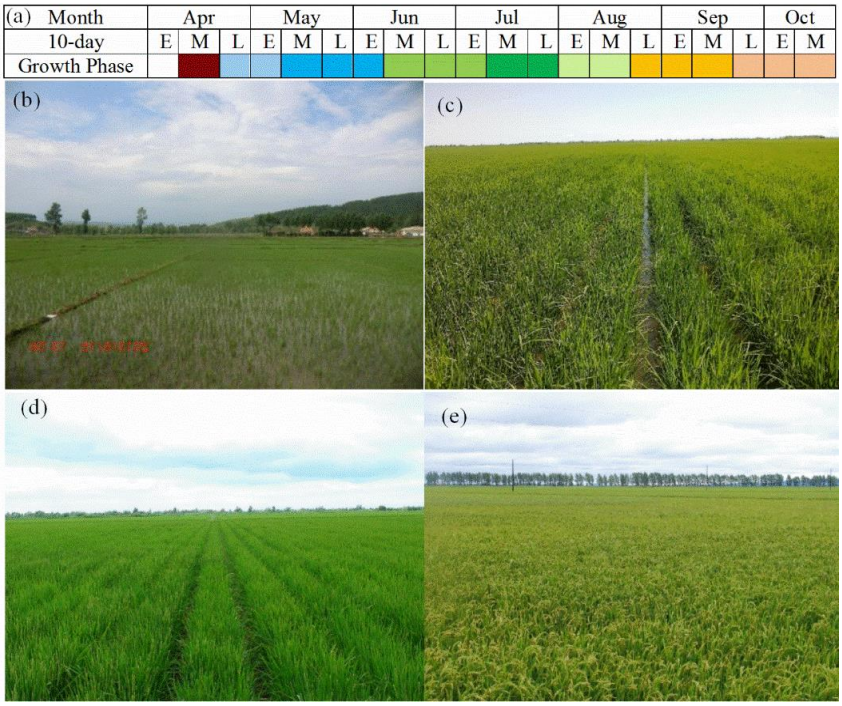


Figure 2.2(a) Rice cropping calendar in the Sanjiang Plain; (b) rice transplanting stage (06/18/2013); (c) stem elongation stage (07/10/2013); (d) panicle initiation stage (07/21/2013); (e) mature stage (08/24/2011)

2.2.2 Landsat images and preprocessing

The Sanjiang Plain is covered by 13 Landsat footprints (Figure 2.1(b)). 119 L1T Landsat images from 2010 - 2012 were collected from http://landsat.usgs.gov/ and were used to extract the multi-temporal curves of the Landsat vegetation indices for typical land cover types. Sixteen images were eventually used to generate the paddy rice map after examining three criteria (Table 2.1): (1) image acquisition date was during the peak of the transplanting/flooding and ripening phases when paddy rice showed the distinguishably phenological or spectral features from other land types; (2) cloud coverage was less than 5%; and (3) the gap-filling strategy (see Section 2.5).

Table 2.1 A list of Landsat images collected for mapping the paddy rice distribution in the Sanjiang Plain, northeast China

Path/Row	Sensor	Date	Year	Cloud/%	Rice growing phase
113/026	TM	September-19	2011	0	Ripening
113/027	TM	September-19	2011	0	Ripening
114/027	TM	June-25	2011	1	Transplanting
	TM	June-06	2010	0	Transplanting
	TM	June-25	2011	0	Transplanting
114/028	ETM+	September-21	2011	0	Ripening
	ETM+	September-07	2012	0	Ripening
114/029	TM	June-25	2011	0	Transplanting
115/027	ETM+	August-27	2011	0	Ripening
	ETM+	June-26	2012	0	Transplanting
115/028	ETM+	September-12	2011	0	Ripening
	ETM+	September-09	2010	1	Ripening
115/029	ETM+	August-27	2011	3	Ripening
	ETM+	June-26	2012	0	Transplanting
116/027	TM	September-11	2011	0	Ripening
116/028	TM	September-11	2011	0	Ripening

All images were first processed for atmospheric correction and converted to surface reflectance using the Landsat Ecosystem Disturbance Adaptive Processing System □LEDAPS) (Figure 2.3) (Masek et al. 2008; Vermote et al. 1997). Masks for

clouds, cloud shadows, clear water, and data gaps due to Landsat 7 ETM+ SLC-off (Scan Line Corrector failed) were created for each Landsat scene using the object-based cloud and cloud shadow algorithm, Fmask (Zhu and Woodcock 2012).

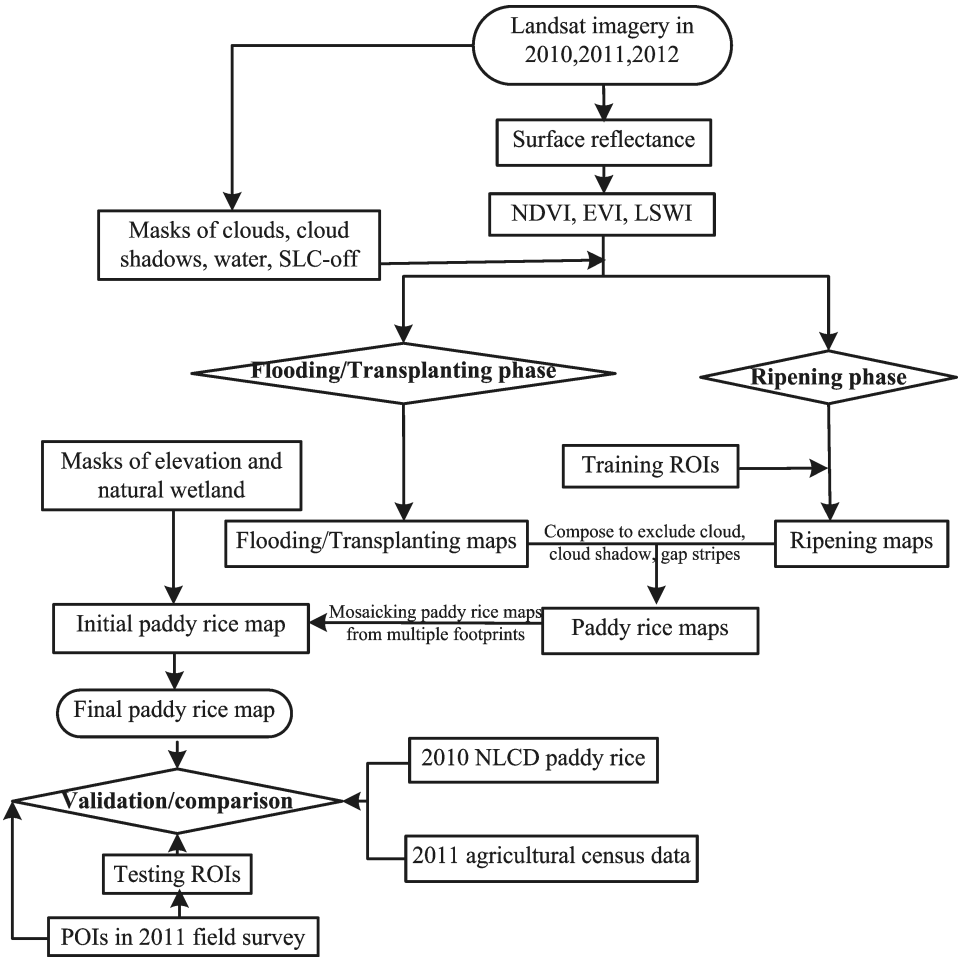


Figure 2.3 Workflow for mapping paddy rice distribution using the multi-temporal Landsat images

Three vegetation indices were calculated using surface reflectance (ρ) from the blue (B1), red (B3), NIR (B4), and SWIR (B5) bands: (1) Normalized Difference Vegetation Index (NDVI) (Tucker 1979b), (2) Enhanced Vegetation Index (EVI) (Huete et al. 2002; Huete et al. 1997a), and (3) Land Surface Water Index (LSWI) (Xiao et al. 2004a).

$$NDVI = \frac{\rho_{B4} - \rho_{B3}}{\rho_{B4} + \rho_{B3}} \tag{2.1}$$

$$EVI = \frac{\rho_{B4} - \rho_{B3}}{\rho_{B4} + 6 \times \rho_{B3} - 7.5 \times \rho_{B2} + 1} \tag{2.2}$$

$$LSWI = \frac{\rho_{B4} - \rho_{B5}}{\rho_{B4} + \rho_{B5}} \tag{2.3}$$

2.2.3 Algorithm for mapping paddy rice during the flooding/transplanting phase

We first chose one ground truth point for each land type, which was collected during the 2011 field investigation. Three vegetation indices were then extracted from multi-temporal Landsat imagery from 2010–2012 for the pixel where the ground truth point was located (Figure 2.4). Paddy rice showed a unique inversion between LSWI and EVI (NDVI) during the flooding/transplanting period: LSWI was substantially higher than EVI (NDVI) during early May and late June. Thus, a pixel was paddy rice when the condition LSWI + 0.05 > EVI (NDVI) was met in the flooding/transplanting phase. This was consistent with the MODIS phenology-based algorithm (Xiao et al. 2006a; Xiao et al. 2005a).

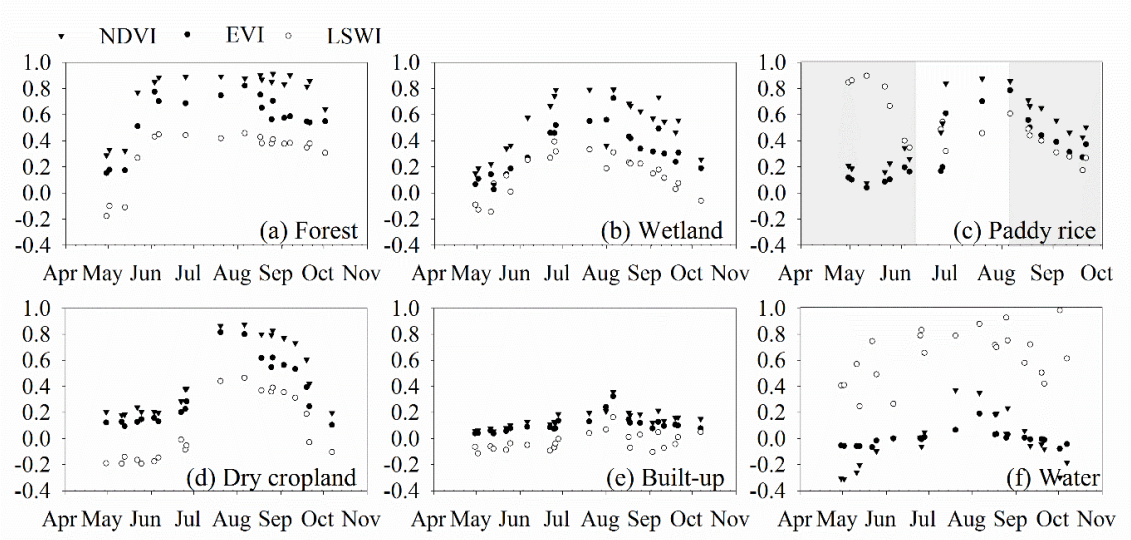


Figure 2.4 Seasonal dynamics of Landsat-based vegetation indices (NDVI, EVI, and LSWI) for typical land types

2.2.4 Algorithm for mapping paddy rice during the ripening phase

Paddy rice also showed unique features during the ripening phase (Figure 2.4). From late August to late September, forest NDVI remained high (around 0.8). However, paddy rice NDVI fell below 0.8 (Figure 2.4(a) vs. 2.4(c)). Built-up had much lower LSWI (around 0) than did paddy rice (> 0.2) (Figure 2.4(c) vs. 2.4(e)). Paddy rice had smaller differences between EVI (NDVI) and LSWI. Thus, the rule-based decision trees were deployed on LSWI, NDVI, and (NDVI+EVI)/2-LSWI to map the ripening paddy rice. Here the image on the 254th day in 2011 for path/row=116/027 (116/027-254/2011) was used as an example to illustrate the procedures to build the decision rules and determine the optimal threshold values.

Step 1 Selection of training regions of interest (ROIs): Homogenous ROIs were visually interpreted and digitalized on the Landsat false color composite (FCC) image of LSWI, NDVI, and (NDVI+EVI)/2-LSWI for paddy rice (22 ROIs with 1,077 pixels), dry cropland (22 ROIs with 1,077 pixels), forest (44 ROIs with 974 pixels), and built-up and bare land (21 ROIs with 989 pixels).

Step 2 Evaluation of ROI separability: The Jeffries-Matusita (J-M) distances of the ROI pairs between paddy rice and other land types were calculated (John A. Richards and Jia 1999). All J-M distances were above 1.9, which suggested that paddy rice had great separability from other land types using the training ROIs collected from the Landsat FCC image.

Step 3 Statistical distribution of ROIs: Paddy rice showed distinguishable statistical distributions (Figure 2.5). The built-up and bare land LSWI ranged from –0.2 to 0.2 and was significantly lower than paddy rice (Figure 2.5(a)). The forest NDVI was above 0.7,

much higher than paddy rice (Figure 2.5(b)). The paddy rice (NDVI+EVI)/2-LSWI ranged below 0.2 and was lower than dry cropland.

Step 4 Determination of the optimal thresholds: The optimal thresholds were calculated using regression trees from the training ROIs: Tbuilt-up/bare-land=0.2682 for LSWI, Tforest=0.6849 for NDVI, and Tdry-cropland=0.2219 for (NDVI+EVI)/2-LSWI.

Step 5 Implementation of the decision rules: the decision rules and threshold values were deployed on LSWI, NDVI, and (NDVI+EVI)/2-LSWI.

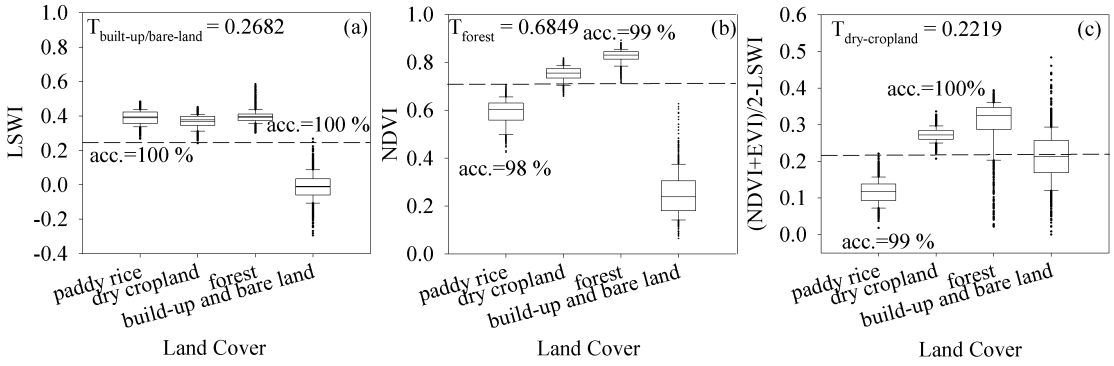


Figure 2.5 Statistic distribution of LSWI, NDVI, and (NDVI+EVI)/2-LSWI for paddy rice, dry cropland, forest, and built-up area on the 116/027-254/2011 (acc. represents accuracy).

The steps above were implemented on the Landsat images during the ripening phase. The threshold values were calculated using regression trees in R Project, Version 3.0.1 with a prediction accuracy above 95% (Table 2.2).

The algorithm robustness was evaluated by the accuracy assessment for three Landsat scenes (116/027-254/2011, 114/028-264/2011, and 114/028-251/2012), which covered the main paddy rice cultivation region. For 116/027-264/2011, a total number of 1,541 testing ROIs (24,656 pixels) was randomly generated within the subset region covered by the WorldView-2. As for 114/028-251/2012, 2,915 ROIs were randomly generated. 285 ROIs (167 for non-paddy rice and 118 for paddy rice) and 2,630 ROIs

(2,068 for non-paddy rice and 567 for paddy rice) were visually interpreted and digitalized onscreen from the high resolution images on Google Earth and the Landsat FCC image of 114/028-155/2012 (R/G/B=SWIR/NIR/Red), respectively. We used the same-year flooding/transplanting rice map (114/028-176/2011) as the ground truth reference to evaluate the accuracy of the ripening rice map on 114/028-264/2011. The accuracy assessment was summarized by the error matrixes along with user accuracy, producer accuracy, overall accuracy, and KAPPA coefficient for the ripening rice maps (Congalton, 1991).

Table 2.2 The threshold values as the inputs of rule-bases decision trees for the Landsat images during the rice ripening phase

Landsat Image	Path/Row	Date	Image Features	Threshold
113/027-262/2010	113/027	09/19/2010	LSWI	0.1158
113/026-262/2010	113/026		NDVI	0.7057
			(NDVI+EVI)/2-LSWI	0.2541
114/028-264/2011	114/028	09/21/2011	LSWI	0.2035
			NDVI	0.6692
			(NDVI+EVI)/2-LSWI	0.2081
114/028-251/2012	114/028	09/07/2012	LSWI	0.2702
			NDVI	0.7639
			(NDVI+EVI)/2-LSWI	0.2918
115/027-239/2011	115/027	08/27/ 2011	LSWI	0.3422
			NDVI	0.8137
			(NDVI+EVI)/2-LSWI	0.2327
115/028-255/2011	115/028	09/12/2011	LSWI	0.1984
			NDVI	0.7518
			(NDVI+EVI)/2-LSWI	0.2368
115/028-252/2010	115/028	09/09/2010	LSWI	0. 2010
			NDVI	0.7090
			(NDVI+EVI)/2-LSWI	0.2566
115/029-239/2011	115/029	08/27/2011	LSWI	0.3371
			NDVI	0.8339
			(NDVI+EVI)/2-LSWI	0.2721
116/027-254/2011	116/027	09/11/2011	LSWI	0.2682
116/028-254/2011	116/028		NDVI	0.6849
			(NDVI+EVI)/2-LSWI	0.2219

2.2.5 Implementation of algorithms

The field surveys were carried out in 2011, thus it was used as the baseline year. Images in 2010 and 2012 were used to fill the gaps caused by clouds, cloud shadows, or Landsat 7 ETM+ SLC-off in the 2011 images. For each Landsat footprint, we assembled the flooding/transplanting and ripening paddy rice maps into one paddy rice map using the following rule: the 2011 flooding/transplanting map was the initial input. If the 2011 flooding/transplanting map wasn't available or if it contained data gaps, the gaps were filled using the first available rice map in the order of: 1) the 2011 ripening rice map, 2) the 2010 flooding/transplanting map, 3) the 2010 ripening rice map, 4) the 2012 flooding/transplanting map, and 5) the 2012 ripening rice map. Finally, the paddy rice maps for 13 Landsat footprints were mosaicked into one preliminary paddy rice map for the Sanjiang Plain.

The final Landsat rice map was generated by excluding the natural wetland and unsuitable terrain regions for rice cultivation. The 30 m Landsat-based natural wetland dataset, provided by the Northeast Institute of Geography and Agricultural Ecology, Chinese Academy of Sciences, includes six natural wetland types: river, lake, flooding wetland, forested wetland, shrub wetland, and grassland wetland. The overall accuracy of natural wetland was above 90% (Xie 2013). As paddy rice in the Sanjiang Plain is generally cultivated in the low-elevation region, a terrain mask was generated to exclude regions with an elevation > 150 m for the low-latitude region and > 500 m for the high-latitude region using the 30 m ASTER Global Digital Elevation Model (DEM) (http://earthexplorer.usgs.gov/).

2.2.6 Validation of the Landsat-based paddy rice map of the Sanjiang Plain

Extensive field surveys were carried out to collect the ground truth points (points of interest, referred as POIs) across the Sanjiang Plain in 2011. The geo-locations of POIs were recorded using a GPS device with a position precision of 3 - 5 m. There were 240 POIs for paddy rice and 993 POIs for the other land cover types collected (487 POIs for dry cropland, 32 POIs for grassland, 90 POIs for natural wetland, 264 POIs for forest, 89 POIs for built-up, 29 POIs for water, and 2 POIs for other land cover types) (Figure 2.1(b)).

In this study, the resultant 30 m Landsat-based paddy rice map ($RICE_{Landsat}$) was evaluated using three approaches. The first approach used a point (POI) to one pixel comparison. We overlaid the 1,233 POIs on the $RICE_{Landsat}$ and counted the number of pixels that were classified as paddy rice and other land cover types, respectively. Note that some POIs were collected along the edges of the fields or on the roads; these pixels were typically mixed with multiple land types. Thus, there could be classification errors for the POIs on the $RICE_{Landsat}$. To overcome the issue, the second approach was to generate four buffering windows (15 m × 15 m, 30 m × 30 m, 45 m × 45 m, and 60 m × 60 m) with the POI as the centers. 60 m was defined as the maximum buffering distance considering the farthest observation range during the field survey and the maximum distance among the rice field plots. We overlaid the buffering windows on the $RICE_{Landsat}$, and counted the numbers of POIs of both paddy and non-paddy rice that had been correctly identified from the $RICE_{Landsat}$ under the two standards. In the first, a paddy rice POI was correctly identified as long as a $RICE_{Landsat}$ paddy rice pixel occurred within the buffering window. In the second, a non-paddy rice POI was correctly identified once all

the $RICE_{Landsat}$ pixels within the buffering window were identified as non-paddy rice. The third approach was to digitalize ROIs with the POIs as references. For each POI, we generated a ROI with an average area of 120 m × 120 m from the high-resolution imagery of Google Earth (Figure 2.1(b)) or Landsat FCC images (R/G/B=SWIR/NIR/Red) in late June as ground truth reference maps, on which paddy rice had either distinguishable spatial features or spectral patterns from other land types. 65 ROIs (1,052 pixels) of paddy rice and 227 ROIs (3,684 pixels) of other land cover types were collected from Google Earth from 2010–2012. 175 ROIs (2,730 pixels) of paddy rice and 766 ROIs (12,216 pixels) of other land cover types were interpreted from Landsat FCC images. The error matrix was calculated by overlaying ROIs on the $RICE_{Landsat}$.

2.2.7 Comparison with other paddy rice datasets

The National Land Cover Dataset (NLCD) is a 30 m vector database using a hierarchical classification scheme of 25 land-cover types. The NLCD was developed by visual interpretation and artificial digitalization from Landsat imagery (the primary base maps) at a scale of 1:100,000. Since the NLCD is only available to the public as areal fraction at 1 km resolution for each land type, we aggregated our $RICE_{Landsat}$ to a 1 km grid and compared it with the 2010 NLCD paddy rice ($RICE_{NLCD}$).

In addition, we collected the agriculture census records of rice cultivation area for 17 counties from the agricultural statistical yearbooks of Shuanyashan City, Qitaihe City, Jixi City, and Jiamusi City in 2011 ($RICE_{Census}$). We compared the county-level rice area between the $RICE_{Landsat}$ and the $RICE_{Census}$.

2.3 Results

2.3.1 Maps of the flooding/transplanting phase of paddy rice

Paddy rice showed as dark green across the Landsat FCC images (R/G/B=SWIR/NIR/Red) after two weeks of seedling transplanting in late June of 2011 and 2012, and was easily identified from other land types (Figures 2.6(a)–6(c)). The LSWI-EVI maps highlighted the spatial distribution of the rice fields under the flooding/transplanting phase (Figures. 2.6(d)–2.6(f)). The pixels with LSWI-EVI> –0.05 primarily represented the spatial pattern of paddy rice. However, the LSWI-NDVI was not as sensitive as LSWI-EVI; LSWI-NDVI of paddy rice was close to that of non-paddy rice (Figures. 2.6(g)–2.6(i)). The spatial distribution of paddy rice on the resultant maps (Figures. 2.6(j)–2.6(l)) corresponded well with the spatial pattern of paddy rice on the Landsat FCC images (Figures. 2.6(a)–2.6(c)).

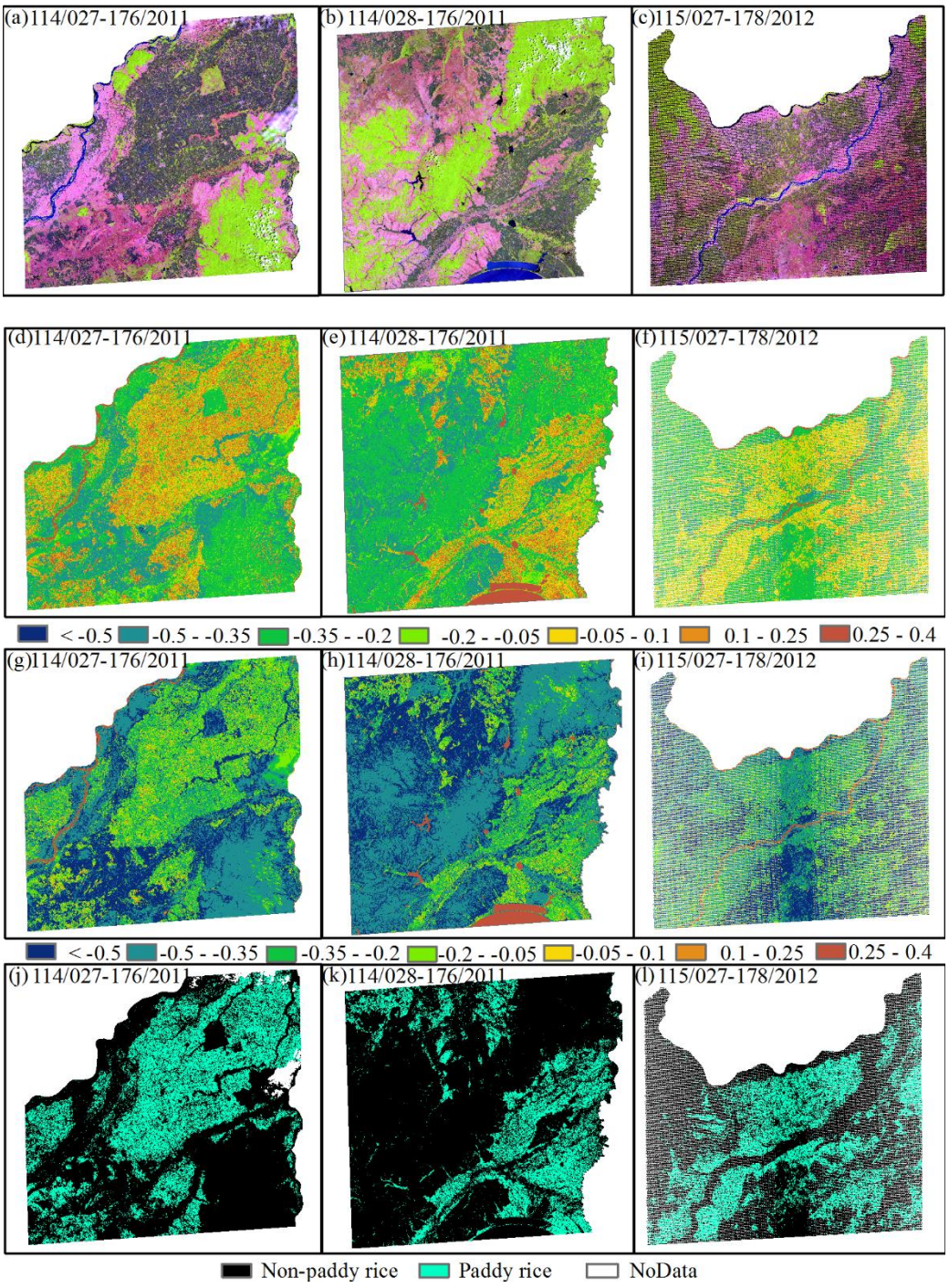


Figure 2.6 (a)–(c), Landsat FCC images (R/G/B = SWIR /NIR/Red); (d)–(f), LSWI-EVI maps; (g)–(i), LSWI-NDVI maps; (j)–(l), flooding/transplanting rice maps for 114/027-176/2011, 114/028-176/2011, and 115/027-178/2012

2.3.2 Maps of the ripening phase of paddy rice

The paddy rice distribution on the resultant maps (Figures. 2.7(d)–2.7(f)) were spatially consistent with the pattern of paddy rice on the Landsat FCC images (Figures. 2.7(a)–2.7(c)) on which paddy rice showed as orange tone, and was distinguishable from other land types. The ripening rice maps for 114/028-264/2011 and 114/028-251/2012 had high classification accuracies. The overall accuracies and KAPPA coefficients were 95% and 92% for 114/028-264/2011, and 96% and 91% for 114/028-251/2012. The user and producer accuracies were mostly above 90% for paddy rice and 95% for non-paddy rice on both maps.

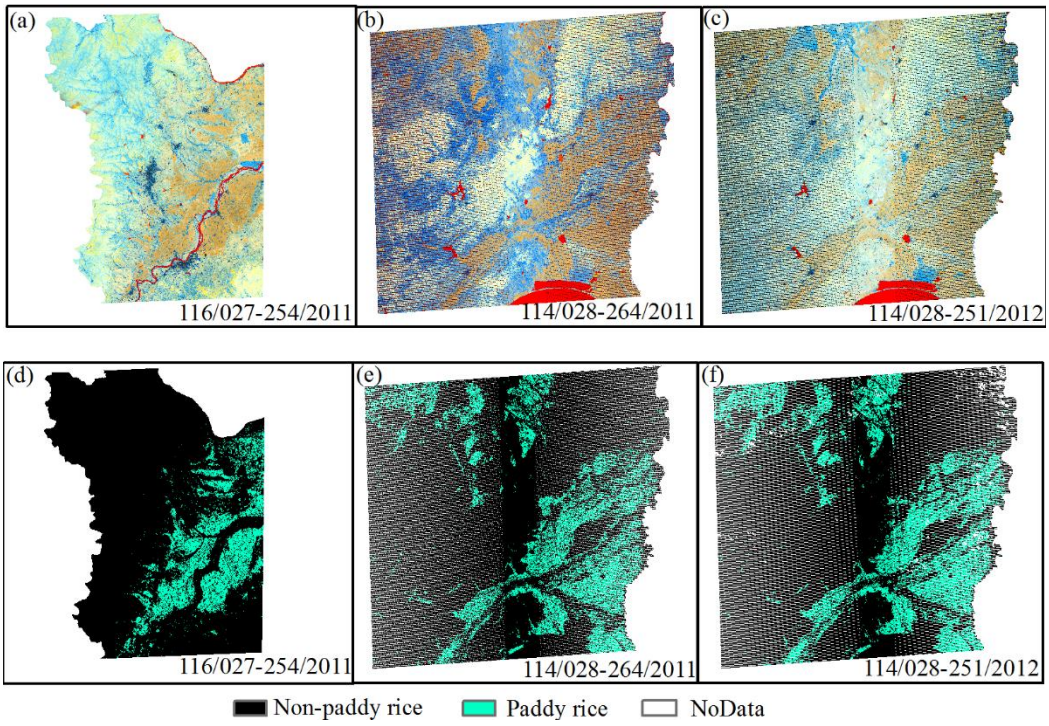


Figure 2.7 (a)–(c), Landsat FCC images (R/G/B = LSWI / NDVI / (NDVI+EVI)/2-LSWI); (d)–(f), ripening rice maps for 116/027-254/2011, 114/028-264/2011, and 114/028-251/2012

The ripening rice map of 114/028-264/2011 had high spatial consistency with the flooding/transplanting rice map of 114/028-176/2011 with a correlation coefficient of 0.8.

The differences between the two rice maps were subtle and mainly distributed along the boundaries of rice fields. The overall accuracy and KAPPA coefficient of the ripening rice map of 114/028-264/2011 was 94% and 84% with a user and producer accuracy of 89% and 87% for paddy rice, and 95% and 96% for non-paddy rice.

2.3.3 Paddy rice map of the Sanjiang Plain and accuracy assessment

The paddy rice area was 20,294 km^2 in 2011, accounting for 19% of the total area of the Sanjiang Plain. Rice fields were mainly distributed at the alluvial plain of Heilongjiang, Songhua, and Ussuri Rivers in the northern region, the plains of Muleng River and Khank Lake in the southeast region, and the Woken River plain in the southwest region (Figure 2.8(a)).

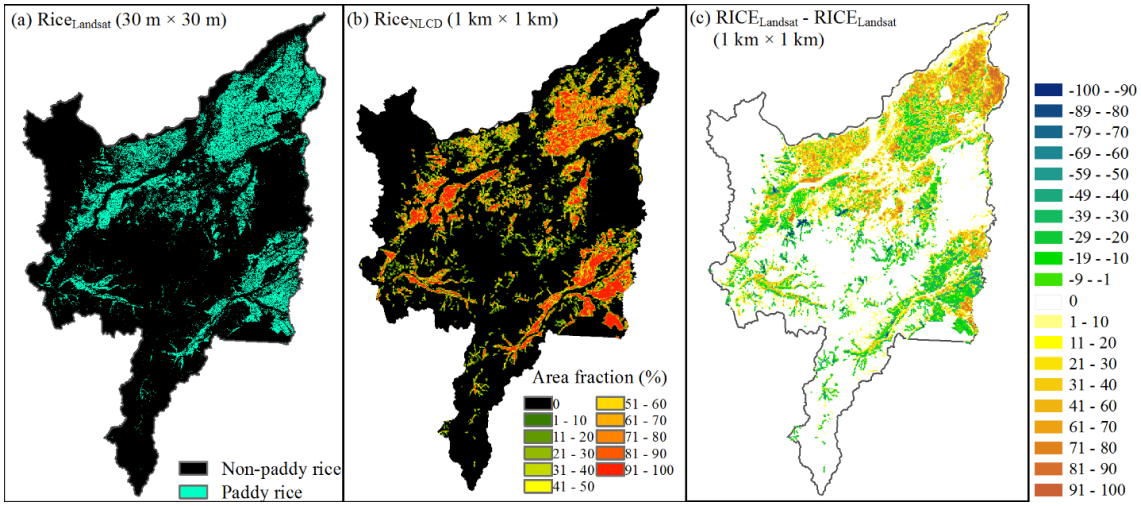


Figure 2.8 (a) 30 m Landsat-based paddy rice map ($RICE_{Landsat}$); (b) 1 km^2 area fraction of paddy rice on the 2010 NLCD ($RICE_{NLCD}$); (c) 1 km^2 area fraction difference map between the $RICE_{Landsat}$ and the $RICE_{NLCD}$

The accuracy of the $RICE_{Landsat}$ paddy rice increased from 61% for the POIs to 95% for the 60 m buffering distance (Figure 2.9). The paddy rice accuracy increased by 11% as the buffering distance increased from 15 - 30 m and from 30 - 45 m. The accuracy

for the $RICE_{Landsat}$ non-paddy rice decreased from 97% for the POIs to 89% for the 60 m buffering distance.

The $RICE_{Landsat}$ had a reasonably high overall accuracy of 97% and a KAPPA coefficient of 90% according to the error matrix calculated with the ROIs (Table 2.3). The user and producer accuracies were 90% and 94% for paddy rice and 98% and 97% for non-paddy rice.

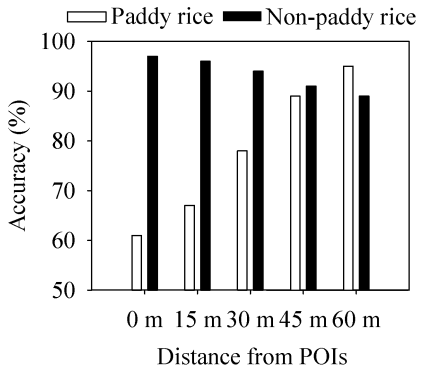


Figure 2.9 Classification accuracy based on POIs

Table 2.3 Accuracy assessment of the 30 m Landsat paddy rice map in the Sanjiang Plain, northeast China

		Paddy rice	Non-paddy rice	Total	Producer accuracy/%
Ground	Paddy rice	3535	247	3782	94
Truth Points	Non-paddy rice	399	15501	15900	97
Total		3934	15748		
User accuracy/%		90	98		

2.3.4 A comparison of the Landsat paddy rice map with the other paddy rice area estimate datasets

In general, the spatial pattern on the $RICE_{Landsat}$ was similar to that on the $RICE_{NLCD}$ (Figures. 2.8(a) and 2.8(b)). However, there were still some significant

differences between the $RICE_{Landsat}$ and the $RICE_{NLCD}$. The total rice area from the $RICE_{Landsat}$ was 31% higher than that derived from the $RICE_{NLCD}$ (15,465 km^2). The northern region showed a significant discrepancy between the $RICE_{Landsat}$ and the $RICE_{NLCD}$ (Figure 2.8(c)).

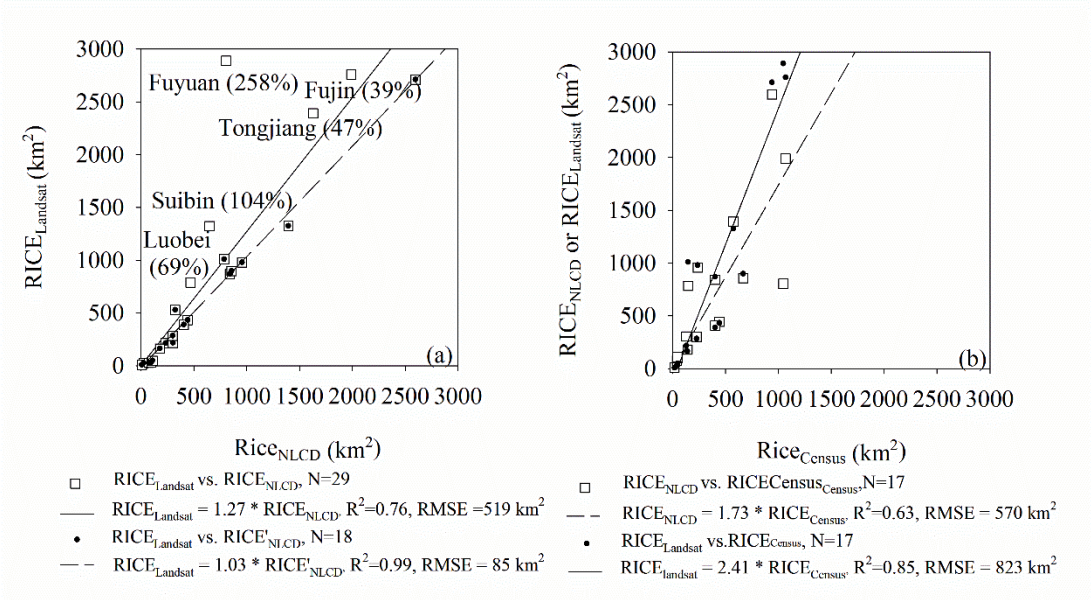


Figure 2.10 (a) County-level comparison of paddy rice area estimates between the $RICE_{Landsat}$ and the $RICE_{NLCD}$; (b) county-level comparison of paddy rice area estimates between the $RICE_{Landsat}$ and the $RICE_{Census}$

The $RICE_{Landsat}$ had higher area estimates than the $RICE_{NLCD}$ for Fujin (39%), Tongjiang (47%), Luobei (69%), Suibin (104%), and Fuyuan (258%) in the north region (Figure 2.10(a)). For the other counties, the $RICE_{Landsat}$ rice area matched well with the $RICE_{NLCD}$ estimates (the solid regression line in Figure 2.10(a)). The $RICE_{Landsat}$ rice area correlated well with the estimates from the $RICE_{Census}$ with R^2=0.85 (the solid regression line in Figure 2.10(b)). However, the $RICE_{Landsat}$ rice area was about 128% higher than the $RICE_{Census}$. The $RICE_{NLCD}$ also estimated the rice area around 66% higher than the $RICE_{Census}$ with R^2=0.63 (the dot regression line in Figure 2.10(b)). This result was

consistent with the previous conclusions of underreporting cropland area by the agricultural census report (Qiu et al., 2003; Liu et al., 2005).

2.4 Discussion

The integration of the Landsat flooding/transplanting-based and ripening-based algorithms introduced in this paper contributes to the efforts to improve the resolution and accuracy of paddy rice maps at the regional scale. The Landsat flooding/transplanting-based algorithm follows the MODIS phenology-based algorithm by identifying the temporary inversion between LSWI and EVI (NDVI) during the field flooding and seedling transplanting stages. Using the simple decision rules and training samples on LSWI, NDVI, and (NDVI+EVI)/2-LSWI, the Landsat ripening-based algorithm has shown the spatial and temporal robustness to extract the high-accuracy ripening rice maps.

The minimum classification unit plays an important role in determining the precision of the $RICE_{Landsat}$ and $RICE_{NLCD}$. The $RICE_{Landsat}$ was generated by pixel-based classification, with a classification unit of 30 m × 30 m. The $RICE_{NLCD}$ was generated by onscreen digitalization primarily from the 30 m Landsat at a scale of 1:100,000, with the minimum classification unit equivalent to 3×3 Landsat pixels. Thus, rice fields smaller than 3×3 Landsat pixels cannot be identified by the NLCD (Liu et al. 2005). In other words, the $RICE_{Landsat}$ can show the spatial pattern of paddy rice in far more detail than the NLCD.

Two sites were selected to evaluate the discrepancies between the $RICE_{Landsat}$ and $RICE_{NLCD}$. Site 1 represents the case of $RICE_{Landsat}$ = paddy rice and $RICE_{NLCD}$ = non-paddy rice. The high resolution image on 09/05/2010 shows that Site 1 was paddy rice in

2010 (Figure 2.11(a)). The temporal profiles of MODIS vegetation indices during 2000–2012 show the presence of the flooding/transplanting phases ($LSWI_{MODIS}$+0.05 > EVI_{MODIS} ($NDVI_{MODIS}$)) in May and June from 2009–2012 (highlighted in gray, Figure 2.11(b)). This proves that Site 1 was paddy rice starting in 2009, which matches with the $RICE_{Landsat}$. Site 2 represents the case of $RICE_{Landsat}$ = non-paddy rice and $RICE_{NLCD}$ = paddy rice. The high resolution image on 08/22/2012 verifies that Site 2 was non-paddy rice in 2012 (Figure 2.11(c)). The temporal profiles of MODIS vegetation indices don't show the presence of the flooding/transplanting phases in May and June of 2000–2012 (Figure 2.11(d)). This verifies that Site 2 was non-paddy rice from 2009–2012, which also matches with the $RICE_{Landsat}$. In summary, the $RICE_{Landsat}$ for Sites 1 and 2 agrees with the interpretation analysis from the high-resolution image and temporal MODIS vegetation indices. It can be concluded that the significant differences between the $RICE_{NLCD}$ and the $RICE_{Landsat}$ are most likely caused by the visual interpretation uncertainties on the $RICE_{NLCD}$. Two main factors contribute to the uncertainties of the $RICE_{NLCD}$. First, image selection determines the interpretation accuracy of paddy rice. The NLCD is produced based on a single FCC image (R/G/B=NIR/Red/Green) (Liu et al. 2005), on which paddy rice might show a similar image tone (red color) with other vegetation types. Adding the SWIR can increase visual interpretation accuracy of paddy rice (Li et al. 2012). Our results suggest that incorporating phenological information using the multi-temporal Landsat FCC images (R/G/B=SWIR/NIR/Red) during the flooding/transplanting and ripening phases should be considered for the rice interpretation of the NLCD. Secondly, the interpreter's expertise, including a good knowledge of the study area and image features (tone, texture, spatial pattern, etc.) of

paddy rice, also plays an important role. However, the interpreter's expertise is not objective and repeatable (Shalaby and Tateishi 2007), and the interpretation error cannot be predictable even across a large region.

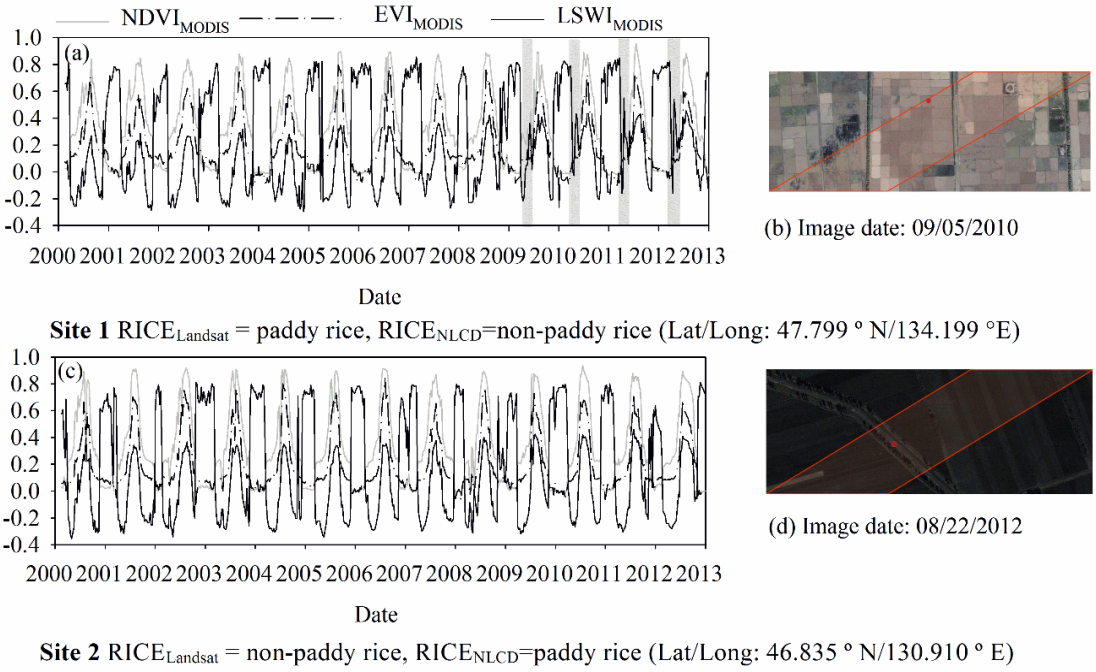


Figure 2.11 Evaluation of the discrepancy between the RICE$_{Landsat}$ and the RICE$_{NLCD}$: (a) and (c), the high-resolution images on Google Earth; (b) and (d), seasonal dynamics of 500 m MODIS vegetation indices (NDVI, EVI, LSWI) during 2000–2012

Several factors contribute to uncertainties in the flood/transplanting and ripening-based algorithms using multi-temporal Landsat images to identify paddy rice on a large spatial scale, such as Southeast Asia—the global main rice cultivation region. Southeast Asia has variable landscapes, topography, and climate along with complex rice-growing ecosystems and multiple cropping intensities (Kuenzer and Knauer 2013; Xiao et al. 2006a). The first factor is the similarity of the flooding/transplanting characteristics from other land types, including mangrove forests and the seasonally inundated natural

wetlands, which can be misclassified as paddy rice. The second factor is the intensive collection of training ROIs to implement the ripening-based algorithm. The third factor is the arbitrary thresholds for generating the terrain mask as rice cultivation terrain, which is variable across regions. Finally, Southeast Asia generally has a tropical monsoon climate with only a short dry season from November to March. Frequent rainfall during the long wet season significantly limits the availability of good-quality Landsat data. The inclusion of other fine-resolution satellite data will increase observation frequency and may help map rice distribution in monsoon Asia in the future.

2.5 Conclusion

Information on the spatial extent of paddy rice planting area is important for studies of rice growth and yield prediction, water resource management, and methane emission assessment. However, spatial datasets of paddy rice at a fine resolution with reliable accuracy are still not available at the regional scale. This study demonstrated the potentials of multi-temporal Landsat imagery in regional-scale rice classification by integrating the phenological and spectral features of paddy rice in the flooding/transplanting and ripening phases. The multi-temporal Landsat vegetation indices were sensitive to tracking the seasonal dynamics of the vegetation-to-water ratio of the rice fields during the flooding and seedling transplanting phases. The unique spectral features of the ripening paddy rice were spatially and temporally robust and can be used to identify paddy rice from other land cover types. However, future studies should investigate several factors such as non-cropland inundated land types, terrain conditions, and image availability when applying the methodology in this study to rice field

identification in other regions, particularly in Southeast Asia with its complex rice cultivation ecosystems.

Chapter 3: Phenology and gross primary production of two dominant savanna woodland ecosystems in Southern Africa

Abstract

Accurate estimation of gross primary production (GPP) of savanna woodlands is needed for evaluating the terrestrial carbon cycle at various spatial and temporal scales. The eddy covariance (EC) technique provides continuous measurements of net CO_2 exchange (NEE) between terrestrial ecosystems and the atmosphere. Only a few flux tower sites were run in Africa and very limited observational data of savanna woodlands in Africa are available. Although several publications have reported on the seasonal dynamics and interannual variation of GPP of savanna vegetation through partitioning the measured NEE data, current knowledge about GPP and phenology of savanna ecosystems is still limited. This study focused on two savanna woodland flux tower sites in Botswana and Zambia, representing two dominant savanna woodlands (mopane and miombo) and climate patterns (semi-arid and semi-humid) in Southern Africa. Phenology of these savanna woodlands were delineated from three vegetation indices derived from Moderate Resolution Imaging Spectroradiometer (MODIS) and GPP estimated from eddy covariance measurements at flux tower sites (GPP_{EC}). The Vegetation Photosynthesis Model (VPM), which is driven by satellite images and meteorological data, was also evaluated, and the results showed that the VPM-based GPP estimates (GPP_{VPM}) were able to track the seasonal dynamics of GPP_{EC}. The total GPP_{VPM} and GPP_{EC} within the plant growing season defined by a water-related vegetation index differed within the range of ± 6%. This study suggests that the VPM is a valuable tool for

estimating GPP of semi-arid and semi-humid savanna woodland ecosystems in Southern Africa.

3.1 Introduction

Savannas are one of the most widely distributed vegetation types, covering one-fifth of the earth land surface (Scholes and Hall 1996). A recent modeling study estimated an annual sum of about 30 Pg C gross primary production (GPP) from tropical savannas and grasslands, accounting for 25.7 % of the global terrestrial GPP (Beer et al. 2010). Africa, which is dominated by the largest area of savanna ecosystems in the world, is considered a main source of uncertainty in the global terrestrial carbon cycles (Weber et al. 2009; Williams et al. 2007). Current knowledge of Africa's carbon fluxes and storage is still limited due to the spatial extent, fire disturbance, and high interannual variability in climate and productivity (Ciais et al. 2011; Williams et al. 2007; Woollen et al. 2012).

Mopane and miombo woodlands in South and Central Africa covering 3.6 million km^2 of land are the single largest dry woodlands in the world. Over the past decade, continuous fluxes of carbon, water, and energy between the land surface and the atmosphere, as measured with the eddy covariance technique, have been used to study the temporal dynamics and spatial pattern of the carbon cycle of savanna woodlands in Southern Africa (Archibald et al. 2009; Kutsch et al. 2008; Merbold et al. 2009; Merbold et al. 2011; Scanlon and Albertson 2004; Veenendaal et al. 2004; Williams et al. 2009). However, such measurements have been made at only a few sites and often over short time periods (Veenendaal et al. 2004).

Satellite remote sensing at moderate spatial resolutions provides daily observations of land surface properties at the spatial scale compatible with the footprint

sizes of the eddy covariance observation sites. It has become a more and more important data source for the study of vegetation phenology (Alcantara et al. 2012; Brown et al. 2012; Jones et al. 2012; Kim et al. 2012; Kross et al. 2011; White et al. 2009) and GPP estimates (Gitelson et al. 2012; Kalfas et al. 2011a; Peng et al. 2011; Sakamoto et al. 2011; Sjostrom et al. 2009; Wang et al. 2010b; Wu and Chen 2012; Wu 2012; Zhang et al. 2012b).

Vegetation phenology is a fundamental determinant affecting the ecosystem processes of carbon, water, and energy exchange (Larcher 2003). It determines the timing and duration of a photosynthetically active canopy and influences the magnitude of carbon and water fluxes throughout the plant growing season (Jolly and Running 2004). The vegetation indices calculated from the reflectance of spectral bands have been proved to effectively monitor the vegetation phenology (Bradley et al. 2007; Moody and Johnson 2001; Sakamoto et al. 2005; Xiao et al. 2006b; Zhang et al. 2006). Earlier studies of phenology have focused on vegetation indices derived from visible and near infrared bands, for example, the Normalized Difference Vegetation Index (NDVI), which is calculated as a normalized ratio between near infrared and red spectral bands (Tucker 1979a), and the Enhanced Vegetation Index (EVI), which is calculated from blue, red, and near infrared bands (Huete et al. 2002). Both NDVI and EVI have been shown to effectively track the seasonality and spatial patterns of savanna phenology (Archibald and Scholes 2007; Chidumayo 2001; Higgins et al. 2011; Huttich et al. 2011). It is well known that the shortwave infrared band (SWIR) is sensitive to water in vegetation and soil. One SWIR-based vegetation index is the Land Surface Water Index (LSWI), which is calculated from near infrared (NIR) and SWIR (Xiao et al. 2004b). It has successfully

been applied to vegetation phenology study and phenology-based land cover mapping (Cai et al. 2011; Chandrasekar et al. 2010; Park and Miura 2011; Xiao et al. 2006b; Xiao et al. 2004b). A prior study has already indicated that LSWI was sensitive to the wet and dry conditions in Africa (Tian et al. 2012). Therefore, whether the time-series LSWI data can effectively extract the phenological dynamics of savanna woodlands in Southern Africa across precipitation gradient and woodland species types is the first question addressed in this study. Water availability at the regional scale, an important seasonal driver for savanna vegetation growth, is the primary limit for predicting savanna phenology patterns (Archibald and Scholes 2007).

A number of the satellite-PEMs have been developed to estimate GPP of vegetation as the product of the absorbed photosynthetically active radiation (APAR) and the light use efficiency (Coops 1999; Monteith 1972b; Potter et al. 1993; Prince et al. 1995; Ruimy et al. 1996). In one group of PEMs, the greenness-related vegetation indices are used to estimate APAR by the canopy. NDVI is most commonly used in the earlier PEMs (Potter et al. 1993; Prince and Goward 1995; Ruimy et al. 1994; Running et al. 2000b; Veenendaal et al. 2004; Yuan et al. 2007). In the other group of PEMs, chlorophyll-related vegetation indices such as EVI and chlorophyll index are used to estimate APAR by chlorophyll (Gitelson et al. 2006; Potter 2012; Sims et al. 2006; Xiao et al. 2004a; Xiao et al. 2004b).

The Vegetation Photosynthesis Model (VPM) is the first satellite-based PEMs that used the concept of chlorophyll and light absorption by chlorophyll (Xiao et al. 2004a; Xiao et al. 2004b). The VPM has been extensively verified for temperate, boreal and moist tropical evergreen forests (Xiao et al. 2004a; Xiao et al. 2004b; Xiao et al.

2005b; Xiao et al. 2005c), temperate and plateau grassland (Li et al. 2007; Wu et al. 2008) as well as agricultural ecosystems (Kalfas et al. 2011a; Wang et al. 2010b). However, its performance in simulating GPP of savanna woodland ecosystems is still unknown.

The objectives of this study are twofold: (1) to evaluate the potential of remote sensing vegetation indices (NDVI, EVI, and LSWI) in identifying land surface phenology of savanna woodlands and determining the growing season length; and (2) to examine the potential of the VPM to simulate GPP of two dominant savanna woodland sites differing in annual precipitation and vegetation composition in Southern Africa. The leaf-on and leaf-off phenological phases need to be identified and then used to evaluate the performance of satellite-based PEMs that estimate GPP of savanna woodland ecosystems. Although a vast area in Southern Africa is covered with mopane and miombo woodlands, there are only two sites with continuous measurements of CO_2 net exchange between the woodlands and the atmosphere by eddy covariance technique; and in this study we used data from the two sites, located in Botswana and Zambia.

3.2 Materials and methods

3.2.1 Study sites

These two eddy covariance flux sites of savanna woodlands are within the Kalahari Transect (KT) in Southern Africa, one of the International Geosphere-Biosphere Program (IGBP) Transects for quantifying biogeochemistry and primary production, water and energy balance, ecosystem structure and function at the continental scale (Scholes and Archer 1997). Both sites are located along a precipitation gradient in the semi-arid and sub-humid regions of Southern Africa. The geo-locations and landscape features of these two sites are shown in Figure 3.1 and Table 3.1. Detailed descriptions

of the two sites can be obtained via FLUXNET - a global network of micrometeorological tower sites (http://www.fluxnet.ornl.gov/fluxnet/sitesearch.cfm) and site specific publications (Arneth et al. 2006; Merbold et al. 2011; Veenendaal et al. 2004; Veenendaal et al. 2008).

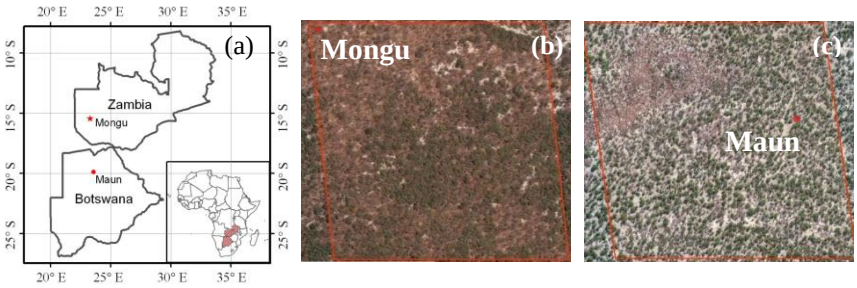


Figure 3.1 A simple illustration of the study sites, including (a) geo-locations of both savanna woodland flux sites in Botswana and Zambia; (b) landscapes at the Mongu site, Zambia, background image - Google Earth on 09/18/2005; (c) landscapes at the Maun site, Botswana, background image – Google Earth on 07/06/2011. The red square line in (b) and (c) corresponds to the size of a MODIS image pixel at 500-m spatial resolution, and the red dots represent the locations of the flux towers. The website http://eomf.ou.edu/visualization/gmap/ provides visualization of flux tower site locations and MODIS pixel boundary

Table 3.1 A summary description of the two savanna woodland flux tower sites

Site Name	Country	Latitude (°)	Longitude (°)	Ecosystem	C3/C4	MAP (mm)	MAT (°C)	Flux measurements
Maun	Botswana	-19. 9155	23. 5603	*mopane* woodland	80/20	464	22.6	1999 - 2001
Mongu	Zambia	-15.4388	23.2525	*miombo* woodland	95/5	945	25	2007 - 2009

MAP: Mean Annual Precipitation; MAT: Mean Annual Temperature

3.2.2 Site-specific meteorological data and CO_2 flux data

All meteorological and CO_2 flux data used in this study were downloaded from CarboAfrica data portal (http://gaia.agraria.unitus.it/newtcdc2/CarboAfrica_home.aspx). It provides the meteorological and CO_2 flux datasets at half hourly, daily, 8-day, and

monthly intervals. CO_2 fluxes and meteorological data of the two sites were available for the periods of 1999 - 2001 and 2007 - 2009, respectively (Figure 3.2 and Figure 3.3). The precipitation data in 2008/2009 at the Mongu site was incomplete due to a sensor malfunction. We used precipitation data from the Zambian Meteorological Department (20 km away) to replace the missing data. At the Maun site, precipitation started in late-November and lasted until May of the next year. Annual rainfall was 197 mm in 2000/2001 and 431 mm in 1999/2000, respectively. The wet season at the Mongu site was concentrated from mid-October to the end of March of the next year, and annual precipitation was 1160 mm in 2007/2008 and 1205 mm in 2008/2009 (Figure 3.2).

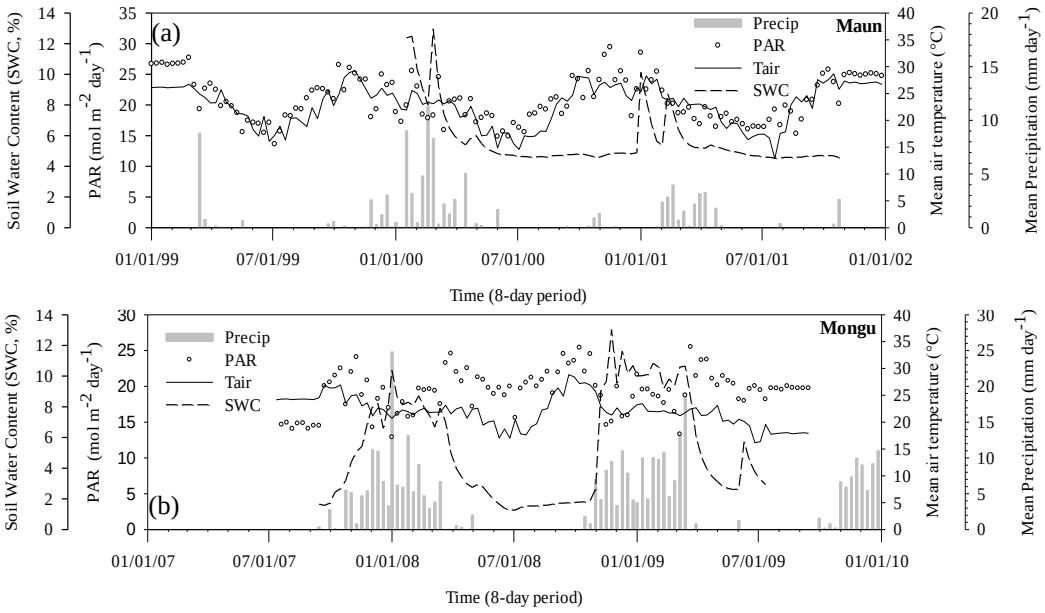


Figure 3.2 Seasonal dynamics and interannual variations of precipitation (Precip), photosynthetically active radiation (PAR), soil water content at the upper 100 cm of soil (SWC), and air temperature (T_{air}) observed at the two savanna woodland flux sites in Africa. (a) Maun, Botswana, during 1999 - 2001; (b) Mongu, Zambia, during 2007 - 2009

The 8-day Level 4 datasets contain air temperature, precipitation, PAR, GPP, and NEE. NEE is gap-filled by two mathematical algorithms: the Marginal Distribution Sampling (MDS) (Reichstein et al. 2005) and the Artificial Neural Network (ANN) approach as described in (Papale and Valentini 2003). In this study, we used the standardized GPP dataset partitioned from NEE generated with the MDS approach. We carefully evaluated the NEE and GPP data, and identified questionable observations (Figure 3.3). At the Maun site, three 8-day periods during December 2000 and January 2001 showed extremely large variations of NEE and GPP (in the range of 40% to 100% in comparison with its neighboring 8-day periods), we treated them as outliers and excluded them in data analysis (Figure 3.3a).

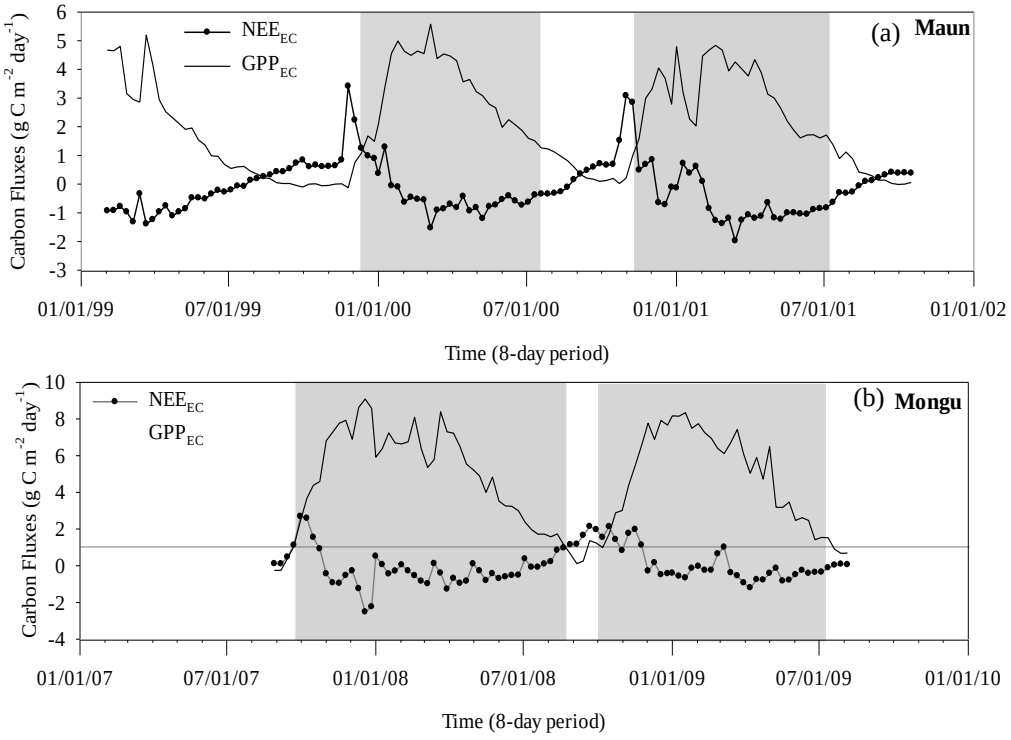


Figure 3.3 Seasonal dynamics and interannual variations of observed net ecosystem exchange of CO_2 (NEE_{EC}) and estimated gross primary production (GPP_{EC}) at the two savanna woodland sites, with the growing seasons highlighted. (a) the Maun site, Botswana, during 1999 - 2001; (b) the Mongu site, Zambia, during 2007 - 2009

3.2.3 MODIS land surface reflectance, vegetation indices, and MODIS GPP products

he Moderate Resolution Imaging Spectroradiometer (MODIS) onboard the Terra and Aqua satellites provide global coverage of imagery every one to two days from 36 spectral bands. This study used the MODIS Land Surface Reflectance 8-Day L3 Global 500 m products (MOD09A1, Collection 5). MOD09A1 provides land surface reflectance from seven spectral bands: Red (620 - 670 nm), NIR_1 (841 - 876 nm), Blue (459 - 479 nm), Green (545 - 565 nm), NIR_2 (1230 - 1250 nm), $SWIR_1$ (1628 - 1652 nm), and $SWIR_2$ (2105 - 2155 nm). There are forty-six MOD09A1 8-day composites within a year. The time-series MOD09A1data (2/2000 to 12/2011) for the Maun and Mongu sites were extracted from the MODIS data portal at the Earth Observation and Modeling Facility (EOMF), University of Oklahoma (http://www.eomf.ou.edu/visualization/manual/).

For each MODIS 8-day observation of surface reflectance, three vegetation indices were calculated using surface reflectance (ρ) from the blue, green, red, NIR_1, and $SWIR_1$ bands: (1) NDVI (Tucker 1979b), (2) EVI (Huete et al. 2002; Huete et al. 1997b), and (3) LSWI (Xiao et al. 2004a; Xiao et al. 2005c).

$$NDVI = \frac{\rho_{NIR_1} - \rho_{red}}{\rho_{NIR_1} + \rho_{red}} \tag{3.1}$$

$$EVI = \frac{\rho_{NIR_1} - \rho_{red}}{\rho_{NIR_1} + 6 \times \rho_{red} - 7.5 \times \rho_{blue} + 1} \tag{3.2}$$

$$LSWI = \frac{\rho_{NIR_1} - \rho_{SWIR_1}}{\rho_{NIR_1} + \rho_{SWIR_1}} \tag{3.3}$$

The vegetation indices calculated from surface reflectance contained noise caused by cloud, cloud shadow, atmospheric aerosols, and the large observing angle. The quality flags of MOD09A1 files showed many bad-quality observations over the course of the

wet season for the Mongu site. If the quality flag of an observation listed cloud, cloud shadow, aerosol quality, or adjacency to cloud, the observation was marked as unreliable. Built upon the two-step gap-filling procedure reported in earlier studies (Xiao et al. 2004a), we used a three-step gap-filling procedure to gap-fill vegetation index time series data. Step 1 deals with only one bad-quality observation (x(t)). We defined a filter with a three-observation moving window (x(t-1), x(t) and x(t+1)) and used data considered to be of good quality or reliable observations to correct or gap-fill unreliable observations. If both x(t-1) and x(t+1) pixels were reliable and x(t) was unreliable, the average of x(t-1) and x(t+1) was used to replace x(t). If only one observation (either x(t-1) or x(t+1)) was reliable and x(t) was unreliable, we used that observation to replace x(t). Step 2 addresses the situation with two consecutive bad-quality observations ((x(t), x(t+1)). We defined a filter with a 4-observation moving window (x(t-1), x(t), x(t+1), x(t+2)). We calculated the difference between x(t-1) and x(t+2) values and added them as an increment to gap-fill x(t) and x(t+1). Step 3 deals with the situation with three or more consecutive bad observations. We used multi-year mean vegetation index data during 2000 - 2011 to gap-fill those individual 8-day periods with bad quality. For example, the mean (M) and standard deviation (SD) of NDVI at individual 8-day periods over 2000 - 2011 (12 years) were first calculated using the reliable observations in 8-day periods, which constructed a mean NDVI time series in a mean year. We then calculated differences of NDVI between reliable observations in a year (e.g., 2007) and the mean NDVI values (M) over 2000 - 2011 (i.e., the mean year). If a year was closer to the mean year, we used M values to gap-fill those 3 or more unreliable observations. If a year was close to the M-SD values, we used M-SD values to gap-fill those 3 or more unreliable

observations. The same rule was applied to M+SD case. Figure 3.4 shows a comparison between the raw vegetation index data and the gap-filled vegetation index data at these two sites. 16% and 35% of the vegetation index observations were gap-filled during the growing seasons of the study periods for the Maun and Mongu sites, respectively.

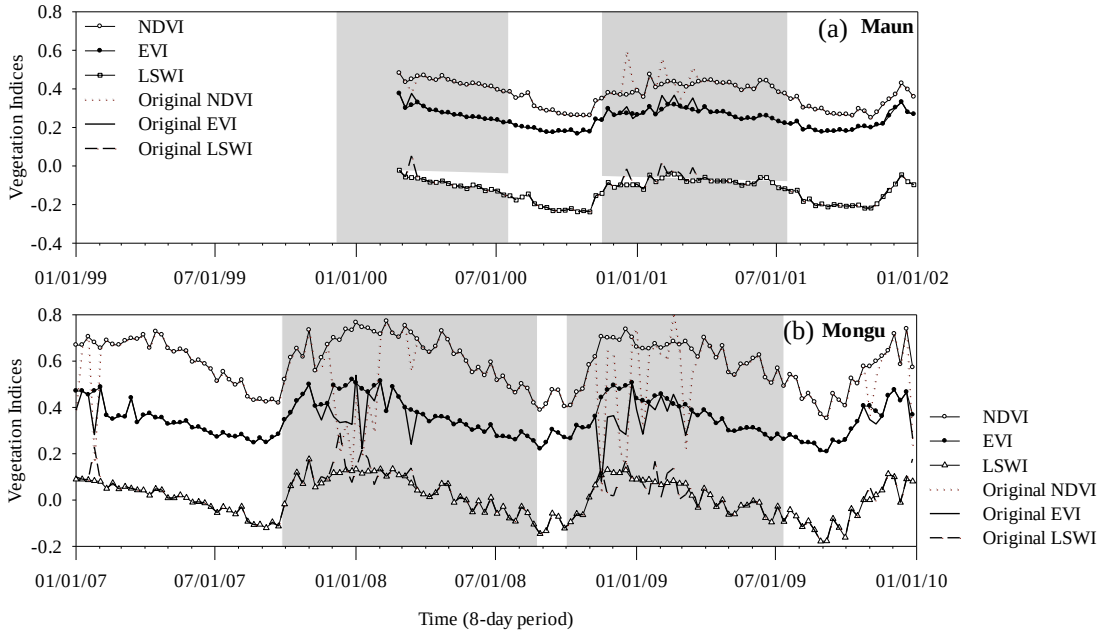


Figure 3.4 Seasonal dynamics and interannual variations of three MODIS-derived vegetation indices at the two savanna woodland flux sites, with the growing seasons highlighted (a) the Maun site, Botswana, during 1999 - 2001; (b) the Mongu site, Zambia, during 2007 - 2009

The MODIS product (MOD17A2), which is the first continuous satellite-driven GPP datasets across the global at a 1 km × 1 km spatial resolution and an 8-day temporal resolution since 2000, was included in this study for model comparison. MOD17A2 is driven by the datasets including land cover, FPAR/LAI, and surface meteorology inputs (Zhao et al. 2006). The MODIS GPP product ($GPP_{MOD17A2}$) were acquired from the Oak Ridge National Laboratory's Distributed Active Archive Center website (http://daac.ornl.gov/MODIS/).

3.2.4 The Vegetation Photosynthesis Model (VPM)

The Vegetation Photosynthesis Model (VPM) is based on the conceptual partitioning of chlorophyll and non-photosynthetically active vegetation (NPV) in a canopy. It estimates GPP over the plant growing season at daily or weekly intervals (Xiao et al. 2004a)

$$GPP = \varepsilon_g \times FPAR_{chl} \times PAR \tag{3.4}$$

where PAR is the photosynthetically active radiation (μmol photosynthetic photon flux density, PPFD), $FPAR_{chl}$ is the fraction of PAR absorbed by chlorophyll in the canopy, and ε_g is the light use efficiency (μmol/μmol PPFD).

The light use efficiency parameter (ε_g) is estimated by the theoretical maximum light use efficiency (ε_0, umol/umol PPFD), air temperature (Tscalar), water condition of land surface (W_{scalar}) and vegetation growing stage (P_{scalar}):

$$\varepsilon_g = \varepsilon_0 \times T_{scalar} \times W_{scalar} \times P_{scalar} \tag{3.5}$$

T_{scalar} is estimated at each time interval, using the formula developed for the Terrestrial Ecosystem Model (Raich et al. 1991):

$$T_{scalar} = \frac{(T-T_{min})(T-T_{max})}{[(T-T_{min})(T-T_{max})]-(T-T_{opt})^2} \tag{3.6}$$

where T_{min}, T_{opt}, and T_{max} are minimum, optimum, and maximum temperature for leaf photosynthetic activities, respectively. When air temperature falls below T_{min}, T_{scalar} is set to zero. Considering optimum temperature ranges and the predominant climate at the two sites, the T_{min}, T_{opt}, and T_{max} were set to 10˚C, 28˚C, and 48˚C, respectively (McGuire et al. 1992).

Instead of using soil moisture and/or water vapor pressure deficit (VPD), the VPM uses LSWI to estimate the effect of land surface water conditions on photosynthesis (W_{scalar}):

$$W_{scalar} = \frac{1+LSWI}{1+LSWI_{max}} \tag{3.7}$$

where $LSWI_{max}$ is the maximum LSWI during the growing season for an individual pixel (Xiao et al. 2004a). Equation 3.7 was proven to work well in vegetation with semi-humid and humid climate (Xiao et al. 2004a; Xiao et al. 2006b; Xiao et al. 2004b; Xiao et al. 2005c) and we used it for the Mongu site in this study. LSWI of vegetation with arid and semi-arid climate could have very low values (-0.20 or lower). LSWI threshold value (LSWI >= -0.1) was used to delineate vegetation phenology in a dynamic system of bare soils and crops (John et al. 2013; Kalfas et al. 2011a). We proposed a slightly modified W_{scalar} (see Equation 3.8) and used it for the Maun site (the semi-arid site). In Equation 3.8, we added the absolute value of LSWI >= -0.1 into the denominator:

$$W_{scalar} = \frac{1 - LSWI}{1 + 0.1 + LSWI_{max}} \tag{3.8}$$

P_{scalar} accounts for the effect of leaf longevity on photosynthesis on the canopy level. For deciduous trees, P_{scalar} is calculated at two different phases as linear function:

$$P_{scalar} = \frac{1 + LSWI}{2} \quad \text{during bud emergence to full leaf expansion} \tag{3.9}$$

$$P_{scalar} = 1 \quad \text{after full leaf expansion} \tag{3.10}$$

$FPAR_{chl}$ is estimated as a linear function of EVI (Equation 3.11) and the coefficient α is set to 1.0 in the current version of the VPM model (Xiao et al. 2004a):

$$FPAR_{\text{chl}} = a \times EVI \tag{3.11}$$

3.3 Results

3.3.1 Land surface phenology as delineated by CO_2 flux data and vegetation indices

The Maun Site

GPP_{EC} showed strong seasonal dynamics at the site (Figure 3.3a). GPP_{EC} started to rise and exceeded 1 g C m^{-2} day^{-1} in late November 1999, increased rapidly and peaked in March 2000 (Figure 3.3a). After the peak, GPP_{EC} gradually decreased and fell below 1 g C m^{-2} day^{-1} again by July 2000. Similar seasonal dynamics also occurred in 2000/2001. The leaf-on and leaf-off phases of mopane woodlands delineated by seasonal GPP_{EC} occurred in November and July, respectively.

At the end of the dry season in 1999/2000, NDVI, EVI, and LSWI remained low (< 0.3, < 0.2, and < -0.15) for about three months, followed by a rapid increase in early November of 2000/2001 (Figure 3.4a). The thresholds of NDVI, EVI, and LSWI, when GPP_{EC} was above 1 g C m^{-2} day^{-1}, were ≥ 0.3, ≥ 0.2 and ≥ -0.15 (Figure 3.4a). All three vegetation indices continuously increased to the maximum in late February. At the end of the wet season, when GPP_{EC} began to decline to 1 g C m^{-2} day^{-1} and below, NDVI, EVI and LSWI decreased similarly (0.3, 0.2, and -0.1) during the leaf senescence and abscission stages. Therefore, compared with the seasonal dynamics and interannual variation of GPP_{EC}, all three vegetation indices have the potential to identify the growth dynamics of mopane woodlands at the Maun site in Botswana.

Table 3.2 summarizes the land surface phenology (leaf-on and leaf-off dates) as determined from GPP_{EC} and vegetation indices at the Maun site. As defined by GPP_{EC} (> 1 g C m^{-2} day^{-1}), the leaf-on and leaf-off dates of 2000/2001 were 11/08/2000 and

07/12/2001, respectively. The leaf-on date of 2000/2001 defined by LSWI was the same as defined by GPP_{EC} (11/08/2000); and the leaf-off date defined by LSWI (07/04/2000) differed from that defined by GPP_{EC} (07/12/2001) by one week earlier. The total GPP over the growing season defined by LSWI (710 g C m^{-2}) was about 1.5 % lower than the total GPP over the growing season defined by GPP_{EC} (721 g C m^{-2}).

Table 3.2 Land surface phenology (leaf-on and Leaf-off dates) of the savanna woodland flux tower sites in Botswana and Zambia, as delineated by the estimated Gross Primary Production (GPP) data from the flux towers and a NIR/SWIR-based vegetation index (LSWI)

Site Name	$GPP_{EC} \geq$ 1 g C m^{-2} day^{-1}		Total GPP_{EC}	LSWI ≥ -0.1 or ≥ -0.15*		Total GPP_{EC}	GPP_{EC} %RE
	Leaf-on date	Leaf-off date		Leaf-on date	Leaf-off date		
Maun	12/11/2000	07/19//2000		N/A	07/11/2000*	N/A	N/A
	11/8/2000	07/12/2001	721	11/8/2000*	07/04/2001	710	-1.5%
Mongu	09/22/2007	08/20/2008	1789	09/22/2007	08/20/2008	1789	0%
	09/21/2008	07/12/2009	1510	09/29/2008	07/04/2009	1486	-1.5%

* If LSWI time series data have values of < -0.15, we chose LSWI threshold value to be ≥ -0.15. Starting date for LSWI was the first date that has consecutive LSWI values ≥ -0.1/-0.15 over the period of late dry season to early wet season; Ending date for LSWI was the first date that has LSWI values ≥ -0.1/-0.15 over the period of late wet season and early dry season.

The Mongu Site

GPP_{EC} had a strong seasonal dynamics at the site (Figure 3.3b), varying between 0 and 9 g C m^{-2} day^{-1}. GPP_{EC} started to rise and exceeded 1 g C m^{-2} day^{-1} in late-September 2007, and rapidly increased until peaking in December 2007 (Figure 3.3b). From June to August 2008, GPP_{EC} continuously decreased and reached 1 g C m^{-2} day^{-1}. Similar temporal dynamics occurred in 2008/2009. Therefore, the leaf-on phase began in September, and the leaf-off phase happened between June and August.

NDVI, EVI, and LSWI increased in late September and corresponded well with the timing of GPP_{EC} increases. The thresholds of NDVI, EVI, and LSWI, when GPP_{EC} was above 1 g C m^{-2} day^{-1}, were ≥ 0.4, ≥ 0.3, and ≥ - 0.1, respectively (Figure 3.4b). NDVI, EVI, and LSWI peaked between November and January, and slowly decreased afterwards to 0.4/0.5, 0.3, and -0.1. The leaf-on and leaf-off dates defined by LSWI (≥ -0.1) in 2007/2008 were the same as defined by GPP_{EC} (Table 3.2), and the total GPP over the growing season defined by LSWI (1789 g C m^{-2}) was the same amount as the total GPP_{EC} (1789 g C m^{-2}). For 2008/2009, the leaf-on date defined by LSWI was one 8-day interval later than the one defined by GPP_{EC} whereas the leaf-off date was one 8-day interval earlier than the one defined by GPP_{EC}. The total GPP over the growing season defined by LSWI (1486 g C m^{-2}) was 1.5 % lower than the total GPP over the growing season defined by GPP_{EC} (1510 g C m^{-2}).

3.3.2 Quantitative relationships between vegetation indices and GPP_{EC}

At the Mongu site (Figures 3.5a, b), simple linear regression models between vegetation indices (NDVI and EVI) and GPP_{EC} during the growing season (LSWI ≥ -0.15 or -0.1) show that NDVI and EVI accounted for 22 % and 67 % of GPP_{EC} variances, respectively (Figure 3.5). Due to the sparse vegetation coverage with maximum leaf area index of 1.0 at the Maun site, NDVI can be easily influenced by soil background (Huete et al. 2002). Thus, the weak linear relationship between NDVI and GPP_{EC} can be attributed to the NDVI sensitivity to soil background under the low vegetation coverage at the Maun site. EVI performs better to track the subtle changes of mopane woodlands at this site by correcting the impact of canopy background and atmosphere correction (Huete et al. 2002).

At the Mongu site (Figures 3.5c, d), NDVI and EVI accounted for 65 % and 68 % of GPP_{EC} variances, respectively. EVI had a slightly stronger linear relationship with GPP_{EC} than NDVI. The relatively weak linear relationship between NDVI and GPP_{EC} might be attributed to the NDVI saturation in dense canopies as found at the Mongu site. During the peak of growing season (GPP_{EC} > 6 g C m^{-2} day^{-1}), NDVI values concentrated from 0.7 to 0.8. However, EVI had the wider dynamic range of 0.3 - 0.5 and was more sensitive to the canopy changes of miombo woodlands.

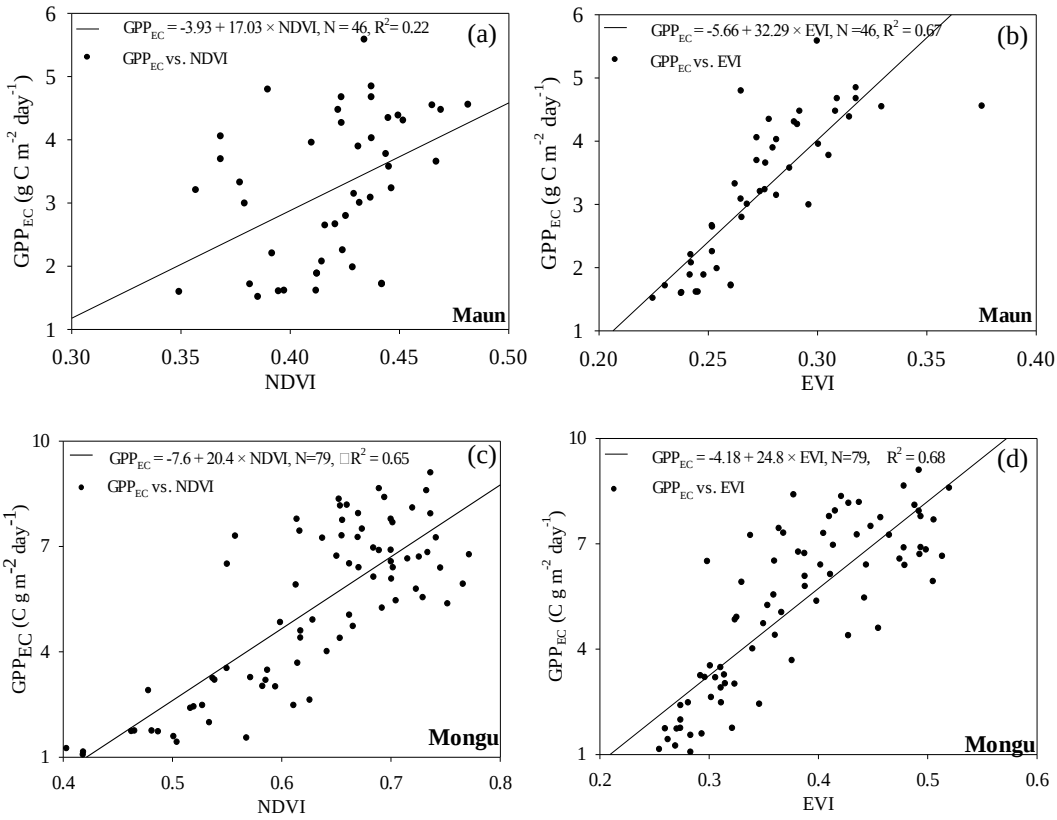


Figure 3.5 The relationships between two vegetation indices (NDVI, EVI) and gross primary production (GPP_{EC}) during the vegetation growth season at the two savanna woodland flux sites. (a) and (b) the Maun site, Botswana, during 1999 - 2001; (c) and (d) Mongu, Zambia, Africa, during 2007 - 2009

Note that NDVI accounted for 22% of GPP_{EC} variance at the Maun site but 65% of GPP_{EC} at the Mongu site. This large discrepancy in biophysical performance is attributed to the sensitivity of NDVI to soil background. LAI was much higher at the Mongu site than at the Maun site (see Section 3.2.1). This clearly suggests that for the study of sparse vegetation in arid and semi-arid climates, one needs to be cautious when using NDVI to estimate biophysical parameters such as GPP.

3.3.3 Seasonal dynamics of GPP from the Vegetation Photosynthesis Model (GPP_{VPM})

The Maun Site

The seasonal dynamics of GPP_{VPM} corresponded well with GPP_{EC} over the period of February to July 2000 (Figure 3.6). The simple linear correlation analysis between GPP_{VPM} and GPP_{EC} showed that GPP_{VPM} was strongly correlated with GPP_{EC} during this period ($R^2 = 0.92$, $p < 0.001$, (Figure 3.7a). The root mean square deviation value (RMSD) was 0.32 g C m^{-2} day^{-1} in 1999/2000 (Table 3.3). The sum of GPP_{VPM} over the period with observations available was 468 g C m^{-2}, which was about 0.6% higher than the sum of GPP_{EC} (465 g C m^{-2}).

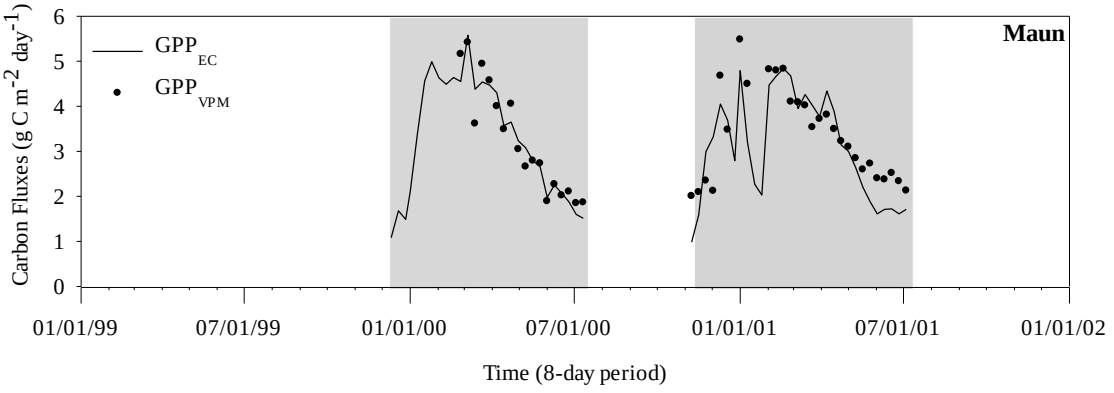


Figure 3.6 Seasonal dynamics and interannual variations of gross primary production at the Maun site, Botswana, during 1999 – 2001, with the growing seasons highlighted. GPP_{EC} - estimated GPP from the flux tower data; GPP_{VPM} - predicted GPP from the VPM model

During 2000/2001, the seasonal dynamics of GPP_{VPM} tracked reasonably well with GPP_{EC} except in January and July 2001 (Figure 3.6). The simple linear regression model between GPP_{VPM} and GPP_{EC} in 2000/2001 had a slope of 1.02 but $R^2 = 0.64$ ($p < 0.001$, Figure 3.7b), which suggested that GPP_{EC} data in 2001 had much larger variation. The RMSD value was 0.67 g C m^{-2} day^{-1} in 2000/2001 (Table 3.3). The seasonal sum of GPP_{VPM} in 2000/2001 was 753 C m^{-2}, being 6.1 % higher than the seasonal sum of GPP_{EC} (710 g C m^{-2}).

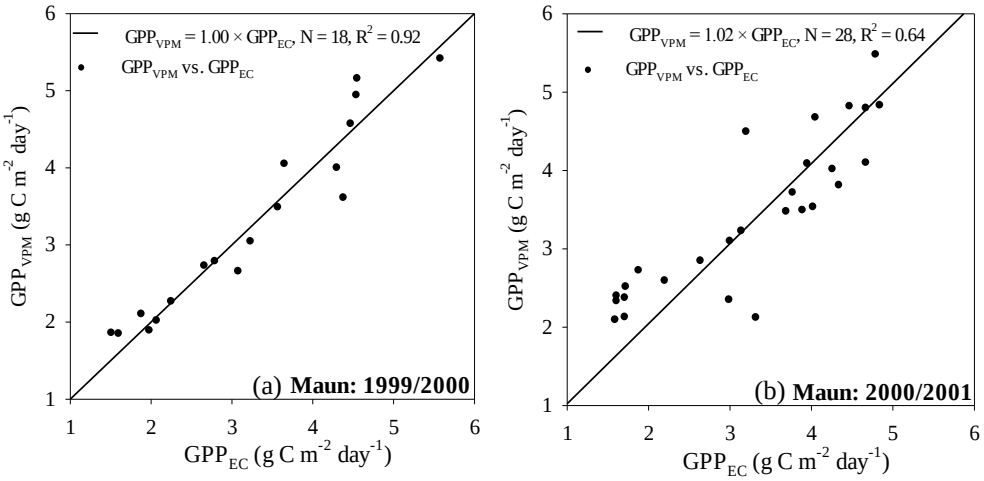


Figure 3.7 A comparison between GPP_{EC} and GPP_{VPM} at the Maun site, Botswana, during (a) 1999/2000, (b) 2000/2001

Table 3.3 A summary of gross primary production (GPP) estimated from the flux tower measurements (GPP_{EC}) and the predictions from the VPM model (GPP_{VPM}) at the savanna woodland flux tower sites in Botswana and Zambia. GPP_{EC}: seasonal sum of GPP estimated from the eddy covariance flux tower observations in g C m^{-2}, GPP_{VPM}: seasonal sum of GPP predicted by the VPM in g C m^{-2}, GPP%RE: relative error in GPP sums calculated as [(GPP_{VPM} - GPP_{EC})/GPP_{EC}]×100, RMSD: Root Mean Squared deviation

Site Name	Plant Growing Season	GPP_{EC}	GPP_{VPM}	GPP%RE	RMSD
Maun	1999-2000*	465	468	0.6	0.32
	2000-2001	710	753	6.1	0.67
Mongu	2007-2008	1789	1759	-1.7	0.76

2008-2009	1487	1422	-4.4	0.90

The Mongu Site

The seasonal dynamics of GPP_{VPM} correlated well with GPP_{EC} during 2007/2008 (Figure 3.8). GPP_{VPM} started to increase in late-September 2007, and reached the peak in December 2007. GPP_{VPM} decreased gradually after January and fell below 1 g C m^{-2} day^{-1} after July 2008. The simple linear correlation analysis showed that GPP_{VPM} correlated well with GPP_{EC} in 2007/2008 ($R^2 = 0.87$, $p < 0.001$, Figure 3.9a). The RMSD value was 0.76 g C m^{-2} day^{-1} over the period of 2007/2008. The seasonal sum of GPP_{VPM} during 2007/2008 was 1759 g C m^{-2}, approximately 1.7% lower than the sum of GPP_{EC} (1789 g C m^{-2}).

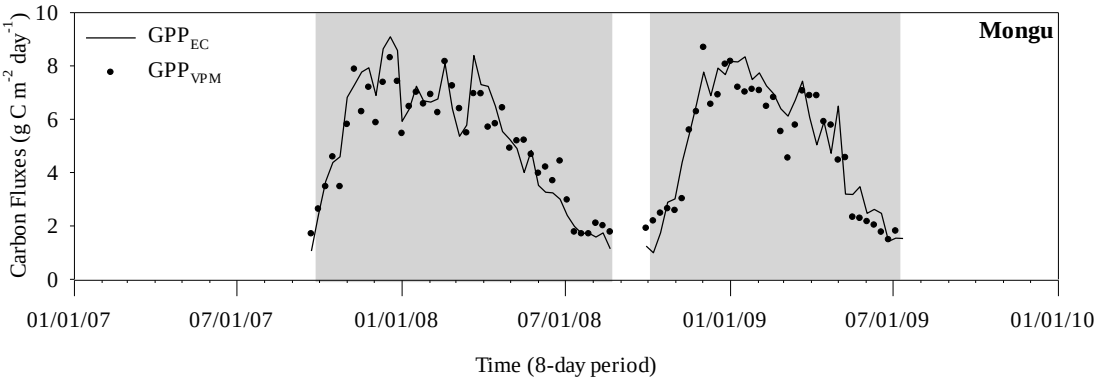


Figure 3.8 Seasonal dynamics and interannual variations of GPP_{EC} and GPP_{VPM} at the Mongu site, Zambia, during 2007-2009, with the growing seasons highlighted

The seasonal dynamics of GPP_{VPM} in the period of 2008/2009 showed the same trend as in 2007/2008. The simple linear correlation analysis showed that GPP_{VPM} correlated well with GPP_{EC} in 2008/2009 ($R^2 = 0.86$, $p < 0.001$, Figure 3.9b). The RMSD value was 0.90 g C m^{-2} day^{-1} over the period of 2008/2009. The seasonal sum of GPP_{VPM}

during 2008/2009 was 1487 g C m^{-2}, approximately 4.4 % lower than the seasonal sum of GPP_{EC} (1422 g C m^{-2}).

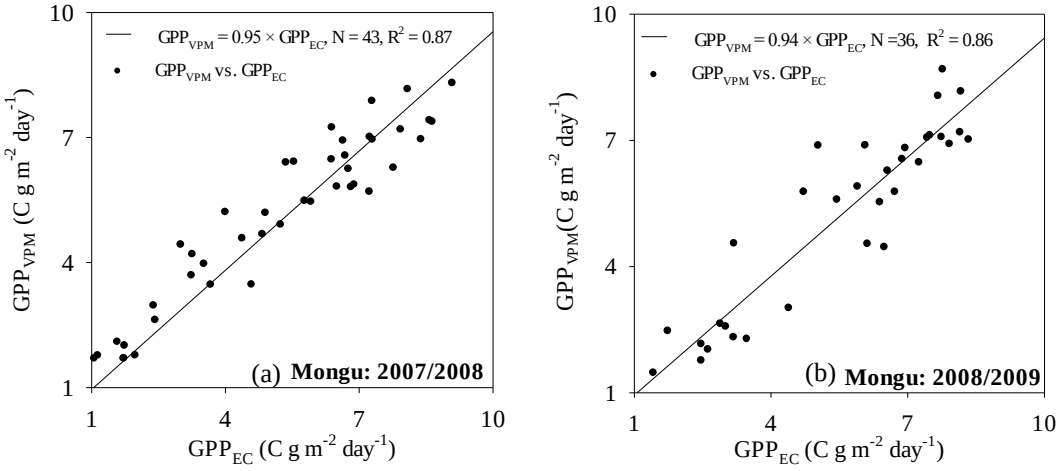


Figure 3.9 Comparison between GPP_{EC} and GPP_{VPM} at the Mongu site, Zambia, during (a) 2007/2008, (b) 2008/2009

3.4 Discussion

The importance of phenology of savanna woodlands in relation to the seasonal variation of net primary production has been recognized in earlier studies (de Bie et al. 1998). Several studies have evaluated and reported on the phenology of savanna vegetation (Chidumayo 2001; Fuller 1999; Fuller and Prince 1996; Hutley et al. 2011; Oliveira et al. 2012; Vrieling et al. 2011; Wagenseil and Samimi 2006). These studies found that NDVI had strong responses to phenological changes of savanna vegetation (Batista et al. 1997; Franca and Setzer 1998). For instance, Fuller (1999) and Fuller and Prince (1996) delineated leaf dynamics of savanna woodlands in Africa (including the mopane and miombo woodlands) with time series NOAA/AVHRR NDVI and rainfall data. The thresholds of average NDVI increase of 0.06 and average rainfall of 50 mm during September and October as an indication for vegetation growth status and water

content status were pre-defined to retrieve the early greening stage of savanna woodlands in the study (Fuller 1999; Fuller and Prince 1996). However, due to the effects of interception, run-off, and soil water movement, the threshold of the rainfall varying over space could not precisely represent the leaf water status. A few recent studies reported that EVI behaved better than NDVI to quantify the leaf dynamics of tropical savanna and could effectively describe the phenology (Bradley et al. 2011; Couto et al. 2011; Ferreira and Huete 2004; Ferreira et al. 2003; Hoffmann et al. 2005; Hüttich et al. 2009).

In this study we used both an ecosystem-physiology approach and a remote sensing approach to delineate phenology of savanna woodlands, and the results clearly show the convergence between these two approaches. As shown in this study, EVI threshold values ranged from 0.2 to 0.3, which is smaller than the range of NDVI threshold values (0.3 to 0.5). These results confirmed that EVI was more stable (a smaller range of threshold values used for leaf-on and leaf-off phases) than NDVI for delineating phenology of savanna woodlands when the threshold method was used. In addition, our study also showed that LSWI was more stable than NDVI and EVI for delineating phenology of savanna woodlands. The LSWI threshold value ($\geq$ -0.1) was used to determine the emergence (leaf-on) and harvest (leaf-off) of croplands (Kalfas et al. 2011a; Yan et al. 2009). In recent years, NIR/SWIR-based vegetation indices have received more attention for their potential in evaluating seasonal dynamics of vegetation canopy (Townsend et al. 2012; Xiao et al. 2002b).

Simulations of satellite-driven Production Efficiency Models (PEM), including the VPM, are affected by model parameterization and calibration (Wu et al. 2011). Different definitions and choices of maximum light use efficiency (ε_0) and environmental

factors are the main sources of PEM uncertainties. ε_0 determines the potential conversion efficiency of absorbed photosynthetically active radiation under the ideal growing condition. The values of ε_0 should be determined according to the vegetation function types (VFT). Some PEMs define ε_0 as an global constant value for all vegetation types; and others used the theoretical values from experiment measurements; and some derived ε_0 from the model fitting between NEE and PAR during the peak of growing season (Chen et al. 2011; Goerner et al. 2011; Wang et al. 2010a; Wu and Niu 2012; Xiao 2006; Zhu et al. 2006).

The theorectical ε_0 of C_3, 0.9 g C mol $PPFD^{-1}$ (Ehleringer and Björkman 1977) used in this simulation, is higher than the value in a previous study of tropical savanna in Northern Australia (0.63 g C mol $PPFD^{-1}$ or 1.29 g C MJ^{-1}) and the value used in the standard MODIS algorithm (MOD17) of 0.5 g C mol $PPFD^{-1}$ or 1.03 g C MJ^{-1} for the grassy woodlands (Kanniah et al. 2011; Kanniah et al. 2009). The large variation of ε_0 values in the PEMs suggests that more investigations of LUE calculation for savanna ecosystems, the mixed biome of tree (C_3) and grass (C_4), are needed. Accurate estimation of light use efficiency of the tree and grass mixed ecosystems needs precise experiments and modeling of the physiological and biochemical processes on the stand, canopy, and landscape scales (Caylor and Shugart 2004; Ludwig et al. 2004; Scholes and Archer 1997; Skarpe 1992; Whitley et al. 2011).

The VPM uncertainties also come from the two dominant down-regulation environmental factors related to water (W_{scalar}) and temperature (T_{scalar}). Here we report a model sensitivity analysis of the VPM: (1) without W_{scalar} ($GPP_{VPM_w/o_Wscalar}$), (2) without T_{scalar} ($GPP_{VPM_w/o_Tscalar}$), and (3) without both W_{scalar} and T_{scalar}

($GPP_{VPM_w/o_Wscalar_Tscalar}$) (Figure 3.10, Figure 3.11, Table 3.4). The effect of W_{scalar} on GPP_{VPM} is relatively larger at the Maun site than at the Mongu site, which is likely related to lower annual precipitation at the Maun site (464 mm, semi-arid climate) than at the Mongu site (945 mm, semi-humid climate). The effect of T_{scalar} on GPP_{VPM} is also much larger at the Maun site than at the Mongu site, which is likely related to the range of temperature variation at these sites (see Figure 3.2). When we compared the changes in slope ($GPP_{VPM} = a \times GPP_{EC}$), W_{scalar} had a higher impact than T_{scalar}. When we compared the changes in R^2, W_{scalar} had less impact than T_{scalar}. In the case without both T_{scalar} and W_{scalar}, the model overestimated GPP by 46% to 50% at the Maun site and by 13% to 16% at the Mongu site, suggesting that it is important to consider both water and temperature in semi-arid climate.

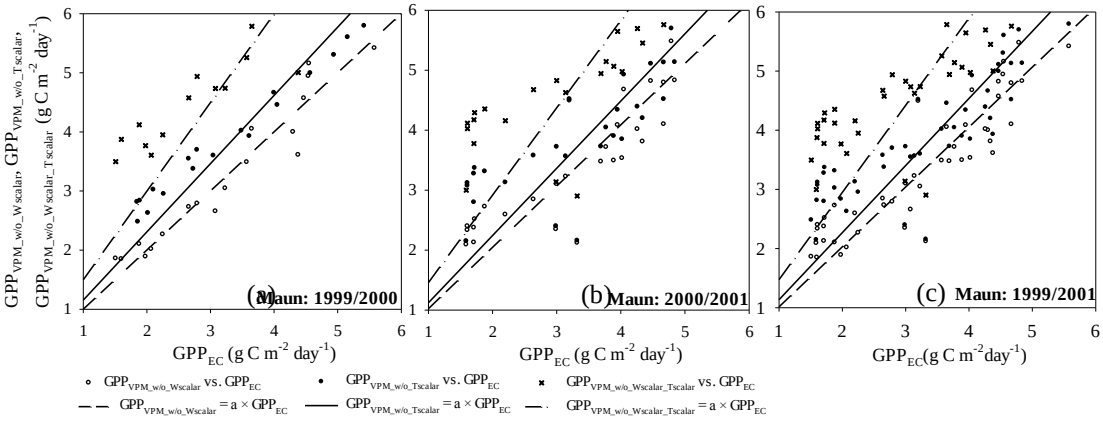


Figure 3.10 Sensitivity analysis of the VPM model at the Maun site, Botswana. It includes three cases of VPM simulations related to W_{scalar} and T_{scalar}: (1) without W_{scalar}, i.e., $\varepsilon_g = \varepsilon_0 \times T_{scalar}$; (2) without T_{scalar}, i.e., $\varepsilon_g = \varepsilon_0 \times W_{scalar}$; and (3) without both W_{scalar} and T_{scalar}, i.e., $\varepsilon_g = \varepsilon_0$. (a) 1999/2000 season; (b) 2000/2001 season, (c) both 1999/2000 and 2000/2001 seasons. See also Table 4 for the slopes and R^2 values of individual simple linear regression models

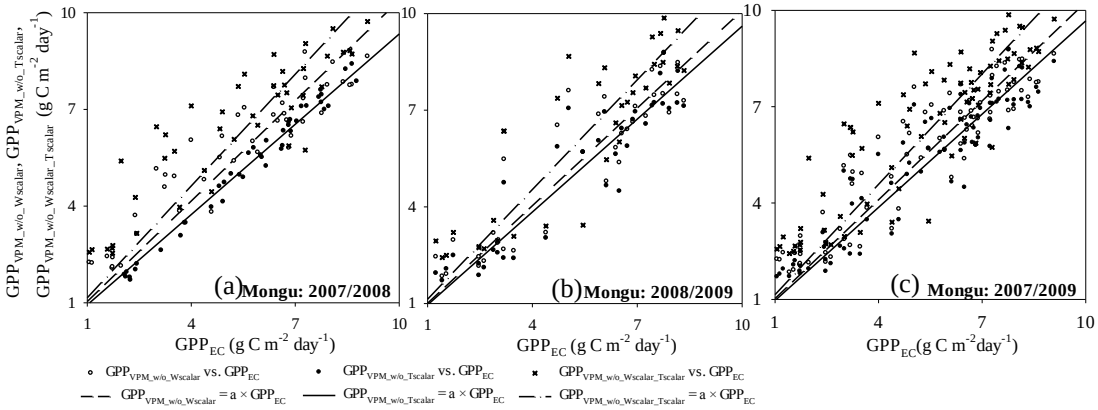


Figure 3.11 Sensitivity analysis of the VPM model at the Mongu site, Zambia, including three cases of VPM simulations related to W_{scalar} and T_{scalar}: (1) without W_{scalar}, i.e., $\varepsilon_g = \varepsilon_0 \times T_{scalar} \times P_{scalar}$; (2) without T_{scalar}, i.e., $\varepsilon_g = \varepsilon_0 \times W_{scalar} \times P_{scalar}$; and (3) without both W_{scalar} and T_{scalar}, i.e., $\varepsilon_g = \varepsilon_0 \times P_{scalar}$. (a) 2007/2008 season; (b) 2008/2009 season, (c) both 2007/2008 and 2008/2009 seasons. See also Table 4 for the slopes and R^2 values of individual simple linear regression models

At the Maun site, the discrepancy between GPP_{VPM} and GPP_{EC} seems relatively large in 2000/2001. This could be explained by MODIS data and GPP_{EC} data. One example is that GPP_{EC} in January 2001 dropped to 2 g C m^{-2} day^{-1} (Figure 3.6), more than 100% lower than the GPP_{EC} value in December 2000. Note that soil moisture data in January 2001 also had a dramatic drop (Figure 3.2a) but NEE data had a dramatic increase (Figure 3.3a). As soil moisture data were used to estimate ecosystem respiration, consequently GPP_{EC} dropped substantially in January 2001. However, the three vegetation indices did not drop accordingly in January 2001 (Figure 3.4a). If these observations of soil moisture and NEE data in January 2011 had no quality problem, one can speculate that the three vegetation indices are not able to reflect how short-term drought (flash drought) affected the vegetation. Another example is the discrepancy between GPP_{VPM} and GPP_{EC} in late May to June 2001. All three vegetation indices were higher in late May and June 2001 than in April to early May, but soil moisture and

precipitation data do not support the short-term increases in vegetation indices in that period. As the 8-day MODIS composite images were used in this study, evaluation of the image compositing method and daily MODIS images in semi-arid climates might be needed in the future.

The comparisons between the MODIS standard GPP product ($GPP_{MOD17A2}$) with GPP_{EC} showed that $GPP_{MOD17A2}$ overestimated GPP at the Maun site, and underestimated GPP at the Mongu site (Sjostrom et al. 2011; Sjöström et al. 2013). Here we compared seasonal dynamics and interannual variation of $GPP_{MOD17A2}$ and GPP_{VPM} (Figure 3.12). At the Maun site, $GPP_{MOD17A2}$ was substantially lower than GPP_{EC} during the first half of the growing season but higher than GPP_{EC} during the second half of the growing season (Figure 3.12a). At the Mongu site, $GPP_{MOD17A2}$ was substantially lower (up to 50%) than GPP_{EC} throughout the entire growing season (Figure 3.12b). In Wu et al. (2010), the underestimation of two PEMs (VPM and MOD17A2) happened among multiple-year simulations at a deciduous forest site. At the Mongu site in our study, it was found that both the GPP simulation from the VPM (GPP_{VPM}) and MOD17A2 ($GPP_{MOD17A2}$) at this site were underestimated compared to GPP_{EC}, especially for $GPP_{MOD17A2}$ (Figure 3.12b) which is consistent with Wu et al. (2010). A possible explanation might be that MODIS sensors are not able to sense the shaded leaves within the canopy, since the Mongu site is located in the Kataba Forest Reserve with a dense tree canopy, high LAI (the canopy height is above 10 m with the fractional canopy cover of 67%) and very sparse understory vegetation (section 3.2.1 and Figure 3.1c), and might be defined as “forest” to some degree. At the Maun site, both GPP_{VPM} and $GPP_{MOD17A2}$ didn’t show the significant underestimation compared with the Mongu site, and were closed to GPP_{EC} (slightly

overestimated, Figure 3.12a). The Maun is characterized as a sparse woodland, with a canopy height of 5 - 10 m and fractional canopy cover of 36%. In this situation, the MODIS sensors may sense all leaves within the canopy. In addition, other factors, such as global climate datasets used in MOD17A2 product, maximum light use efficiency parameter, and the fraction of photosynthetic active radiation absorbed by vegetation canopy ($FPAR_{canopy}$) further contribute to the large discrepancies between $GPP_{MOD17A2}$ and GPP_{EC} (Wu et al. 2010). Detailed analysis of the MOD17A2 algorithm is beyond the scope of this paper, but it does suggest that validation of satellite-driven PEMs at individual flux tower sites of savanna woodlands is important.

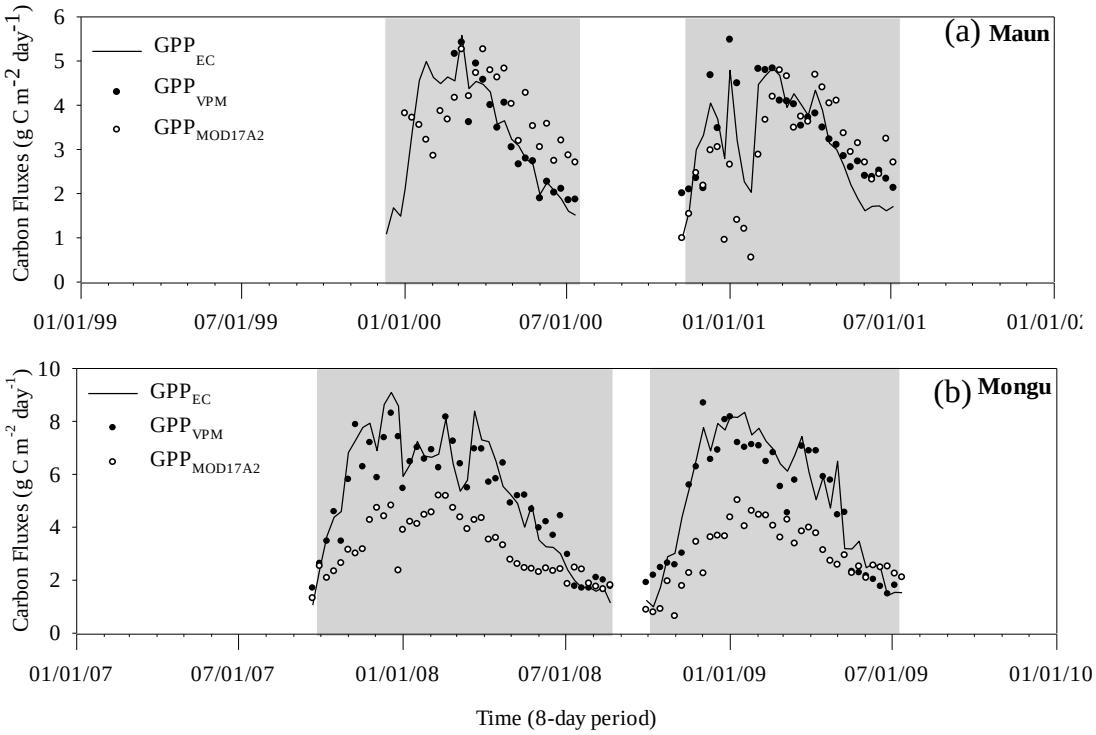


Figure 3.12 Comparison of GPP_{EC} and GPP_{VPM} as well as GPP derived from the MOD17A2 data product ($GPP_{MOD17A2}$). (a) the Maun site, Botswana, during 1999 - 2001; (b) the Mongu site, Zambia, during 2007 - 2009

3.5 Conclusion

The information of land surface phenology growing season length is useful for simulations of satellite-based PEMs. In this study, the land surface phenology of savanna woodlands, described by the satellite vegetation indices, especially the NIR/SWIR-water-sensitive vegetation indices (e.g., LSWI), was proven to agree well with the phenology based on ecosystem physiology as measured by eddy covariance technique. Previous studies have shown that the Vegetation Photosynthesis Model (VPM) provides robust and reliable estimates of GPP across several biomes and geographic regions. This study has also demonstrated the potential of the VPM to estimate the GPP in two savanna woodland ecosystems in Botswana and Zambia. The simulation results showed that the VPM performs reasonably well in tracking the seasonal dynamics and interannual variation of GPP at these two savanna woodland sites. Further evaluation of the VPM simulations for other savanna vegetation types is necessary before it is applied to estimate GPP of savanna ecosystems in Southern Africa at regional and continental scales.

Chapter 4: Effects of in-situ and reanalysis climate data on estimation of cropland gross primary production using the Vegetation Photosynthesis Model

Abstract

Satellite-based PEMs often require meteorological reanalysis data such as the North America Regional Reanalysis (NARR) by the National Centers for Environmental Prediction (NCEP) as model inputs to simulate gross primary production (GPP) at regional and global scales. This study first evaluated the accuracies of air temperature (T_{NARR}) and downward shortwave radiation (R_{NARR}) of the NARR by comparing with in-situ meteorological measurements at 37 AmeriFlux non-crop eddy flux sites, then used one PEM—the Vegetation Photosynthesis Model (VPM) to simulate 8-day mean GPP (GPP_{VPM}) at seven AmeriFlux crop sites, and investigated the uncertainties in GPP_{VPM} from climate inputs as compared with eddy covariance-based GPP (GPP_{EC}). Results showed that T_{NARR} agreed well with in-situ measurements; RNARR, however, was positively biased. An empirical linear correction was applied to R_{NARR}, and significantly reduced the relative error of R_{NARR} by ~25 % for crop site-years. Overall, GPP_{VPM} calculated from the in-situ ($GPP_{VPM(EC)}$), original ($GPP_{VPM(NARR)}$) and adjusted NARR ($GPP_{VPM(adjNARR)}$) climate data tracked the seasonality of GPP_{EC} well, albeit with different degrees of biases. $GPP_{VPM(EC)}$ showed a good match with GPP_{EC} for maize (Zea mays L.), but was slightly underestimated for soybean (Glycine max L.). Replacing the in-situ climate data with the NARR resulted in a significant overestimation of $GPP_{VPM(NARR)}$ (18.4/29.6 % for irrigated/rainfed maize and 12.7/12.5 % for irrigated/rainfed soybean). $GPP_{VPM(adjNARR)}$ showed a good agreement with $GPP_{VPM(EC)}$ for both crops due to the

reduction in the bias of R_{NARR}. The results imply that the bias of R_{NARR} introduced significant uncertainties into the PEM-based GPP estimates, suggesting that more accurate surface radiation datasets are needed to estimate primary production of terrestrial ecosystems at regional and global scales.

4.1 Introduction

Croplands cover 12 % of the global ice-free terrestrial surface (Ramankutty et al. 2008b) and provide food for more than seven billion people in the world. Increasing demand for food under the changing climate is one of the great challenges in the coming decades (Guanter et al. 2014; Lobell and Asner 2003). Gross Primary Production (GPP) of croplands is the total carbon uptake through photosynthesis. A recent modeling study estimated that croplands have an annual sum of 11 Pg C yr^{-1} GPP, accounting for ~10 % of the global terrestrial GPP (Chen et al. 2014). Crop cultivation and production vary substantially over space and time. Thus, an accurate quantification of cropland GPP is critical for global food security (Wheeler and von Braun 2013), biofuel production (Landis et al. 2008), and understanding variations in the terrestrial carbon cycle (Haberl et al. 2007).

Production Efficiency Models (PEMs) have been widely used to quantify the spatial-temporal GPP variations of terrestrial ecosystems using the satellite and climate data as inputs. The PEMs, originating from Monteith's theoretical concept about light use efficiency (LUE) (Monteith 1972a; Monteith and Moss 1977), estimate GPP as the product of the photosynthetically active radiation (PAR, MJ m^{-2}), the fraction of PAR absorbed by the vegetation (fPAR), and the conversion efficiency of absorbed PAR for carbon fixation (ε, g C MJ^{-1}) ($GPP=\varepsilon \times fPAR \times PAR$). The PEMs for croplands can be

classified into two categories based on fPAR and ε estimation methods. The first category calculates fPAR and ε separately. This approach has been applied in the Global Production Efficiency Model (GLO-PEM) (Prince and Goward 1995), the MODIS Daily Photosynthesis model (MODIS-PSN) (Running et al. 2000a), the C-Fix model (Veroustraete et al. 2002), and the Vegetation Photosynthesis Model (VPM) (Xiao et al. 2004a; Xiao et al. 2004b). The second type of PEMs, referred as the Greenness and Radiation (GR) model, uses the chlorophyll-related vegetation indices (VI_{chl}) as a proxy of ε×fPAR ($GPP \propto VI_{chl} \times PAR$) (Gitelson et al. 2006; Peng and Gitelson 2011, 2012; Peng et al. 2011; Wu et al. 2009; Zhang et al. 2014a; Zhang et al. 2015).

Challenges remain, however, in applying PEMs due to model structure and model inputs. Several attempts have been made to address the uncertainties from the PEM algorithm itself, including the assumption of linear response of photosynthesis to light intensity (Chen et al. 1999), constant maximum LUE for one ecosystem (Heinsch et al. 2006), the impacts of diffuse radiation (He et al. 2013; Zhang et al. 2012a), and the incomplete integration of environmental regulations (temperature, water, phenology etc.) to photosynthetic processes (Dong et al. 2015; Yuan et al. 2014). Most uncertainty analyses overlooked the potential impacts of model inputs on the application of PEMs to regional or global primary production monitoring.

Meteorological reanalysis data produces continuous and near real-time climate monitoring via data assimilation models, and has been the major climate input of PEMs for the large-scale primary production simulation (Feng et al. 2007; Running et al. 2004; Xiao et al. 2011; Yuan et al. 2010). Studies have reported that the meteorological reanalysis data can be spatially and temporally biased from the ground observations, in

particular for downward shortwave radiation when estimating PAR (Babst et al. 2008; Cai et al. 2014; Decker et al. 2012; Troy and Wood 2009; Zhang et al. 2007; Zhao et al. 2013a; Zhao et al. 2006; Zib et al. 2012). PEMs have been found very sensitive to the accuracy of climate reanalysis variables (Cai et al. 2014; Heinsch et al. 2006; Zhang et al. 2007; Zhao et al. 2006). For example, Heinsch et al. (2006) reported that the errors associated with the standard MODIS GPP product were mainly attributed to the NASA's Data Assimilation Office (DAO) reanalysis data. Previous sensitivity analyses of PEMs to climate inputs focused on global reanalysis data, the spatial resolution of which is too coarse to delineate the local climatic variations.

The North America Regional Reanalysis (NARR) by the National Centers for Environmental Prediction (NCEP) is the only currently available long-term regional reanalysis data. Compared with the NCEP global reanalysis datasets, the NARR substantially improves the spatio-temporal resolutions along with the accuracy of climate variables (Mesinger et al. 2006) and could be an alternative climate driver of regional GPP estimates in particular for croplands, one of the most heterogeneous landscapes. There has been very limited research regarding the uncertainties of PEMs in relation to the NARR. Therefore, careful investigation of the accuracy of the NARR and its impacts on cropland GPP estimates at site level is an indispensable step prior to the large scale application of these tools.

The objectives of this study were to: (1) evaluate the accuracy of the NARR (air temperature and downward shortwave radiation) as compared to the in-situ observations from the AmeriFlux network at 8-day intervals; (2) adjust the NARR based on the statistical differences from in-situ meteorological measurements; and (3) quantify the

impacts of different climate inputs (in-situ meteorological data and the original and adjusted NARR data) on the GPP simulation for maize and soybean using the VPM at seven AmeriFlux crop sites (40 site-years).

4.2 Data and methods

4.2.1 NARR

The NARR is produced at a spatial resolution of 32 km and a temporal resolution of 3-hours. We obtained the NARR daily gridded air temperature (T_{NARR}) and downward shortwave radiation (R_{NARR}) from http://www.esrl.noaa.gov/psd/. The daily T_{NARR} and R_{NARR} for the pixels covering AmeriFlux sites were extracted for the available site-years at 44 AmeriFlux sites and were aggregated to 8-day intervals to match the temporal resolution of MODIS products.

4.2.2 MODIS land surface reflectance, vegetation indices products

This study used the 8-day 500 m MODIS Surface Reflectance product—MOD09A1 to derive vegetation indices. The time-series MOD09A1 data for the crop sites were extracted from the MODIS data portal at the Earth Observation and Modeling Facility, University of Oklahoma (http://www.eomf.ou.edu/visualization/manual/). The Enhanced Vegetation Index (EVI) and Land Surface Water Index (LSWI) were calculated for every 8-day observation using equations (4.1) and (4.2).

$$EVI = 2.5 \times \frac{\rho_{NIR_1} - \rho_{red}}{\rho_{NIR_1} + 6 \times \rho_{red} - 7.5 \times \rho_{blue} + 1} \quad (4.1)$$

$$LSWI = \frac{\rho_{NIR_1} - \rho_{SWIR_1}}{\rho_{NIR_1} + \rho_{SWIR_1}} \quad (4.2)$$

where ρ_{NIR_1}, ρ_{red}, ρ_{blue}, and ρ_{LSWI} are the MOD09A1 surface reflectance for NIR_1 (841-876 nm), red (620–670 nm), blue (459–479 nm), and $SWIR_1$ (1628–1652 nm), respectively. A two-step gap-filling procedure was applied to gap-fill bad-quality

observations within the time series of vegetation indices (Xiao et al. 2004a; Xiao et al. 2004b).

4.2.3 In-situ meteorological observations and CO_2 flux data

The AmeriFlux network consists of eddy covariance flux sites for monitoring the long-term ecosystem-scale exchange of carbon, energy, and water in North America (Baldocchi et al. 2001). Meteorological observations such as temperature, precipitation, and radiation are also collected at these sites.

We obtained all available 8-day Level 4 data of the AmeriFlux sites covering the conterminous U.S. from http://ameriflux.lbl.gov/Pages/default.aspx (Figure 4.1). The Level 4 data included air temperature (T_{EC}), downward shortwave radiation (R_{EC}), and CO_2 flux data. This study used the standardized GPP (GPP_{EC}), which was partitioned from net ecosystem CO_2 exchange (NEE). By screening quality flags, only the most reliable observations were chosen for analysis. T_{EC} and R_{EC} from 37 non-crop sites (139 site-years) were used to evaluate and to adjust the NARR, if there were large biases. A total of 23 site-years of T_{EC} and R_{EC} and 40 site-years of GPP_{EC} from seven crop sites were used to validate the adjusted NARR and to evaluate the VPM-simulated GPP, respectively (Table 4.1). The crop sites were located in the U.S. Midwest corn and soybean belt, and were under different agricultural management practices. US-NE1 was a continuous irrigated maize site and US-NE2 was an irrigated maize/soybean rotation site. The other five sites were rainfed rotation sites. The detailed descriptions about these sites can be found in site specific publications (Griffis et al. 2005; Meyers and Hollinger 2004; Verma et al. 2005).

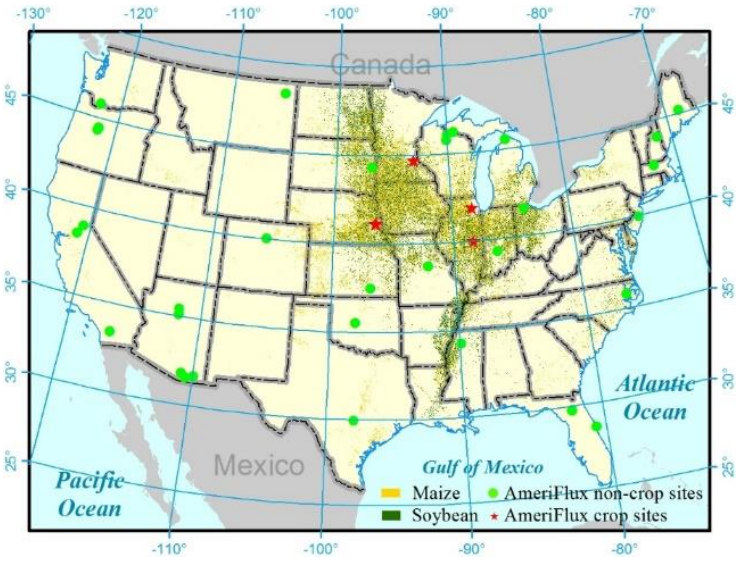


Figure 4.1 Location of the AmeriFlux eddy flux sites. Circles denote the non-crop sites for accuracy assessment of the NARR and stars denote the crop sites used to evaluate the VPM-based GPP estimates. The base map is the 2013 Cropland Data Layer (CDL) from the National Agricultural Statistics Service (NASS)

It is important to mention that a direct comparison between the in-situ AmeriFlux observations and the NARR data without considering the differences of spatial scales might introduce some uncertainties. The in-situ observations can be affected by local environment conditions (terrain, hydrology, land cover etc.), while the NARR might be too coarse to delineate local environment variations. However, the AmeriFlux is currently the best available dataset providing high-quality and synchronized observation of radiation, temperature, water and carbon fluxes under standard protocols.

Table 4.1 A summary description of the AmeriFlux eddy flux crop sites

Site ID	Latitude	Longitude	Years of T_{EC}[a], R_{EC}[b]	Crop type	Years of GPP_{EC}[c]
US-NE1	-96.4766	41.165	2002-2012	Irrigated maize	2002–2005, 2007–2012
US-NE2	-96.4701	41.1649	2001-2012	Irrigated maize	2001, 2003, 2005, 2007, 2009–2012
				Irrigated soybean	2002, 2004, 2006, 2008
US-NE3	-96.4396	41.1797	2001-2012	Rainfed maize	2001, 2003, 2005, 2009, 2011
				Rainfed soybean	2002, 2004, 2008, 2010
US-RO1	-93.0898	44.7143	2004-2006	Rainfed maize	2005
				Rainfed soybean	2006
US-RO3	-93.0893	44.7217	2004-2006	Rainfed maize	2005
US-IB1	-88.2904	40.0062	2006-2007	Rainfed maize	2006
				Rainfed soybean	2007
US-Bo1	-88.2227	41.8593	2001-2006	Rainfed maize	2005
				Rainfed soybean	2002, 2004, 2006

[a] and [b] air temperature and downward shortwave radiation observed from the AmeriFlux eddy flux sites

[c] 8-day Level-4 GPP estimates from the AmeriFlux eddy flux sites

4.2.4 The Vegetation Photosynthesis Model (VPM)

The VPM is one PEM based on the conceptual partition of the light absorption by chlorophyll pigments and nonphotosynthetic vegetation (NPV such as branches, trunks, or senescent leaves) (Xiao et al. 2004a; Xiao et al. 2004b). The VPM defines the fPAR as the fraction of PAR absorbed by plant chlorophyll ($fPAR_{chl}$):

$$GPP = \varepsilon \times fPAR_{chl} \times PAR \tag{4.3}$$

$$fPAR_{chl} = EVI \tag{4.4}$$

$$\varepsilon = \varepsilon_0 \times T_{scalar} \times W_{scalar} \tag{4.5}$$

where PAR is calculated as 0.45 × R (R, downward shortwave solar radiation); $fPAR_{chl}$ is equivalent to EVI; Light use efficiency, ε , is estimated as a function of the maximum light use efficiency (ε_0), temperature (T_{scalar}) and water condition (W_{scalar}). The ε_0 values of 3.12 g C MJ^{-1} for maize (Kalfas et al. 2011a) and 1.75 g C MJ^{-1} for soybean (Wagle et al. 2015) were used in this study.

The effect of temperature scalar (T_{scalar}) on GPP is calculated using the equation from the Terrestrial Ecosystem Model (Raich et al. 1991):

$$T_{scalar} = \begin{cases} \frac{(T-T_{min})(T-T_{max})}{[(T-T_{min})(T-T_{max})]-(T-T_{opt})^2}, & T_{min} \le T \le T_{max} \\ 0, & T \le T_{min},\ T \ge T_{max} \end{cases} \tag{4.6}$$

where T is 8-day mean air temperature; T_{min}, T_{opt}, and T_{max} are minimum, optimum, and maximum temperatures for vegetation photosynthesis, respectively, and were set to 10 °C, 28 °C, 48 °C for maize (Kalfas et al. 2011a), and -1 °C, 28 °C, 50 °C for soybean (Wagle et al. 2015).

The effect of water scalar (W_{scalar}) on GPP is calculated with LSWI:

$$W_{scalar} = \begin{cases} \frac{1+LSWI}{1+LSWI_{max}}, & LSWI > 0 \\ LSWI + LSWI_{max}, & LSWI \le 0 \end{cases} \tag{4.7}$$

where $LSWI_{max}$ is the maximum LSWI during growing season.

This study used the VPM to simulate three sets of GPP_{VPM}: $GPP_{VPM(EC)}$, $GPP_{VPM(NARR)}$, and $GPP_{VPM(adjNARR)}$, using T and R from eddy flux sites (T_{EC}, R_{EC}), the NARR (T_{NARR}, R_{NARR}), and the adjusted NARR (T_{NARR}, $R_{adjNARR}$), respectively.

4.2.5 Statistical analysis

To quantify the differences between T_{NARR} and T_{EC}, R_{NARR} and R_{EC}, correlation coefficient (ρ), ratio of standard deviation (σ_{ratio}), bias, and root-mean-square-error (RMSE) were calculated for each non-crop site-year. The histogram of each statistics was summarized for all non-crop site-years to characterize the overall accuracy of T_{NARR} and R_{NARR}.

Mean Squared Error (MSE) was calculated for T_{NARR} and R_{NARR} of each site-year, and decomposed into three terms (Decker et al. 2012; Gupta et al. 2009), such that

$$MSE = 2\sigma_{NARR}\sigma_{EC}\,(1-\rho) + (\sigma_{NARR}-\sigma_{EC})^2 + (\mu_{NARR}-\mu_{EC})^2 \quad (4.8)$$

where μ_{EC} and σ_{EC} are the mean and standard deviation for the in-situ observations, respectively. μ_{NARR} and σ_{NARR} are the mean and standard deviation for the NARR, respectively. The first, second, and third terms in equation (4.8) were represented in ternary diagrams to concisely visualized the contribution of correlation (ρ), consistency of variation (σ_{ratio}), and bias (bias and RMSE) to the overall disagreements between T_{NARR} and T_{EC} and between R_{NARR} and R_{EC}.

The simple linear regression between R_{EC} and R_{NARR} was also calculated for all non-crop site-years ($R_{EC} = \alpha \times R_{NARR}$). On the basis of the spatial pattern of regression coefficients (α), an empirical ratio-based adjustment was applied to R_{NARR} at the crop sites ($R_{adjNARR}$). Relative error (RE), RMSE, regression coefficient (α), and coefficient of

determination (R^2) of the simple linear regression between R_{NARR} and R_{EC}, and $R_{adjNARR}$ and R_{EC} were obtained to quantify the adjustment performance.

This study implemented a top-down strategy to evaluate the impact of different climate inputs on GPP_{VPM}. First, the statistics factors described above were used to quantify how $GPP_{VPM(EC)}$, $GPP_{VPM(NARR)}$, and $GPP_{VPM(adjNARR)}$ matched GPP_{EC} for individual crops. Second, the similarities between GPP_{VPM} and GPP_{EC} across individual crop-sites were evaluated using Taylor diagrams. Taylor diagrams provide a statistical summary of the similarity of variability pattern (ρ), the agreement of the variability amplitudes (represented by the ratio of normalized standard deviation, $\bar{\sigma}_{ratio}$), and the centered RMSE between the modeled results and the observations (Gleckler et al. 2008; Taylor 2001). In addition, annual mean RMSE of GPP_{VPM} was calculated for each crop site-year.

4.3 Results

4.3.1 Comparison of air temperature

T_{NARR} agreed well with T_{EC} for almost all non-crop site-years. T_{NARR} was significantly correlated with T_{EC} (ρ > 0.95 for 139 site-years, Figure 4.2). In addition, T_{NARR} showed a similar amplitude of variation as in T_{EC}, as ~82 % of site-years had σ_{ratio} within ±10 % error. T_{NARR} was mostly overestimated with a positive bias of 0.5–2.5 °C and a mean RMSE of 1.67 °C. The simple linear regression confirmed the good agreement between T_{NARR} and T_{EC}. T_{NARR} showed a strong linear regression with T_{EC} (α across 129 site-years was in a range of 1 ± 0.1, R^2 > 0.95, p < 0.001). MSE was determined by both the bias and correlation, as the contribution of bias and correlation was over 0.8 at 86 % of the site-years (Figure 4.3).

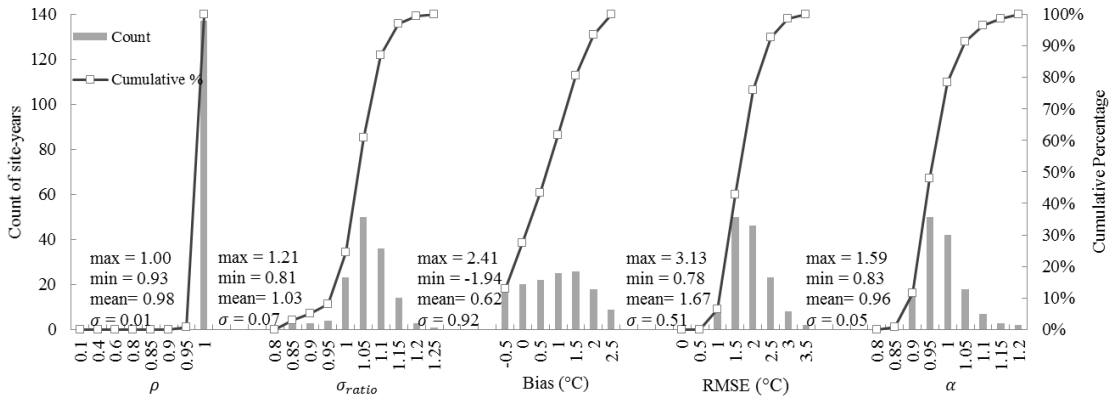


Figure 4.2 Distribution histograms of correlation coefficient (ρ), ratio of standard deviation (σ_{ratio}), bias, root-mean-square-error (RMSE), and regression coefficient (α) for 8-day air temperature from AmeriFlux (T_{EC}) and NARR (T_{NARR}) across the non-crop site-years

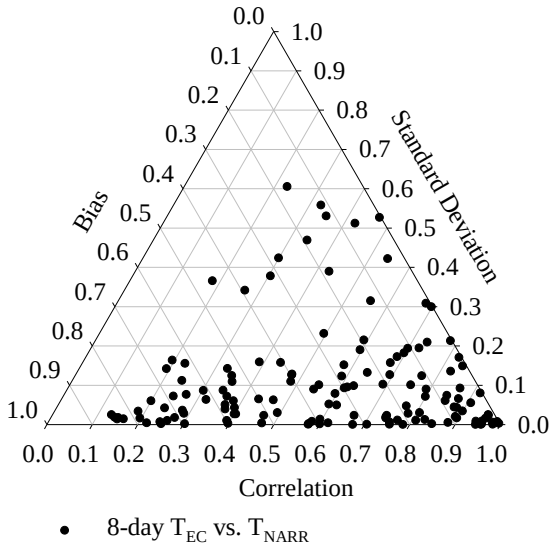


Figure 4.3 Contributions of correlation (ρ), consistency of variation (σ_{ratio}), and bias to the Mean Squared Error (MSE) for the 8-day NARR air temperature (T_{NARR}) across the non-crop site-years

T_{NARR} was also relatively accurate at the crop sites. The simple linear regression indicated that T_{NARR} agreed well with T_{EC} for all crop site-years (α = 1.04, RE = 11.6 %, RMSE = 1.4 °C, R^2 = 0.99, Figure 4.4). T_{NARR} accounted for over 98 % of the seasonal

dynamics of T_{EC} for individual crop sites on annual scale (Table 4.2). α varied from 1.0 to 1.1 among the crop sites. RE and RMSE were -1.4–7.3 % and 1.2–1.7 °C, respectively. Considering the relatively high accuracy at non-crop and crop site-years, the 8-day T_{NARR} was used as the VPM input without any correction.

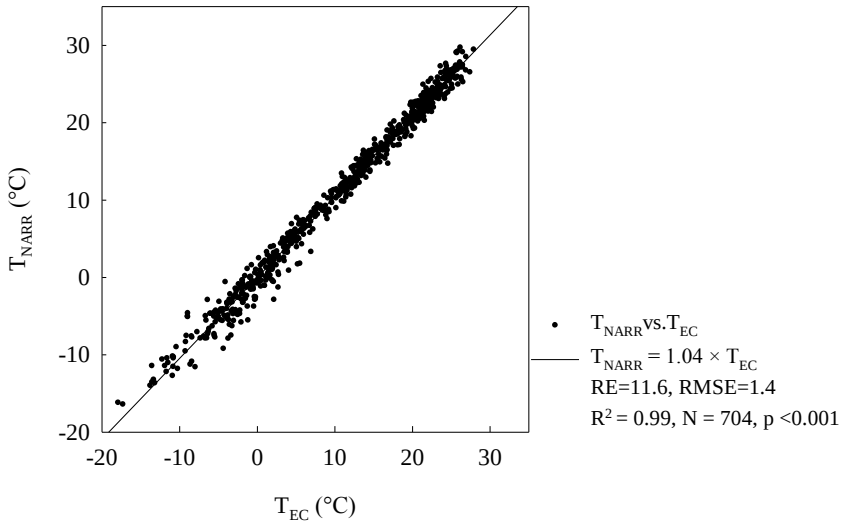


Figure 4.4 Comparisons of 8-day air temperature between AmeriFlux (T_{EC}) and NARR (T_{NARR}) across all crop site-years

Table 4.2 Statistics of the comparison of the 8-day NARR air temperature, original, and adjusted downward shortwave radiation with the AmeriFlux observations for the individual crop sites

Site ID	T_{EC}[a] vs. T_{NARR}[b]				R_{EC}[c] vs. R_{NARR}[d]				R_{EC} vs. $R_{adjNARR}$[e]		
	RE	RMSE	α	R^2	RE	RMSE	α	R^2	RE	RMSE	α
US-NE1/2/3	7.3±5.9	1.7±0.55	1.1±0.04	0.98	21.8±2.6	3.9±0.4	1.2±0.03	0.9±0.03	-2.5±2.1	1.6±0.02	0.97±0.02
US-RO1/3	-1.4±5.2	1.6±0.33	1.0±0.01	0.99±0.01	26.5±2.2	4.2±0.2	1.2±0.02	0.91±0.03	1.2±1.8	1.6±0.22	0.99±0.02
US-IB1	4.6±0.1	1.3±0.12	1.1±0.02	0.99	28.6±1.5	4.9±0.26	1.3	0.89±0.05	2.9±1.2	1.8±0.23	1.01
US-Bo1	7.1±2.0	1.2±0.17	1.0±0.01	0.99	22.7±7.6	3.8±0.78	1.2±0.08	0.9±0.05	-1.9±6.1	2.0±0.40	0.96±0.06

[a] and [b] air temperature of the AmeriFlux and NARR data (ºC)

[c, d] and [e] downward shortwave radiation of the AmeriFlux, the NARR before and after adjustment (MJ m^{-2} day^{-1})

4.3.2 Comparison of downward shortwave radiation

R_{NARR} was well correlated with R_{EC} (ρ > 0.9 at 94 % of the non-crop site-years, Figure 4.5). However, it was overestimated with σ_{ratio} > 1.1 at 67 % of the site-years. The bias was positive across all site-years on an average of 3.55 MJ m^{-2} day^{-1}. 60 % of the site-years had a RMSE of 3–5 MJ m^{-2} day^{-1}. The bias was the dominant contributor to MSE (Figure 4.6). The contribution of bias was > 0.5 at 133 of 139 site-years, indicating the disagreement between R_{NARR} and R_{EC} was systematic.

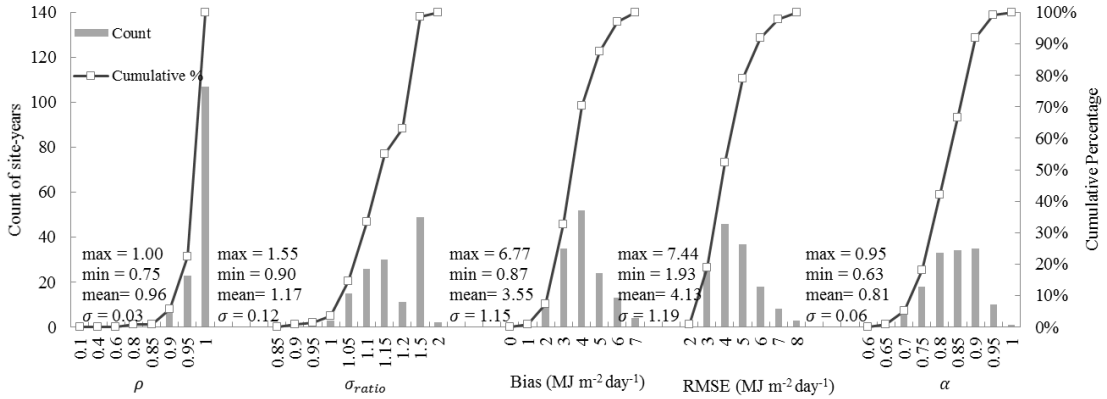


Figure 4.5 Distribution histograms of correlation coefficient (ρ), ratio of standard deviation (σ_{ratio}), bias, root-mean-square-error (RMSE), and regression coefficient (α) for 8-day downward shortwave radiation between AmeriFlux (R_{EC}) and NARR (R_{NARR}) across the non-crop site-years

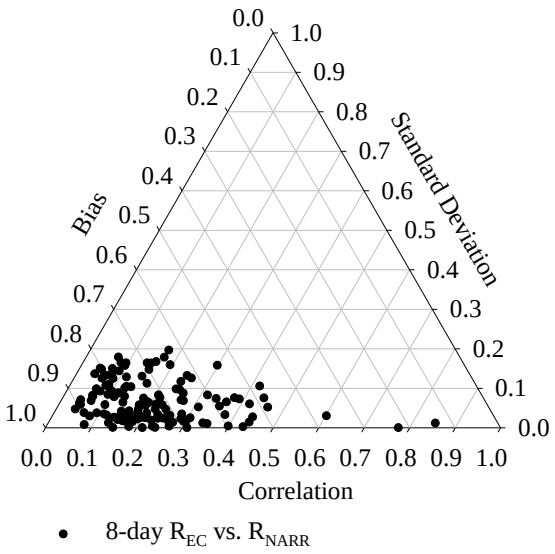


Figure 4.6 Contributions of correlation (ρ), consistency of variation (σ_{ratio}), and bias to the Mean Squared Error (MSE) for the 8-day NARR downward shortwave radiation (R_{NARR}) across the non-crop site-years

R_{NARR} showed a significant linear regression with R_{EC} at each non-crop site-year (Figure 4.5). However, α was quite variable (0.63–0.95). α slightly decreased with the latitude increasing or the longitude decreasing (Figure 4.7). α was more stable within the longitude range of 85–100 °W than it was across 40–47.5 °N for the region covering the crop sites (Figure 4.7 highlighted in gray). Thus, the median of α values (0.81) within the longitude of 85–100 °W was used as a ratio to adjust the bias of R_{NARR} at the crop sites.

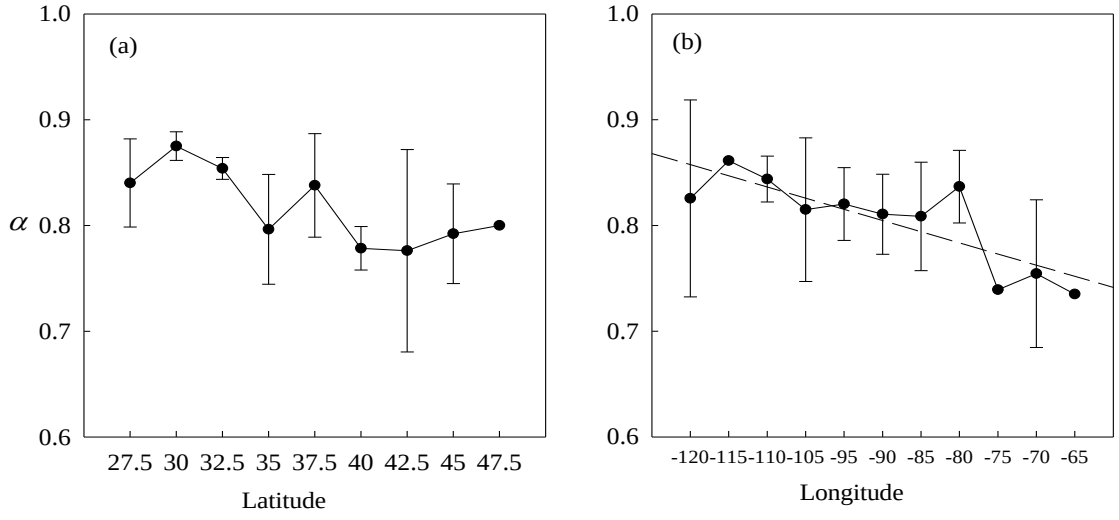


Figure 4.7 Spatial patterns of regression coefficient (α) between 8-day downward shortwave radiation from AmeriFlux (R_{EC}) and NARR (R_{NARR}), with geographical distribution of crop sites highlighted: (a) α averaged along the 2.5° latitude gradient and (b) α averaged along the 5° longitude gradient

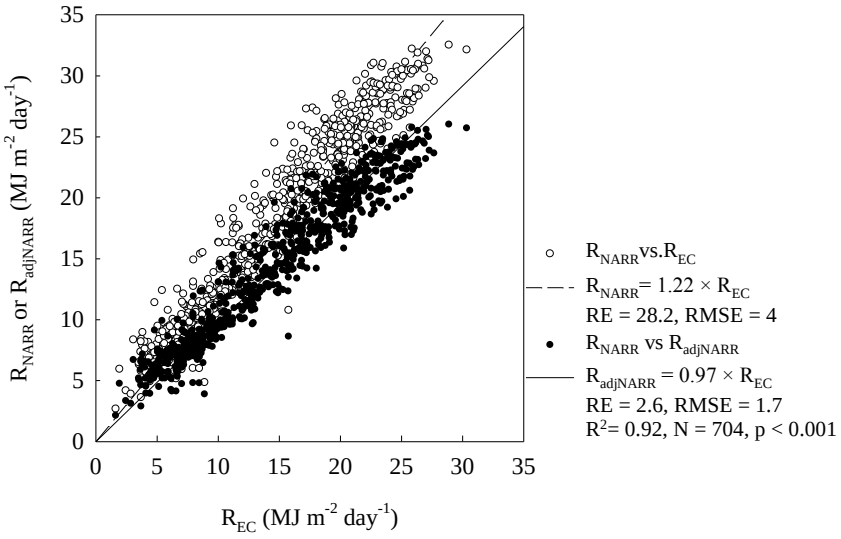


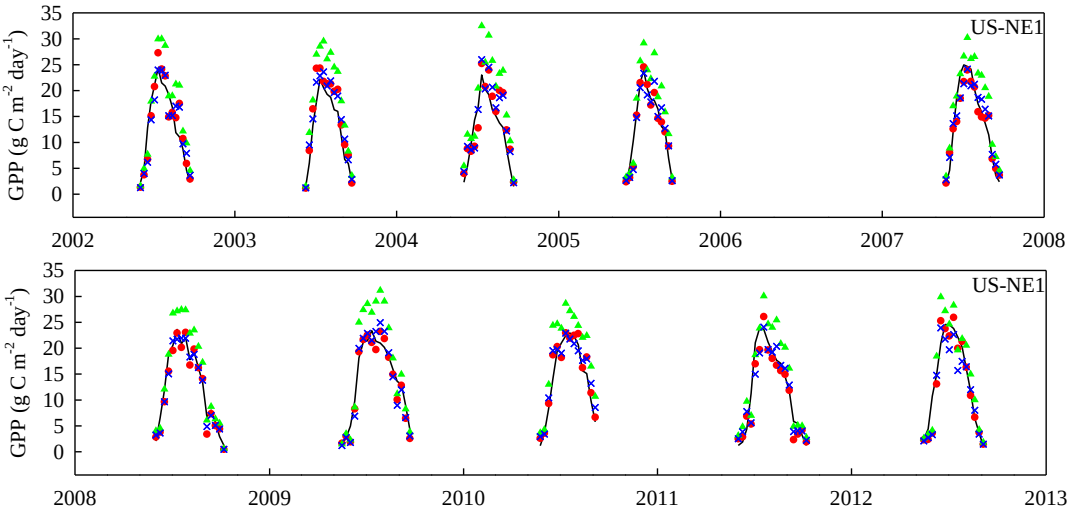
Figure 4.8 Comparisons of 8-day downward shortwave radiation between AmeriFlux (R_{EC}) and the NARR before and after adjustment (R_{NARR}, $R_{adjNARR}$) for all crop site-years

The adjustment substantially reduced the bias of R_{NARR} at the crop sites (Figure 4.8). R_{NARR} was overestimated by 28.2 % on average. $R_{adjNARR}$ evenly distributed along 1:1 line and RMSE was reduced to 1.7 MJ^{-2} day^{-1}.

R_{NARR} explained ~ 90 % of the variations of R_{EC} across each crop site (Table 4.2). Similar to the non-crop sites, R_{NARR} was strongly overestimated (RE > 22 %) at the crop sites. The annual RMSE varied from 3.8 MJ m^{-2} day^{-1} to 4.9 MJ m^{-2} day^{-1}. After the adjustment, α was close to 1, and RE and RMSE of $R_{adjNARR}$ decreased to -2.5–3 % and 1.6–2 MJ m^{-2} day^{-1}, respectively.

4.3.3 Comparison of VPM-based (GPP_{VPM}) and the flux tower-based (GPP_{EC}) estimates

The seasonal dynamics of $GPP_{VPM(EC)}$, $GPP_{VPM(NARR)}$, and $GPP_{VPM(adjNARR)}$ corresponded well with GPP_{EC} for both maize and soybean (Figure 4.9). At the leaf-on stage during late-May to June, GPP_{EC} started to exceed 1 g C m^{-2} day^{-1} and GPP_{VPM} also rose rapidly, and both reached a maximum at the peak growing season during late-July to early-August. After the crops matured and approached the harvest date in September, both GPP_{EC} and GPP_{VPM} began to decrease and were lower than 1 g C m^{-2} day^{-1}.



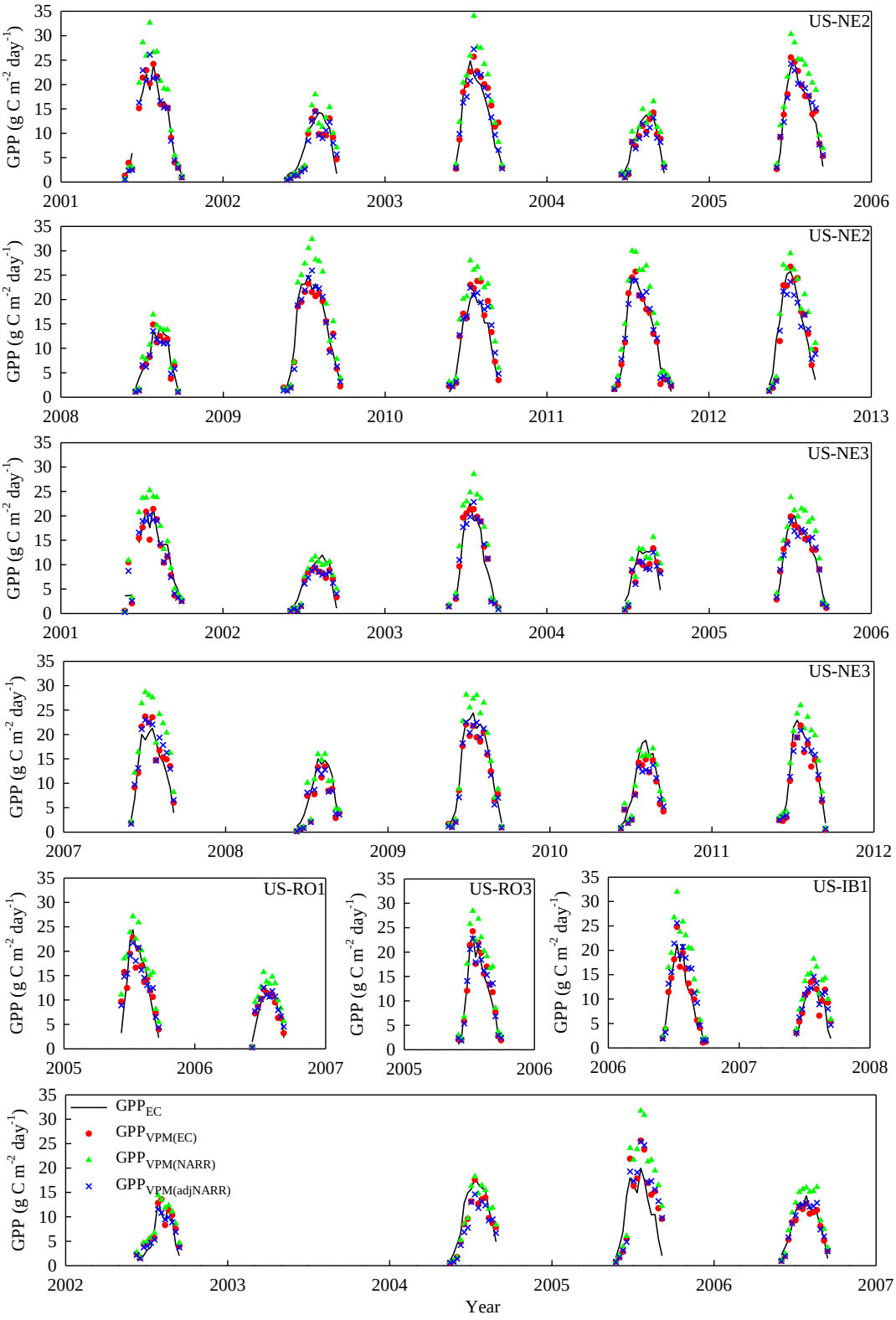
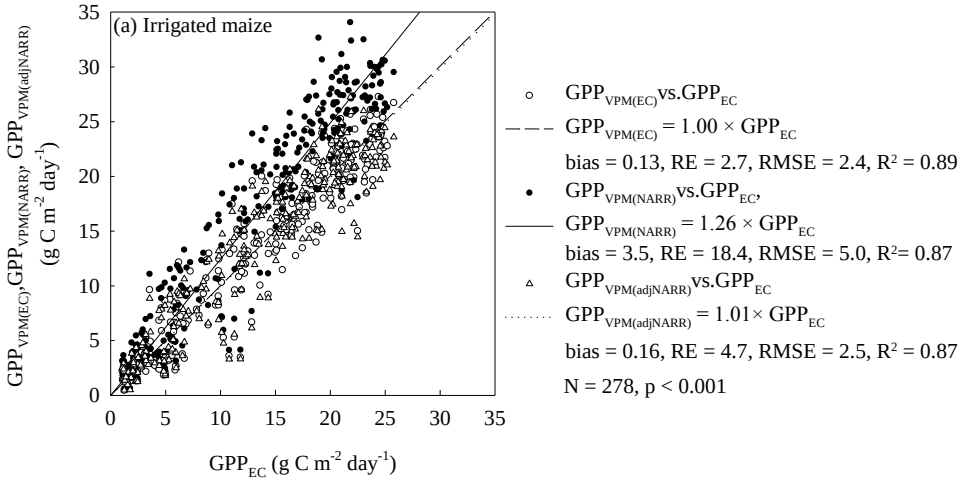
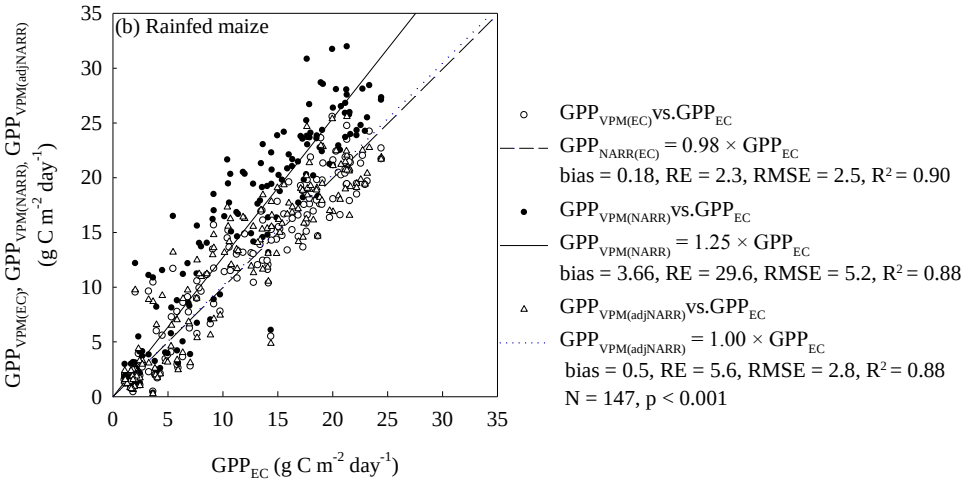
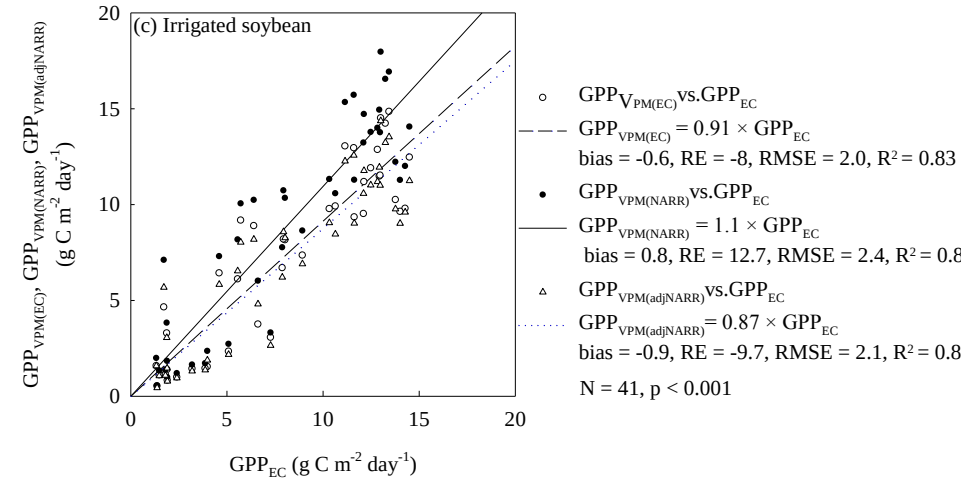


Figure 4.9 Seasonal dynamics and interannual variations of GPP_{EC}, $GPP_{VPM(EC)}$, $GPP_{VPM(NARR)}$, and $GPP_{VPM(adjNARR)}$ for the crop site-years. The soybean site-years are highlighted


(a) Irrigated maize
$GPP_{VPM(EC)}$, $GPP_{VPM(NARR)}$, $GPP_{VPM(adjNARR)}$ (g C m^{-2} day^{-1})
GPP_{EC} (g C m^{-2} day^{-1})
$GPP_{VPM(EC)}$ vs. GPP_{EC}
$GPP_{VPM(EC)}$ = 1.00 × GPP_{EC}
bias = 0.13, RE = 2.7, RMSE = 2.4, R^2 = 0.89
$GPP_{VPM(NARR)}$ vs. GPP_{EC},
$GPP_{VPM(NARR)}$ = 1.26 × GPP_{EC}
bias = 3.5, RE = 18.4, RMSE = 5.0, R^2= 0.87
$GPP_{VPM(adjNARR)}$ vs. GPP_{EC}
$GPP_{VPM(adjNARR)}$ = 1.01× GPP_{EC}
bias = 0.16, RE = 4.7, RMSE = 2.5, R^2 = 0.87
N = 278, p < 0.001


(b) Rainfed maize
$GPP_{VPM(EC)}$, $GPP_{VPM(NARR)}$, $GPP_{VPM(adjNARR)}$ (g C m^{-2} day^{-1})
GPP_{EC} (g C m^{-2} day^{-1})
$GPP_{VPM(EC)}$ vs. GPP_{EC}
$GPP_{NARR(EC)}$ = 0.98 × GPP_{EC}
bias = 0.18, RE = 2.3, RMSE = 2.5, R^2 = 0.90
$GPP_{VPM(NARR)}$ vs. GPP_{EC}
$GPP_{VPM(NARR)}$ = 1.25 × GPP_{EC}
bias = 3.66, RE = 29.6, RMSE = 5.2, R^2 = 0.88
$GPP_{VPM(adjNARR)}$ vs. GPP_{EC}
$GPP_{VPM(adjNARR)}$ = 1.00 × GPP_{EC}
bias = 0.5, RE = 5.6, RMSE = 2.8, R^2 = 0.88
N = 147, p < 0.001


(c) Irrigated soybean
$GPP_{VPM(EC)}$, $GPP_{VPM(NARR)}$, $GPP_{VPM(adjNARR)}$ (g C m^{-2} day^{-1})
GPP_{EC} (g C m^{-2} day^{-1})
$GPP_{VPM(EC)}$ vs. GPP_{EC}
$GPP_{VPM(EC)}$ = 0.91 × GPP_{EC}
bias = -0.6, RE = -8, RMSE = 2.0, R^2 = 0.83
$GPP_{VPM(NARR)}$ vs. GPP_{EC}
$GPP_{VPM(NARR)}$ = 1.1 × GPP_{EC}
bias = 0.8, RE = 12.7, RMSE = 2.4, R^2 = 0.8
$GPP_{VPM(adjNARR)}$ vs. GPP_{EC}
$GPP_{VPM(adjNARR)}$ = 0.87 × GPP_{EC}
bias = -0.9, RE = -9.7, RMSE = 2.1, R^2 = 0.8
N = 41, p < 0.001

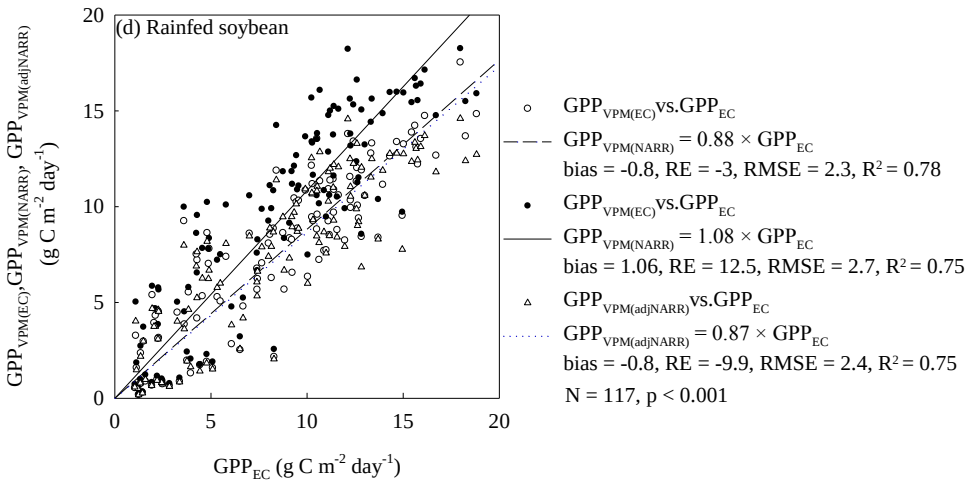


Figure 4.10 Comparisons of $GPP_{VPM(EC)}$, $GPP_{VPM(NARR)}$, and $GPP_{VPM(adjNARR)}$ with GPP_{EC} for individual crop: (a) irrigated maize, (b) rainfed maize, (c) irrigates soybean, and (d) rainfed soybean

The relationships between GPP_{VPM} and GPP_{EC} for individual crop types were evaluated through simple linear regression models (Figure 4.10). For irrigated and rainfed maize, both $GPP_{VPM(EC)}$ and $GPP_{VPM(adjNARR)}$ agreed well with GPP_{EC}; but $GPP_{VPM(NARR)}$ was overestimated due to the positive bias of R_{NARR} (Figures 4.10a and 4.10b). $GPP_{VPM(EC)}$ accounted for 89 % of the variations of GPP_{EC}. $GPP_{VPM(NARR)}$ was also correlated well with GPP_{EC}, but it was overestimated by 18.4 % and 29.6 % for irrigated and rainfed maize, respectively. After adjusting R_{NARR}, α, RE, and RMSE for $GPP_{VPM(adjNARR)}$ were close to those of $GPP_{VPM(EC)}$. For irrigated and rainfed soybean, $GPP_{VPM(EC)}$ and $GPP_{VPM(adjNARR)}$ estimated GPP reasonably well with an underestimation < -10 % (Figures 4.10c and 4.10d). $GPP_{VPM(NARR)}$ over-predicted GPP_{EC} by ~13 % for irrigated and rainfed soybean.

The relationships between GPP_{VPM} and GPP_{EC} were further evaluated for maize through individual crop-sites and individual site-years (Figure 4.11a, 4.11b, and Table 4.3). $GPP_{VPM(EC)}$ and $GPP_{VPM(adjNARR)}$ showed reliable GPP estimates for the irrigated and

rainfed maize across the sites (Figure 4.11a and 4.11b). Most sites had similar patterns and amplitudes of variability between $GPP_{VPM(EC)}$ and GPP_{EC} ($1 < \bar{\sigma}_{ratio} < 1.05$ and $0.95 < \rho < 0.98$, Figure 4.11a) with low annual mean RMSEs (ca. 1.5–2.4 g C m^{-2} day^{-1}, Table 4.3). $GPP_{VPM(EC)}$ at RO1 and Bo1 didn't appear to adequately capture the amplitudes of variability of GPP_{EC} ($\bar{\sigma}_{ratio}$ = 0.7 and 1.3) as indicated by relatively low ρ (0.92 and 0.82) and high RMSE (3.2 g C m^{-2} day^{-1} and 4.9 g C m^{-2} day^{-1}). The discrepancies were due to the underestimation of $GPP_{VPM(EC)}$ during the peak growing season at RO1 and the significant overestimation of $GPP_{VPM(EC)}$ after the peak growing season at Bo1 (Figure 4.9). $GPP_{VPM(NARR)}$ simulated the phasing and timing of GPP_{EC} well (ρ was ca. 0.93–0.98). The RMSE of $GPP_{VPM(NARR)}$ (ca. 4.2–6.4 g C m^{-2} day^{-1}) was significantly higher than that of $GPP_{VPM(EC)}$ at most sites, indicating an overestimation caused the NARR. The adjustment of R_{NARR} resulted in similar patterns of $GPP_{VPM(adjNARR)}$ and $GPP_{VPM(EC)}$ at all sites, with a slight increase of RMSE (ca. 1.6–3.1 g C m^{-2} day^{-1}, Figures 4.11b and Table 4.3).

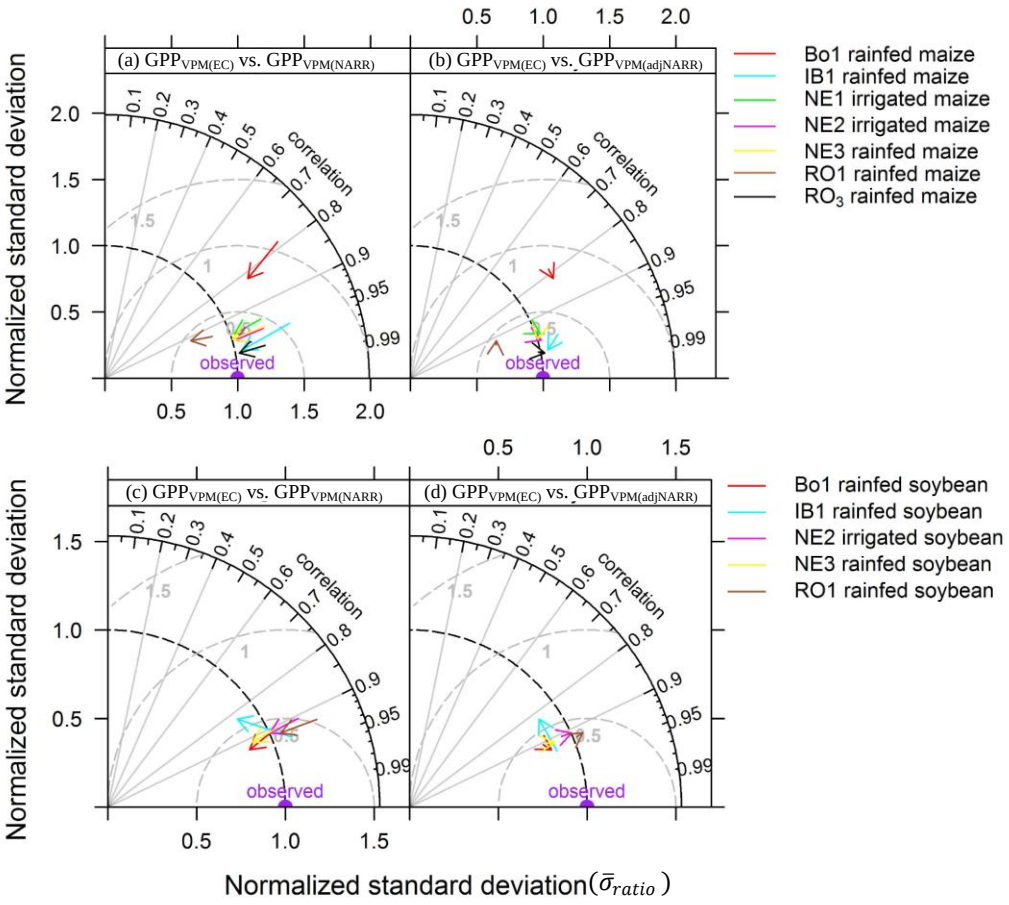


Figure 4.11 Performances of the VPM driven by three climate datasets for individual crop-site: (a) and (b) $GPP_{VPM(EC)}$ vs. $GPP_{VPM(NARR)}$ and $GPP_{VPM(EC)}$ vs. $GPP_{VPM(adjNARR)}$ for the irrigated and rainfed maize; (c) and (d) $GPP_{VPM(EC)}$ vs. $GPP_{VPM(NARR)}$ and $GPP_{VPM(EC)}$ vs. $GPP_{VPM(adjNARR)}$ for the irrigated and rainfed soybean. The locations of the heads and tails of arrows quantify how GPP_{VPM} matches with GPP_{EC}, and the arrows show how the agreement of GPP_{VPM} with GPP_{EC} changes using different climate inputs. The distance to the origin is the ratio of the standard deviations of GPP_{VPM} and GPP_{EC} (Normalized standard deviation, $\bar{\sigma}_{ratio}$). The azimuthal angle is the correlation (ρ) showing the similarity of variation patterns between GPP_{VPM} and GPP_{EC}. The most ideal GPP_{VPM} estimate is the point "observed" with $\bar{\sigma}_{ratio}$ = 1 and ρ = 1

Table 4.3 A summary of the performances of the VPM driven by three sets of climate inputs at the crop sites

Site ID	Crop type	$GPP_{VPM(EC)}$[a]			$GPP_{VPM(NARR)}$[b]			$GPP_{VPM(adjNARR)}$[c]		
		ρ	$\bar{\sigma}_{ratio}$	RMSE	ρ	$\bar{\sigma}_{ratio}$	RMSE	ρ	$\bar{\sigma}_{ratio}$	RMSE
US-NE1	Irrigated maize	0.95	1.03	2.4±0.7	0.93	1.25	5.0±1.1	0.93	1.00	2.7±0.6
US-NE2	Irrigated maize	0.96	1.02	2.2±0.8	0.95	1.24	4.8±0.6	0.95	0.99	2.3±0.6
	Irrigate soybean	0.91	1.00	2.0±0.6	0.91	1.18	2.3±0.7	0.90	0.94	2.0±0.6
US-NE3	Rainfed maize	0.95	1.00	2.1±0.5	0.95	1.26	4.2±1.3	0.95	1.01	2.2±0.5
	Rainfed soybean	0.91	0.89	2.6±0.4	0.91	1.05	2.2±0.3	0.90	0.84	2.8±0.5
US-RO1	Rainfed maize	0.92	0.7	3.2	0.93	0.86	4.8	0.93	0.69	3.1
	Rainfed soybean	0.92	1.06	1.4	0.92	1.27	3.4	0.92	1.02	1.5
US-RO3	Rainfed maize	0.98	1.03	1.5	0.97	1.23	4.3	0.98	0.98	1.6
US-IB1	Rainfed maize	0.97	1.06	1.5	0.96	1.45	6.4	0.96	1.16	3.1
	Rainfed soybean	0.83	0.88	2.3	0.93	1.11	4.1	0.93	0.89	1.9
US-Bo1	Rainfed maize	0.82	1.31	4.9	0.78	1.66	8.6	0.78	1.33	5.5
	Rainfed soybean	0.93	0.86	2.0	0.91	1.03	2.5	0.91	0.83	2.3

The relationships between GPP_{VPM} and GPP_{EC} were also evaluated for soybean through individual crop-sites and individual site-years (Figure 4.11c, 4.11d, and Table 4.3). $GPP_{VPM(EC)}$ and $GPP_{VPM(adjNARR)}$ matched GPP_{EC} reasonably well. The variability of $GPP_{VPM(EC)}$ was similar to that of GPP_{EC} ($0.83 < \rho < 0.93$, Figure 4.11c). NE2 and RO1 had a good agreement between $GPP_{VPM(EC)}$ and GPP_{EC}, as $\bar{\sigma}_{ratio}$ was close to 1 showing a low RMSE (1.4–2.0 g C m^{-2} day^{-1}, Table 4.3). At other sites (NE3, IB1, and Bo1), $GPP_{VPM(EC)}$ underestimated the variability of GPP_{EC} ($0.85 < \bar{\sigma}_{ratio} < 0.9$, Figure 4.11c) with a high RMSE (2.0–2.6 g C m^{-2} day^{-1}). $GPP_{VPM(NARR)}$ correlated well with GPP_{EC} ($0.9 < \rho < 0.94$). However, the $\bar{\sigma}_{ratio}$ of $GPP_{VPM(NARR)}$ was larger than that of $GPP_{VPM(EC)}$ caused by the positive bias of R_{NARR}. After adjusting the bias of R_{NARR}, $GPP_{VPM(adjNARR)}$ matched GPP_{EC} better than did $GPP_{VPM(NARR)}$ (Figure 4.11d).

4.4 Discussion

4.4.1 Uncertainties of the NARR air temperature

T_{NARR} has been assumed to be relatively accurate in the studies of drought monitoring and the response of vegetation to climate change (Karnauskas et al. 2008; Karnieli et al. 2010; Wang et al. 2011). In this study, the 8-day T_{NARR} was mostly overestimated with a mean bias of 0.62 °C. This was consistent with the previous finding that T_{NARR} was biased warm at monthly intervals (Jiang and Yang 2012). In general, the 8-day T_{NARR} agreed well with the in-situ observations across non-crop and crop site-years with the mean RMSE of 1.67 °C and 1.4 °C, respectively, showing relatively higher accuracy than other global reanalysis datasets (DAO, ECMWF, NCEP, MERRA) investigated by Zhao et al. (2006) and Decker et al. (2012).

4.4.2 Uncertainties of the NARR downward shortwave radiation

This study made an assumption that R_{EC} were ground truth. However, the errors or uncertainties associated with in-situ radiation observations also contributed to the differences between R_{NARR} and R_{EC}. R_{EC} at the AmeriFlux is measured by different pyranometers. The errors from pyranometers including instrument deployment and maintenance (leveling and shading) and sensor response errors such as thermal offset (Bush et al. 2000; Reda et al. 2005) determined the errors of R_{EC}. The errors of R_{EC} are subtle compared with the R_{NARR} biases, but one shouldn't neglected their impacts considering the significant decay of long-term sensor stability (Stanhill and Cohen 2001).

A number of studies have evaluated the monthly R_{NARR} at individual sites. Walsh (2009) evaluated the monthly R_{NARR} at the Alaska Barrow site and found that it had a lower bias (2.6 MJ m^{-2} day^{-1}) than did NCEP/NCAR (3.7 MJ m^{-2} day^{-1}). Kennedy et al.

(2011) concluded that the bias of monthly R_{NARR} varied with sky conditions at the Atmospheric Radiation Measurement Program (ARM) Southern Great Plain (SGP) site. Markovic et al. (2009) reported that a systematic bias of monthly R_{NARR} in summer (5.3 MJ m^{-2} day^{-1}) was larger than that in winter (2.5 MJ m^{-2} day^{-1}). These evaluations implied that R_{NARR} had a large span of positive biases. However, their results cannot represent the overall accuracy of R_{NARR} at continental scale using limited sites. A recent study did a large-scale assessment of monthly R_{NARR} using 24 FLUXNET sites showing that R_{NARR} exhibited a positive bias of 3.2 MJ m^{-2} day^{-1} (Zhao et al. 2013a). The ideal temporal interval of climatic drivers for ecological models should be finer, i.e. hourly, daily, or weekly intervals, to demonstrate the diurnal or seasonal dynamics of carbon and energy fluxes (Abatzoglou 2013; Huntzinger et al. 2013; Wei et al. 2013). Thus, we evaluated the accuracy of R_{NARR} at 8-day intervals and regional scale using all available AmeriFlux sites. The 8-day R_{NARR} well represented the seasonal dynamics of 8-day R_{EC}. Similar to monthly R_{NARR}, the bias of the 8-day R_{NARR} was positive and systematic with a large range across the U.S.. The systematic overestimation of R_{NARR} is mainly caused by the insufficient simulation of light extinction caused by clouds, aerosols, and water vapor in the radiative transferring models (Kennedy et al. 2011; Markovic et al. 2009; Zhao et al. 2013a), and other topographical factors (i.e. elevation, slope, and aspect).

Empirical or semi-empirical approaches are applied to correct the bias of $R_{NARR.}$ The empirical approach develops the linear statistical regression model between the reanalysis and in-situ observations, then applies the model to other locations (Feng et al. 2007; Qian et al. 2006; Xiao et al. 2014a). The empirical approach ignores the spatio-temporal variations in the R_{NARR} bias. Some studies developed the semi-empirical

approach to account the impacts of clouds and topographical factors in the regression models (Schroeder et al. 2009; Zhao et al. 2013a). We followed the empirical approach to calibrate R_{NARR}, and meanwhile considered the spatial variation of regression models.

Simply estimating PAR as a constant ratio of R_{NARR} can introduce uncertainties to PAR. Theoretically, the band range of downward shortwave radiation (0.3–2.8 μm) doesn't match that of PAR (0.4–0.7 μm) (Sakamoto et al. 2011). Moreover, the ratio of PAR to downward shortwave radiation is not constant, as it temporally changes with the local weather condition (Gonzalez and Calbo 2002; Jacovides et al. 2004; Papaioannou et al. 1993). Surface PAR datasets, such as the satellite-derived Global Land Surface Satellite (GLASS), might be an alternative PAR input for the regional and global ecological modeling (Cai et al. 2014; Eck and Dye 1991; Frouin and Pinker 1995; Jin et al. 2013; Pinker et al. 2010; Rubio et al. 2005; Zhao et al. 2013b).

4.4.3 Sensitivity of PEMs to various climate inputs

All analyses about the sensitivity of PEMs to climate inputs were focused on the PEM of the standard MODIS GPP product—the MODIS-PSN (Heinsch et al. 2006; Zhang et al. 2007; Zhao et al. 2006). These studies found that radiation, air temperature, and vapor pressure deficit (VPD) of the global reanalysis data were largely biased, and introduced significant errors to the standard MODIS GPP product. For instance, Zhao et al. (2006) found that the MODIS GPP showed significant differences when driven by DAO, NCAR, and ECMWF (> 20 Pg Cyr^{-1}). Heinsch et al. (2006) collected 38 site-years of GPP_{EC} from 15 AmeriFlux sites to evaluate the accuracy of MODIS GPP driven by DAO and in-situ meteorology, and annual GPP derived from DAO was 23 % higher than GPP_{EC} and the RE of the GPP derived from DAO was much larger than that of the GPP

derived from the in-situ meteorology. Note that these evaluations were conducted at monthly or longer intervals. Analyses on finer temporal scales such as weekly interval are needed in order to accurately evaluate the seasonal dynamics of the uncertainties of PEMs to climate data. Thus, we focused on quantifying the uncertainties of GPP_{VPM} to in-situ and NARR climate data at 8-day interval. The 8-day GPP_{VPM} driven by the in-situ meteorology, original and adjusted NARR data traced over 83–98 % of GPP_{EC} variations for individual site-years, confirming their capabilities to simulate the response of crop photosynthesis to the environment change (i.e. light, temperature, and water), and tracked the phenological phases well (i.e. leaf-on and leaf-off stages). Similar to the MODIS-PSN, climate inputs had a strong impact on the VPM for cropland GPP estimates. $GPP_{VPM(EC)}$ well estimated GPP_{EC} for individual crops, sites, and site-years. $GPP_{VPM(NARR)}$ significantly overestimated GPP_{EC} as R_{NARR} was positively biased. This study addressed two climate inputs of air temperature and downward shortwave radiation for the VPM. The accuracies of other climate variables (VPD, precipitation etc.) in reanalysis products might be more variable (Decker et al. 2012). Therefore, more uncertainties might be introduced to the PEMs that are driven by multiple climate variables.

4.4.4 Challenges in comparing GPP_{VPM} with GPP_{EC}

In one study like ours using GPP_{EC} to validate or constrain the GPP estimates from PEMs, two assumptions are often made: (1) GPP_{EC} is assumed to be accurate as the ground truth and (2) The eddy flux tower footprint is approximately equivalent to the image pixel. The uncertainties associated with these two assumptions, however, can

contribute to the discrepancies between the PEM-based GPP estimates (GPP_{VPM} in this study) and GPP_{EC}.

There are a number of errors or uncertainties (random and systematic) from eddy covariance measurements. Random errors are attributed to the stochastic nature of turbulence, sampling errors, instrument system, and variations in the flux footprint (Richardson et al. 2012). Systematic errors arise from the combination of the unmet underlying theoretical assumptions, instrument calibration, and data processing techniques (Falge et al. 2001; Papale et al. 2006; Richardson et al. 2012). Furthermore, the eddy covariance provides direct measurement of NEE and GPP_{EC} is estimated as the difference between NEE and ecosystem respiration (R_{eco}) using flux-partitioning approaches, which may also introduce large uncertainties in GPP_{EC} (Desai et al. 2008; Reichstein et al. 2005; Stoy et al. 2006). For example, Desai et al. (2008) found annual GPP_{EC} varied ~ 100 g C m^{-2} $year^{-1}$ among 23 partitioning methods. Thus, more efforts are needed to improve partitioning NEE into its gross components to help validate GPP in PEMs and other land surface models (Baldocchi et al. 2015).

The second assumption is questionable in heterogeneous landscapes. Limited by data availability, most PEMs are performed on 1 km spatial resolution of satellite images and might not represent the crop fields that towers are located in due to the mixed signals from other sub-pixel components. In this study, an in-situ landscape analysis showed that the heterogeneity of 500 m MODIS pixels was much improved over that of 1 km MODIS pixels at seven crop sites (Figure S4.1). 500 m MODIS pixels were mainly covered by the crop fields that the towers measured except US-RO3 and US-Bo1. Even though the uncertainties of the GPP comparison caused by heterogeneous landscapes were

diminished to some extent using the 500 m MODIS data in this study, further evaluations using high resolution images along with the downscaling techniques are required for implementing PEMs, especially at heterogeneous landscapes.

4.5 Conclusion

This study evaluated the uncertainties of the NARR surface meteorology and quantified the sensitivity of the VPM to the in-situ and NARR climate inputs at seven AmeriFlux crop eddy flux sites. Our results indicated that the bias of NARR resulted in considerable uncertainties in cropland GPP estimates. The 8-day NARR air temperature matched well with in-situ observations, but the NARR downward shortwave radiation showed large positive bias and led to the overestimation of GPP_{VPM}. An empirical correction of the NARR radiation improved the model performance.

The findings of this study confirm the good performance of the VPM on estimating maize and soybean GPP as long as meteorological inputs are accurate, and imply that the capability of the satellite-based PEMs for regional productivity monitoring at heterogeneous landscapes would be enhanced if the radiation of the regional reanalysis product can be improved to resolve the impacts of cloud cover and terrain. The proposed method to correct NARR radiation is limited to the crop sites in this study, and might not be applicable for other regions due to the large spatial variations of the NARR radiation bias. In addition to the meteorological data, further research is required to address the uncertainties of the PEM-based GPP estimates caused by other model inputs such as satellite data.

Supplementary materials

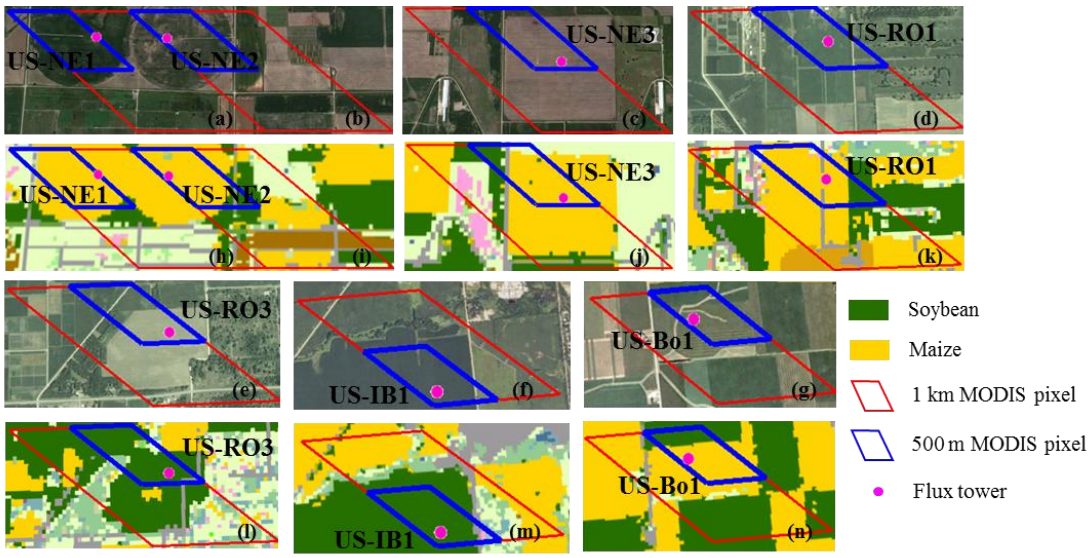


Figure S4.1 Landscape analyses for seven crop sites. (a) - (g) are landscapes from the high-resolution Google Earth images; (h) - (n) are land cover maps from the 2011 Cropland Data Layer (CDL), which are crop classification maps derived from high-resolution (30 m or 56 m) satellite data. The polygons with red and blue outlines are 1 km and 500 m MODIS pixels covering flux towers, respectively

Chapter 5: The 2012 flash drought threatened the U.S. Midwest agroecosystems

Abstract

In the summer of 2012, the United States (U.S.) Midwest, the most productive agricultural region in the world, experienced the most intense and widespread drought on record for the past hundred years. The 2012 summer drought, characterized as a "flash drought", developed in May with a rapid intensification afterwards and peaked in mid-July. Approximately 76 % of crop region and 60 % of grassland and pasture regions were under moderate to severe drought conditions. This study used multiple sources of evidence, i.e., in-situ AmeriFlux CO_2 data, spaital satellite observations of vegetation indices and solar-induced chlorophyll fluorescence (SIF), and scaled ecosystem modeling, to provide independent and complenmentary analyses of the impact of 2012 flash drought on productivity of major biomes in the U.S. Midwest. Three datasets consistently showed that (1) phenological activities of all biomes advanced 1-2 weeks earlier in 2012 compared to other years of 2010-2014, (2) the drought had a more severe impact on agroecoystems (crop and grassland) than on forests, and (3) the growth in agroecosystems was suppressed (i.e., reduction in vegetation indices, SIF, and gross primary production, GPP) from June to the end of the growing season. The Midwest-wide GPP modeling results showed that total regional GPP in 2012 was 1.76 Pg C $year^{-1}$, 63 Tg C $year^{-1}$ less than the mean GPP for 2010-2014. Agroecosystems, which accounted for 84 % of regional GPP assimilation, were impacted the most by 2012 drought with total GPP reduction of 9%, 7%, 6%, and 29% for maize (*Zea mays L.*), soybean (*Glycine max L.*), cropland, and grassland, respectively. As the frequency and severity of droughts

have been predicted to increase in the future, this study provides better insights into the impacts of flash droughts on vegetation productivity and carbon cycling of major biomes in the U.S. Midwest.

5.1 Introduction

Drought as an intermittent climate disturbance plays an important role in the earth systems, and its severity and frequency is predicted to increase in the future (Breshears et al. 2005; Dai 2011, 2013). Drought impacts on the structure, composition, and function of terrestrial ecosystems are often diverse and difficult to determine (Frank et al. 2015; Reyer et al. 2013; van der Molen et al. 2011). These drought associated impacts are not only immediate, for example via directly affecting plant photosynthesis and respiration (Ciais et al. 2005), but can exhibit time-lagged effects, such as increasing pest and pathogen-caused vegetation mortality, and changing plant species composition (Allen et al. 2010; Bigler et al. 2007; Phillips et al. 2010).

Recently, a term ‘flash drought’ recently became widely used to refer to the droughts with a rapid onset and intensification rate (Svoboda et al. 2002). Unlike those droughts that develop slowly, most climate models failed to early predict flash droughts (Hoerling et al. 2014). Moreover, flash droughts are likely to occur during the active growing season - the sensitive stage of crop development, and allow less time for agricultural community to respond to the changing conditions (Otkin et al. 2013). Thus, flash droughts are extremely devastating to agriculture. In 2012, the U.S. Midwest, one of the most intense agricultural areas in the world, experienced severe flash drought during the summertime. The extreme drought condition destroyed the major field crops, particularly field corn and soybeans, and caused large loss in livestock producers due to

forage and feed decreasing (Boyer et al. 2013; Mallya et al. 2013). Several studies have examined the impacts of droughts on vegetation greenness and productivity, and terrestrial carbon budgets at the regional and subcontinental scales (Ciais et al. 2005; Liu et al. 2014; Schwalm et al. 2012; Zhang et al. 2012c; Zhao and Running 2010). These studies, however, focused on the slowly developed droughts, and the assessment of the impacts of flash droughts on ecosystems is still lacking.

In general, three approaches have been applied to study the ecosystems' responses to drought: in-situ eddy flux data (Dunn et al. 2007; Granier et al. 2007; Noormets et al. 2010; Wolf et al. 2013), spatial satellite observations (e.g. vegetation indices) (Asner and Alencar 2010; Ji and Peters 2003; Vicente-Serrano 2007), and scaled ecosystem modelling (Liu et al. 2014; Williams et al. 2014; Zhao and Running 2010; Zscheischler et al. 2014). All of these approaches, however, have their own limitations. Although the eddy flux data can provide a relatively precise picture on the stand–scale functional response of vegetation to droughts, the number of sites is limited when spatially assessing the larger-scale drought impact, such as scales larger than flux tower footprints. While remote sensing and ecosystem modelling seem best suited to investigate large-scale drought effects, remote sensing can only show a view via the spectral reflectance changes expressed as vegetation indices instead of direct indicators of vegetation leaf area, biomass, and physiological functions. In addition, some ecosystem models have difficulty in accurately capturing the response of vegetation physiological processes to environmental stressors due to model structure and temporal and spatial resolution. Hence, an integrated analysis of in-situ eddy flux data, spatial remote sensing observations, and scaled ecosystem modelling approaches can overcome shortcomings of

each approach, and is indispensable to comprehensively reveal the cross-scale response of ecosystems to drought (Reichstein et al. 2007; Reyer et al. 2013).

Thus, the objectives of this study were to (1) evaluate the timing, severity, and spatial extent of 2012 flash drought over the U.S. Midwest and (2) investigate the impact of 2012 flash drought on the U.S. Midwest ecosystems with an integrated analysis of in-situ eddy flux data, spatial remote sensing observations, and scaled ecosystem modelling

5.2 Materials and methods

5.2.1 In-situ climate and CO_2 flux data from the AmeriFlux data

The AmeriFlux is an extensive network of eddy covariance flux sites that provide high-quality and synchronized observations of ecosystem-scale CO_2, water, and energy fluxes over North America. Sites in the U.S. Midwest were selected based on two criteria: 1) the landscape of site-located 500 m MODIS pixel was homogeneous and 2) data were available for both drought (2012) and non-drought years during 2010–2014. As no grassland AmeriFlux site was located in the U.S. Midwest, we used a nearby AmeriFlux grassland site (US-Kon) at the Konza Prairie, Kansas as a proxy. We obtained the gap-filled half-hourly Level-2 product of climate variables, soil water content (SWC), and CO_2 fluxes for four different-biome sites from the AmeriFlux website (http://ameriflux.lbl.gov/) (Figure 5.1, Table 5.1). We aggregated half-hourly data to 8-day intervals to match the temporal resolution of MODIS observations.

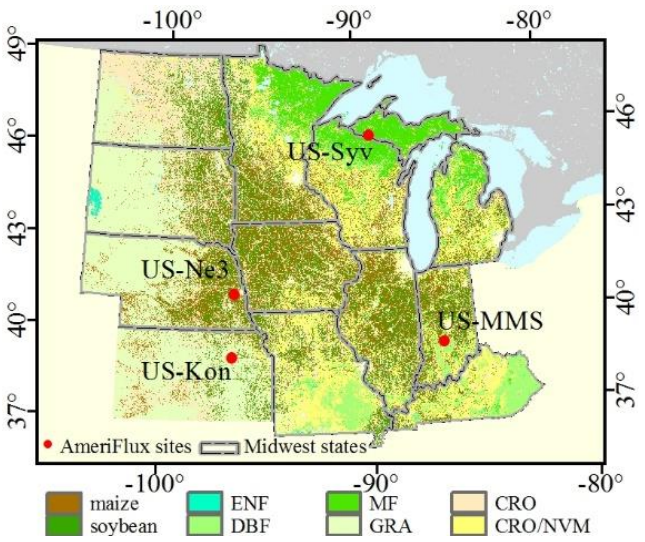


Figure 5.1 Land use and land cover map of the U.S. Midwest. Red circles represent AmeriFlux eddy covariance sites. Vegetation type is coded according to IGBP designations: ENF - evergreen needle forest, DBF - deciduous broadleaf forest, MF - mixed forest, GRA - grassland, CRO - cropland, and CRO/NVM - cropland/natural vegetation mosaic

5.2.2 The regional data for the 2012 drought assessment

We used spatial climate data from the PRISM (Parameter-evaluation Regressions on Independent Slopes Model) climate mapping program to delineate 2012 anomalous climate. The PRISM provides a set of fine-scale daily to annual climate variables from 1895-present, primarily for the Conterminous United States (Daly et al. 2000). The daily 4 km mean air temperature and precipitation during 2010–2014 were acquired from PRISM website (/www.prism.oregonstate.edu/), then were aggregated to 8-day intervals.

The Standardized Precipitation Index (SPI) was also used to quantify the drought intensity of the 2012 growing season. The SPI is a measure of probability of the observed precipitation based on historical records at a variety of time scales for both short- and long-term droughts (McKee et al. 1993). As this study focused on the short-term agricultural applications, the 1-month SPI (0.4 ° resolution) from the National Drought

Mitigation Center was obtained from the Western Regional Climate Center (http://www.wrcc.dri.edu/spi/spi.html). Based on the U.S drought classification scheme (http://droughtmonitor.unl.edu/aboutus/classificationscheme.aspx), a drought event occurs when the SPI reaches an intensity of -0.5 or less, and value ranges of -0.5 to -0.8, -0.8 to -1.3, - 1.3 to -1.6, -1.6 to -2.0 refer to abnormal, moderate, severe, and extreme drought, respectively.

5.2.3 The regional data for GPP estimation of the Vegetation Photosynthesis Model (VPM)

NCEP/NARR climate data. The North American Regional Reanalysis (NARR) by the National Centers for Environmental Prediction (NCEP) is a long-term regional reanalysis of the near-surface meteorological variables over North America (Mesinger et al. 2006). The NARR is produced at a spatial resolution of 32 km and a temporal resolution of 3-hours. We obtained the NARR 3-hourly air temperature and downward shortwave radiation from http://www.esrl.noaa.gov/psd/. The 3-hourly NARR data were aggregated to 8-day intervals and were spatially interpolated to 500 m (see Zhang et al. (2016) for interpolation algorithm in detail). As the NARR downward shortwave radiation is systematically positive biased, we further calibrated it ($R_{adjNARR} = 0.81 \times R_{NARR}$) as proposed by Jin et al. (2015).

MODIS surface reflectance and vegetation indices. Three vegetation indices, the Normalized Difference Vegetation Index (NDVI) (Tucker 1979b), Enhance Vegetation Index (EVI) (Huete et al. 1997a), and Land Surface Water Index (LSWI) (Xiao et al. 2004b), were calculated from the 8-day 500 m MODIS Surface Reflectance products collection 5 (MOD09A1 C5).

NASS Cropland Data Layer. The Cropland Data Layers (CDLs) provided by the US Department of Agriculture (USDA) National Agricultural Statistics Service (NASS) are the satellite-based crop-specific land cover datasets at a fine spatial resolution of 30 m or 56 m. The classification accuracies for maize and soybean on the CDLs are above 90 % (Boryan et al. 2011). The annual CDLs of 2010–2014 were aggregated to 500-m spatial datasets of areal fraction for maize and soybean.

MODIS land cover product. The MODIS Land Cover Type product (MCD12Q1 C5) describes land cover properties derived from annual satellite observations on Terra- and Aqua-MODIS. MCD12Q1 was used as base map to assign biome parameters when estimating GPP for non-maize/soybean crops and non-crop biomes, including pasture/grassland, mixed forest (MF), and deciduous broadleaf forest (DBF).

5.2.4 Other regional datasets

GOME-2 sun-induced chlorophyll fluorescence (SIF). SIF is derived from the spectral radiance at 740 nm measured by the Global Ozone Monitoring Experiment 2 (GOME-2) onboard the MetOp-A platform. GOME-2 SIF has shown a linear relationship with GPP for crop and grassland on both in-situ and regional levels (Guanter et al. 2014; Wagle et al. 2016; Zhang et al. 2014b).We used the weekly and monthly level 2 GOME-2 SIF (version 2.6) as an indirect indicator of the Midwest-wide GPP. Detailed description about the GOME-2 SIF retrievals can be found in Joiner et al. (2013).

USDA NASS agricultural inventory data ($Yield_{NASS}$). State-level yield statistics of maize, soybean, and pasture/grassland were acquired from the USDA NASS Quick Stats database (http://quickstats.nass.usda.gov/).

5.2.5 Regional GPP estimation of the VPM

The VPM simulates the terrestrial ecosystem GPP upon the concept of the light absorption by canopy greenness or chlorophyll (Xiao et al. 2004a; Xiao et al. 2004b):

$$GPP = \varepsilon \times fPAR_{chl} \times PAR \quad (5.1)$$

$$\varepsilon = \varepsilon_0 \times T_{scalar} \times W_{scalar} \quad (5.2)$$

where PAR is the photosynthetically active radiation; $fPAR_{chl}$ is the fraction of PAR absorbed by canopy greenness or chlorophyll. ε is the light use efficiency - a function of the maximum light use efficiency (ε_0), temperature (T_{scalar}), and water (W_{scalar}) stress conditions. The VPM parameters were derived from the satellite ($fPAR_{chl}$, W_{scalar}) and climate reanalysis (PAR, T_{scalar}) datasets. The details of VPM parameter estimations have been presented in Xiao et al. (2004b) and Xiao et al. (2004a).

For regional GPP simulation, the NASS CDLs allowed us to separate GPP contributions from maize and soybean for each 500 m pixel. To consider the differences in photosynthetic capacity between maize (C_4) and soybean (C_3) we applied in-situ derived ε_0 values of 3.12 g C MJ^{-1} (Kalfas et al. 2011a) for maize and 1.75 g C MJ^{-1} for soybean (Wagle et al. 2015). A biome parameter lookup table containing values of ε_0 and biome-specific physiological parameters for other vegetation types were referred to Zhang et al. (2016). The GPP of one pixel was estimated by area-weighted averaging the GPP contributions of sub-pixel components based on the area fraction maps of maize and soybean and MCD12Q1 land use datasets:

$$GPP_{VPM} = \sum_i f_i \times \varepsilon_{0i} \times fPAR_{chl} \times PAR \quad (5.3)$$

where f_i and ε_i are the area fraction and light use efficiency for maize, soybean, and other vegetation types (crop, grassland, DBF, MF, *etc.*). We simulated GPP over the U.S. Midwest from 2010 to 2014.

5.2.6 Data analysis

We compared 8-day daily air temperature and precipitation in 2012 with the mean values for 2010-2014 (excluding 2012) to track the onset and persistence of 2012 drought over the U.S. Midwest agroecosystem region. We also calculated the mean and minimum values of 1-month SPI and temperature and preciptiation anomalies to quantify the spatial extent and severity of drought in the 2012 growing seasoon.

The drought impact on ecoystems was first evluated at four AmeriFlux sites by analyzing the differences in climates, soil water, plant phenolgoy, and carbon fluxes duirng the 2012 growing season relative to mean values for 2010-2014. As long-term obervations are ususually not avaliable at the AmeriFlux sites, we used the mean of 2010–2014 (excluding 2012) or previous or later normal year in case of unavailability data for multiple years) as a proxy of 'normal' condition.

Multiple regional datasets, including the satellite-derived vegetation indices (NDVI, EVI, and LSWI), SIF, terrestrial carbon cycle simulations (GPP_{VPM}), and agricultural inventory ($Yield_{NASS}$), were applied to investigate the Midwest-wide ecosystem responses to drought. We quantified change in magnitudes and response dates of vegetation greenness and productivity during the 2012 drought compared to 2010–2014 at biome and pixel levels. The response date was defined as the first DOY, day of year, when vegetation indices, SIF, and GPP_{VPM} were lower than 2010 – 2014 mean (excluding 2012) for two or more consecutive 8-day intervals.

5.3 Results

5.3.1 Assessment of 2012 flash drought based on climate data

The spring of 2012 was the warmest spring since record in the U.S. Midwest. Air temperature averaged over the U.S. Midwest was 4 °C (February) and 9 °C (March) higher than the 2010–2014 means (Figure 5.2). After a period of near to normal early spring precipitation, drought rapidly developed in late spring/early summer (May). Drought severity abruptly intensified and continued to increase because of the significant precipitation deficit and heat wave. The drought peaked in June and July with the decreased precipitation by 62 % and 54 %, respectively, and increased temperature by 1.5 °C and 3 °C, respectively, relative to the 2010–2014 means. From September 2012, drought severity began to ameliorate due to near-normal precipitation. Overall, the accumulated precipitation during the 2012 growing season averaged over the U.S. Midwest was 235 mm (46 % below the 2010–2014 mean).

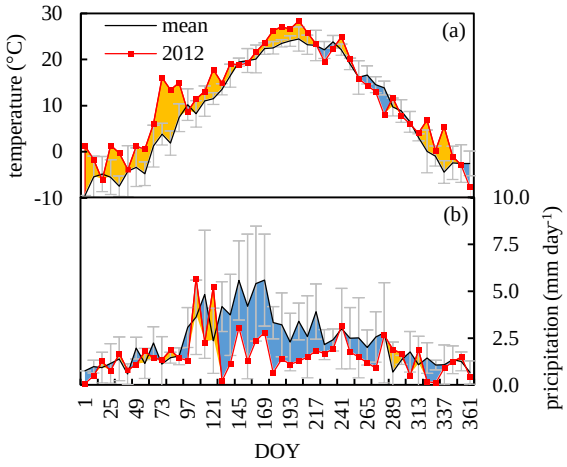


Figure 5.2 Comparison of time series of 8-day average air temperature (a) and precipitation (b) from PRISM over the U.S. Midwest between a drought year of 2012 and the mean for 2010-2014 (excluding 2012). Vertical error bars indicate mean ± standard deviation; shade areas represent 2012 anomalies relative to the mean values for 2010–2014

The severity of the 2012 growing season drought varied spatially across the U.S. Midwest (Figure 5.3). Most of the region, except the upper Great Lakes region and eastern states (Figure 5.3a), was abnormally dry and experienced extreme droughts due to the concurrence of high temperature and large water deficit (Figure, 3d, e). The southern region (~ 46 % of the U.S. Midwest), including large extents of South Dakota, Nebraska, Iowa, Missouri, Illinois, Indiana, and Kentucky, experienced extreme drought in June or July (Figures. 3b-c). In particular, 76 % of maize/soybean region suffered moderate to extreme drought with temperature and precipitation anomalies of 1.2 °C and -221 mm, respectively. Similarly, 59 % of grassland/pasture region was under extreme drought with temperature and precipitation anomalies of 1.8 °C and -267 mm, respectively.

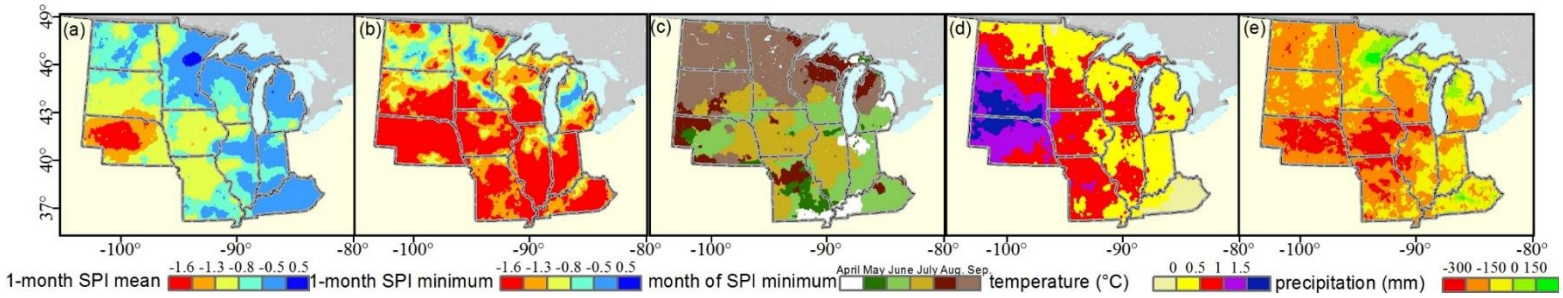
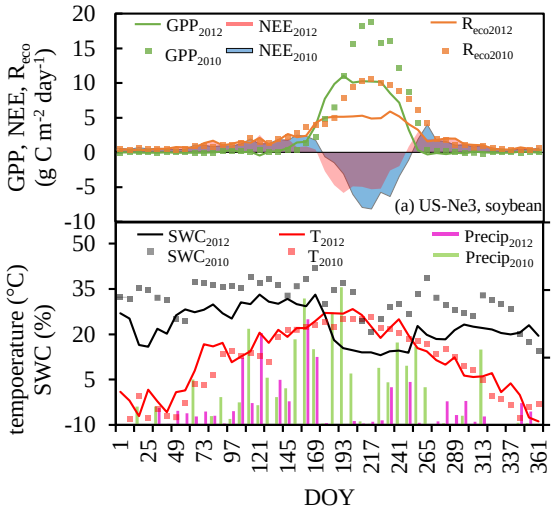


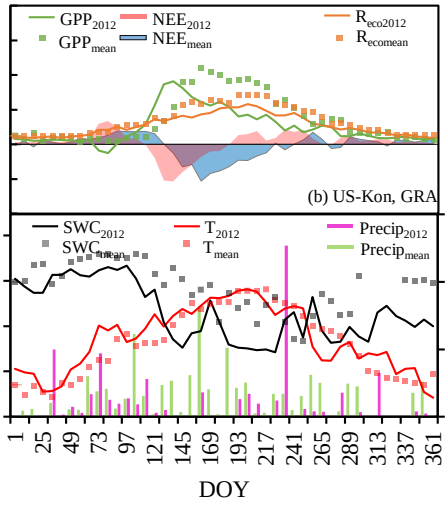
Figure 5.3 Spatial pattern of drought severity and climate anomalies during the 2012 growing season (May–September) over the U.S. Midwest. 1-month SPI mean and minimum (a and b, respectively), month of SPI minimum (c), anomalies of air temperature and total precipitation for the 2012 growing season relative to the mean values for 2010–2014 (d and e, respectively)

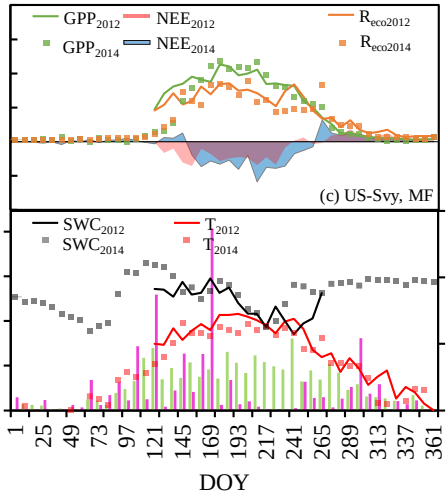
5.3.2 Impacts of droughts on the U.S. Midwest ecosystems at AmeriFlux sites

We compared climate conditions, soil moisture, vegetation growth (phenology), and CO_2 fluxes between 2012 and normal condition (2010–2014 mean) at AmeriFlux sites (Figure 5.4 and Table 5.1). Drought assessment of 2012 at AmeriFlux sites showed consistent results as mentioned above for the PRISM climate dataset. All AmeriFlux sites experienced warm temperature ($\Delta T > 0$) and water deficit (ΔP, $\Delta SWC < 0$) in the 2012 growing season. Particularly, SWC was significantly lower in 2012 compared to 2010–2014 means for soybean (-38 %) and grassland (-31 %) sites.

Four sites showed a uniform phenological response to 2012 extreme climate. SOS, MAXT, and EOS in 2012 were 1 or 2 weeks earlier compared to 2010–2014 means (Table 5.1). Soybean and grassland were significantly affected as GPP, NEE, and R_{eco} decreased significantly ($p < 0.001$, paired t test, $n = 10$) in parallel with soil water reduction in early July and June, respectively, and didn't recover afterwards (Figures 5.4a–b). The seasonal GPP was reduced by approximately 30% in soybean and grassland (-324 g C m^{-2} and -357 g C m^{-2}, respectively) relative to 2010–2014 means. In contrast, drought had less impact on carbon fluxes at forest sites. At US-Syv, a dry spell of 2012 in late August didn't cause the significant difference in ecosystem productivity compared to the 2010-2014 mean ($p = 0.31$, paired t test, $n = 10$) (Figure 5.4c), and seasonal GPP slightly increased (~75 g C m^{-2} above mean) in 2012 due to warmer spring. At US-MMS, GPP began to decrease from mid-June 2012, then recovered by mid-August (Figure 5.4d). The warmer spring with advanced SOS (~14 days earlier) and higher ecosystem productivity compensated the impact of summer drought on carbon uptake, resulting in only ~12 % decline in GPP at US-MMS.


GPP, NEE, R_eco (g C m-2 day-1)
GPP2012
NEE2012
Reco2012
GPP2010
NEE2010
Reco2010
(a) US-Ne3, soybean
tempoerature (°C)
SWC (%)
SWC2012
SWC2010
T2012
T2010
Precip2012
Precip2010
DOY


GPP2012
NEE2012
GPPmean
NEEmean
Reco2012
Recomean
(b) US-Kon, GRA
SWC2012
SWCmean
T2012
Tmean
Precip2012
Precipmean
DOY


GPP2012
NEE2012
GPP2014
NEE2014
Reco2012
Reco2014
(c) US-Svy, MF
SWC2012
SWC2014
T2012
T2014
DOY

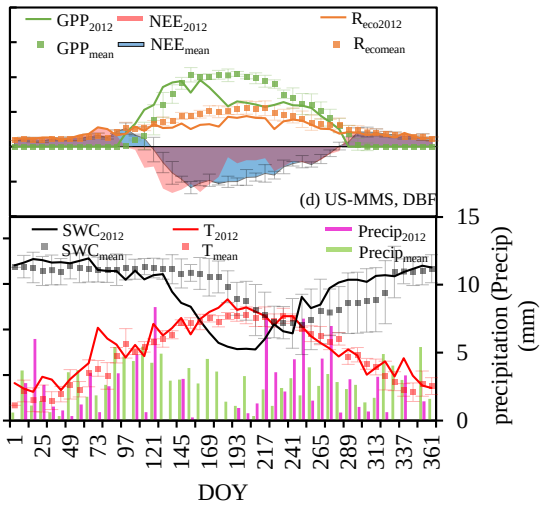


Figure 5.4 Observed climate, soil water content, and CO_2 fluxes at four AmeriFlux sites

Table 5.1 Changes in climate, soil moisture, vegetation phenology, and seasonal CO_2 fluxes between 2012 and 2010–2014 mean at four AmeriFlux sites during the growing season

Site Code	Name	Biome	Lat, Lon	Years	SOS		MAXT		EOS		Growing season					
					2012	mean	2012	mean	2012	mean	ΔT	ΔP	ΔSWC	ΔGPP	ΔNEE	ΔR_{eco}
US-Ne3	Mead Rainfed	CRO	41.18, -96.44	2010, 2012	06/02	06/10	07/12	07/28	09/06	09/14	1.5	-3.0	-11	-324	-21	-302
US-Kon	Konza Prairie	GRA	39.08, -96.56	2010-2012	04/07	04/15	05/17	06/10	11/01	11/17	0.5	-1.0	-9	-357	-141	-216
US-Syv	Sylvania Wilderness	MF	46.24, -89.35	2012, 2014	-	-	07/04	07//04	10/16	10/24	2.5	-1.0*	-4	75	-27	103
US-MMS	Morgan Monroe State Forest	DBF	39.32, -86.41	2010-2014	04/07	04/23	05/25	06/02	10/08	10/16	0.3	-0.5	-5	-169	25	-174

Lat-latitude; Lon-Longitude; SOS-start of season (leaf-on date when GPP ≥ 1 g C m^{-2} day^{-1}); MAXT-time of maximum photosynthesis; EOS-end of season (leaf-off date when GPP ≥ 1 g C m^{-2} day^{-1}); ΔT, ΔP, ΔSWC, ΔGPP, ΔNEE, ΔR_{eco} stand for the difference of temperature (°C day^{-1}), precipitation (mm day^{-1}), soil water content (% day^{-1}), total gross primary productivity, net ecosystem CO_2 exchange, and ecosystem respiration (g C m^{-2}) between 2012 and 2010–2014 mean during the growing season. *We used precipitation from US-PFa (78 km away) to replace the missing data at US-Syv in 2012.

5.3.3 Impacts of droughts on the U.S. Midwest ecosystems at regional scale

Figure 5.5 compares seasonal dynamics (8-day intervals) of four spatially averaged satellite-based vegetation biophysical parameters and GPP for different biomes between a drought year of 2012 and the mean for 2010-2014 (excluding 2012). For individual biome, we found good agreements among the responses (i.e., response timing and change in magnitudes) of NDVI, EVI, LSWI, SIF, and GPP_{VPM}, and SIF to 2012 drought. Shaded areas in Figure 5.5 show that all biomes experienced advanced phenology in 2012 and the largest reduction in NDVI, EVI, LSWI, SIF, and GPP_{VPM} occurred in August. Consistent with in-situ observations in section 3.2, agricultural biomes (maize, soybean, overall crop, and grassland) were more affected than forests. Maize emerged ~2 weeks (DOY = 137 when greenness and production started to increase) earlier than soybean (DOY = 153). However, lack of precipitation and extreme heat suppressed maize, soybean, and crop growth after July. Compared to a multi-year average, three vegetation indices, SIF, and GPP_{VPM} of pasture/grassland began to decrease around late-May (DOY = 145) with total reduction up to 24 % (NDVI), 22 % (EVI), 217 % (LSWI), 22 % (SIF), and 33 % (GPP_{VPM}). NDVI, EVI, LSWI, SIF, and GPP_{VPM} showed subtle decrease for both MF (-9 % to -2 %) and DBF (-8 % to -2 %) after July on biome scale, which were slightly different from in-situ observations.

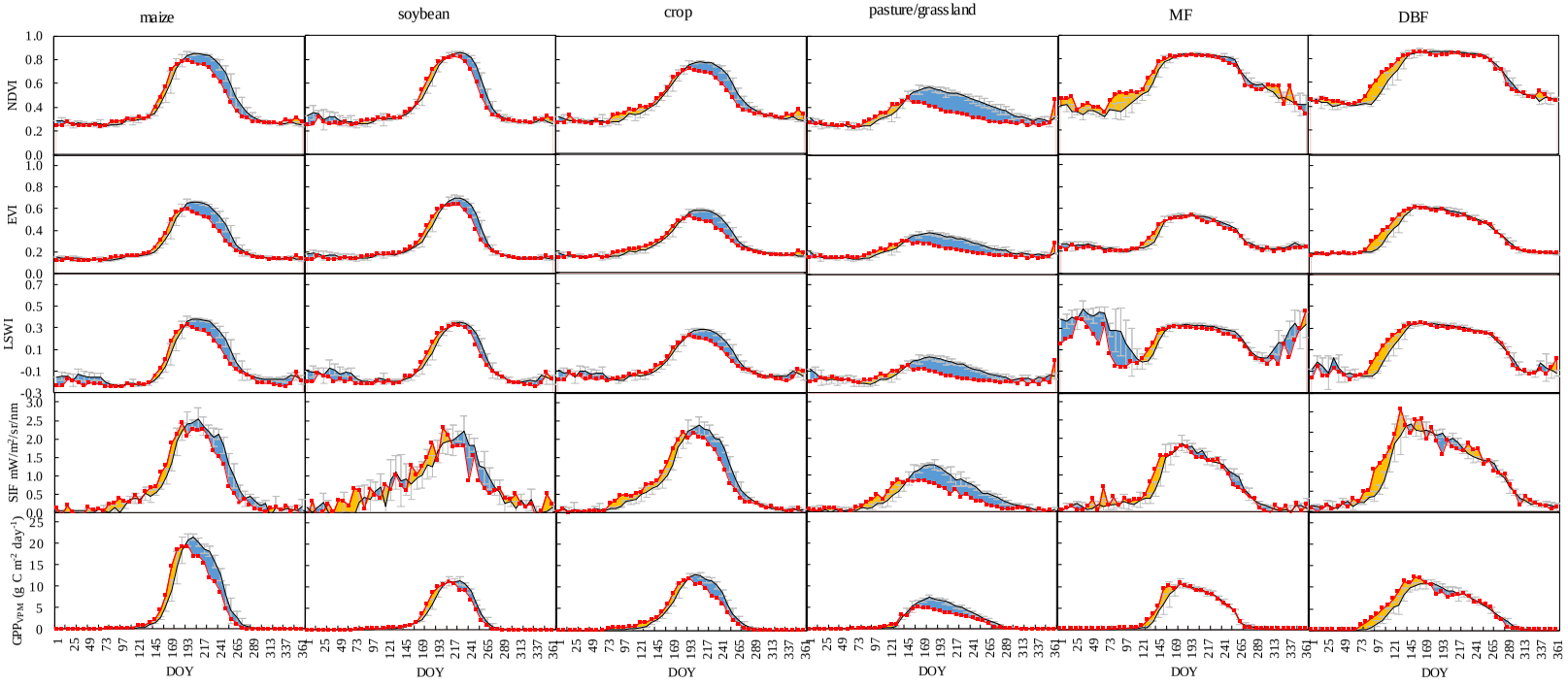


Figure 5.5 Comparison of seasonal dynamics of the spatially averaged MODIS 8-day vegetation indices (NDVI, EVI, and LSWI), SIF, and GPP_{VPM} for six different biomes between a drought year of 2012 and the mean for 2010-2014 (excluding 2012). DOY: day of year. Red lines with markers represent 2012; black lines represent the 2010–2014 mean (excluding 2012), and vertical bars represent mean ± standard deviation; and shaded areas represent 2012 anomalies relative to the mean values for 2010–2014

Figure 5.6 shows the Midwest-wide change in magnitudes of vegetation greenness and production during April – June (AMJ), July – September (JAS), and growing season (GS) of 2012, and vegetation response dates to 2012 drought on 500 m or 0.5 ° pixel level. In AMJ, vegetation greenness, SIF, and GPP_{VPM} over half of the U.S. Midwest apparently increased (RC > 0 %), whereas the mixed prairie region, including southwestern North Dakota, main South Dakota, and western Nebraska, experienced the largest reduction (Figure 5.6a). In JAS, the crop region was suppressed by drought as well as the west prairie. ~ 80 % of the U.S. Midwest showed decline in NDVI, EVI, LSWI, SIF, and GPP_{VPM} except the forest regions in the upper northern Great Lakes, southeast Missouri, and Kentucky, and parts of agriculture regions in the Minnesota River basin, and James and Red River basins of North Dakota (Figure 5.6b). Overall, the main agroecosystems of U.S. Midwest were the most drought-affected areas during the 2012 growing season, covering North Dakota, South Dakota, Nebraska, Iowa, Missouri, Illinois, and Indiana (Figure 5.6c). The reduction in vegetation greenness and productivity in these regions followed the drought pattern exhibited in Figure 5.3. For example, Nebraska was continuously under severe to extreme drought conditions during the 2012 growing season, and its agroecosystems experienced at least one-month extreme drought, mainly occurring in June or July (Figure 5.3b, c). Accordingly, the vegetation indices, SIF, and GPP_{VPM} of the Nebraska agroecosystems were significantly lower than the 2010 – 2014 mean.

Vegetation response timing to 2012 drought also spatially varied across the U.S. Midwest, and its spatial pattern was relatively consistent among five vegetation biophysical parameters (Figure 5.6). The prairie region responded the earliest, and

vegetation indices, SIF, and GPP_{VPM} started to drop below the multi-year averages in May and June. The major crop regions responded to drought mainly in August except northern Missouri (June and July). This finding agreed with USDA NASS Crop Progress Report when comparing Missouri with other states. The forests in upper Great Lakes and southeast Kentucky did not show clear reduction in vegetation indices, SIF, and GPP_{VPM} during the drought, whereas they decreased in July in deciduous forest regions in the southern Missouri and Indiana.

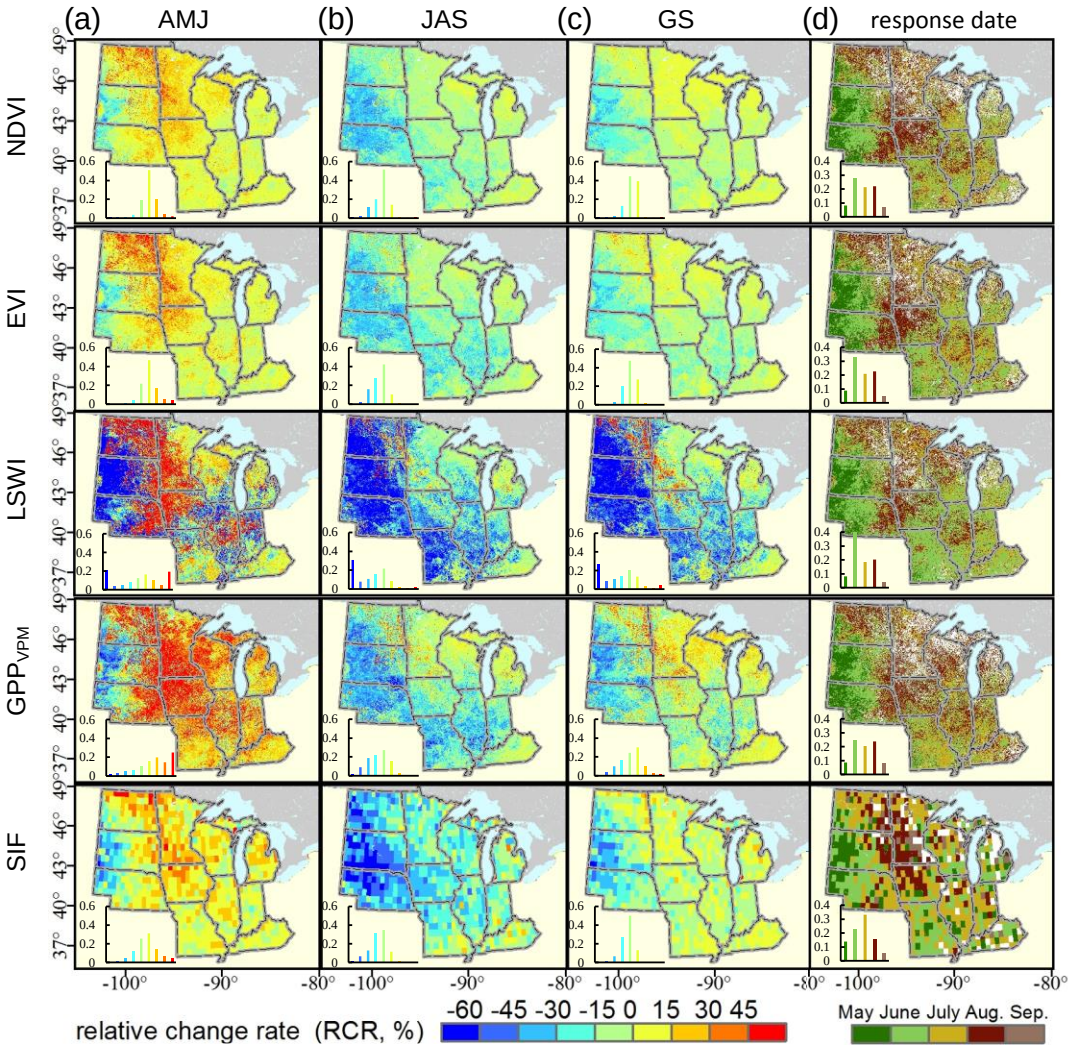


Figure 5.6 Midwest-wide relative change rate (RCR, %) and response date of 8-day MODIS vegetation indices (NDVI, EVI, LSWI) and productivity (GPP_{VPM} and SIF) during a drought year of 2012 relative to the mean for 2010–2014 (excluding 2012?).

RCR during April–June (AMJ, a), July–September (JAS, b), and growing season (GS, c). Response date to drought (d) - the first date when three 8-day composites in 2012 were continuously lower than the mean values for 2010–2014. The insets show the frequency histograms of RCR and response date

Total regional GPP_{VPM} in 2012 was the lowest (1.76 Pg C $year^{-1}$) compared to other years from 2010 to 2014 (Table 5.2), and drought reduced total GPP by 63 Tg C $year^{-1}$ (3.5%) in 2012 compared with the 2010–2014 mean GPP. Agroecosystems, which accounted for 84 % of regional GPP, were the most impacted by the 2012 drought. Maize, soybean, cropland, and grassland exhibited the lowest annual/total GPP in 2012 with reductions of 9%, 7%, 6%, and 29%, respectively, for annual GPP and 3%, 10%, 4%, and 28%, respectively, for total GPP. Grassland showed rapid recovery of carbon assimilation following drought, and annual GPP in 2013 for grassland was similar to annual GPP in 2010 (0.69 kg C m^{-2} $year^{-1}$). Annual GPP of maize, soybean, and crop gradually increased during 2013 – 2014, but it was still lower than in 2010. In contrast, annual/total GPP in 2012 for forests was higher than the 2010-2014 mean GPP. Surprisingly, annual GPP was lower in 2013 and 2014 than in 2012 for MF and DBF.

Table 5.2 Annual and total GPP estimates for each biome of the U.S. Midwest from 2010 to 2014

biome		2010	2011	2012	2013	2014	2012 AC	2012 RC
	area	232644	249535	263390	257493	243753		
maize	annual GPP	1.61	1.55	1.42	1.53	1.58	-0.15	-9
	total GPP	0.37	0.39	0.37	0.39	0.39	-11	-3
	area	192304	191286	188958	193132	214248		
soybean	annual GPP	0.91	0.88	0.83	0.87	0.90	-0.06	-7
	total GPP	0.17	0.17	0.16	0.17	0.19	-18	-10
maize and soybean	total GPP	0.55	0.55	0.53	0.56	0.58	-29	-5
	area	779765	769556	786575	769695	769696		
CRO	annual GPP	1.11	1.07	1.03	1.07	1.09	-0.06	-6
	total GPP	0.86	0.82	0.81	0.83	0.84	-31	-4

	area	265315	264856	275767	281087	281085		
GRA	annual GPP	0.69	0.68	0.49	0.69	0.70	-0.20	-29
	total GPP	0.18	0.18	0.14	0.19	0.20	-52	-28
	area	420092	418490	384771	403613	403613		
CRO/NVM	annual GPP	1.27	1.23	1.27	1.21	1.22	0.04	3
	total GPP	0.53	0.51	0.49	0.49	0.49	-18	-4
	area	127428	141064	143788	139160	139160		
MF	annual GPP	0.97	1.01	1.05	0.92	1.00	0.08	8
	total GPP	0.12	0.14	0.15	0.13	0.14	18	14
	area	112175	106294	113332	109645	109652		
DBF	annual GPP	1.44	1.41	1.53	1.39	1.37	0.13	9
	total GPP	0.03	0.03	0.04	0.03	0.03	4	13
all biomes	total GPP	1.87	1.81	1.76	1.79	1.82	-63	-4

area (km^2), area over 500 m pixels, for maize and soybean, pixels with area fraction over 20 %.

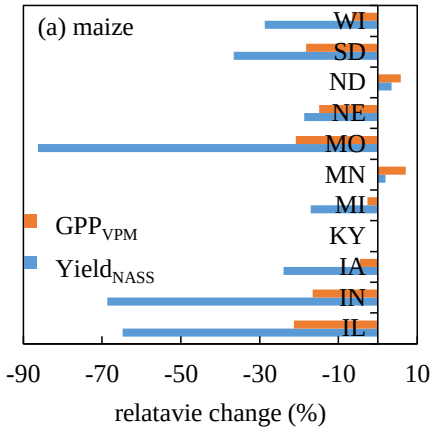
annual GPP (kg C m^{-2} $year^{-1}$), spatially averaged annual GPP

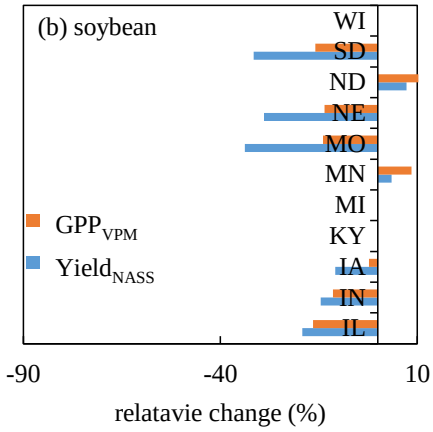
total GPP (Pg C $year^{-1}$), spatially integrate annual GPP

2012 AC (Tg C $year^{-1}$), actual change of total GPP in 2012 relative to the other-year mean of 2010–2014

2012 RC (%), relative change rate of total GPP in 2012 relative to the other-year mean of 2010–2014.

Agricultural harvest data in 2012 also show the impact of drought on agroecosystem productivity and carbon cycles. Agricultural harvest data showed negative anomalies of $Yield_{NASS}$ for maize and soybean in 2012 over most Midwest states except North Dakota (ND) and Minnesota (MN), consistent with the patterns of GPP_{VPM} (Figures 5.7a-b, Figure 5.6c). $Yield_{NASS}$ and GPP_{VPM} for pasture/grassland declined over three main growing states (Figure 5.7c).





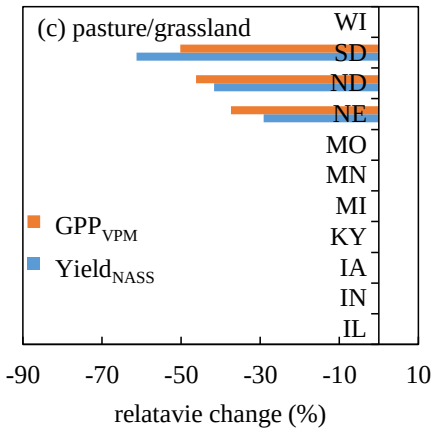


Figure 5.7 Relative change (%) of GPP_{VPM} and NASS yield statistics ($Yield_{NASS}$) over Midwest states for maize (a), soybean (b), and pasture/grassland (c). To avoid statistic errors in regions with sparse agriculture cultivation, analyses are limited to

states where maize, soybean, or pasture/grassland account for > 20% of the total state area

5.4 Discussion

5.4.1 The 2012 flash drought in the U.S. Midwest

The 2012 flash drought in the U.S. Midwest was one of the worst on record with comparable severity and spatial extent of those in 1930s, 1950s, and 1980s (Hoerling et al. 2014; Kellner and Niyogi 2014). It was characterized by both moisture deficit and abnormally high temperature, moreover, it wasn't captured by the U.S. Drought Monitor (USDM) until late June due to its rapid onset in May. Mallya et al. (2013) concluded that the weak winter storms in previous winter triggered by anomalous tropical sea surface temperatures (SSTs), La Niña, was the main cause of the 2012 flash drought. Two recent studies, however, showed that the 2012 drought more likely related to natural weather variations causing the reduction of cyclone and frontal activity in late spring, and the decrease of moisture transportation from Gulf of Mexico instead of SST anomalies (Hoerling et al. 2014; Kumar et al. 2013). The probability of severe droughts and heat waves are predicted to increase over the continental United States in future according to multimodel projections (Basara et al. 2013; Cook et al. 2015; Wehner et al. 2011; Wuebbles et al. 2014). Hence, the drought extremes will continue to significantly affect the terrestrial ecosystems in future by altering productivity and ecosystems' responses to drought. For example, a previous data-driven diagnostics showed that drought was a major factor contributing to the interannual variability in carbon fluxes over North America during 2000 to 2010 (Xiao et al. 2014b).

5.4.2 Impacts of 2012 flash drought on the U.S. Midwest ecosystems

This study, using multiple sources of evidences, showed that the 2012 flash drought significantly affected ecosystems in the U.S. Midwest by changing vegetation function, structure, and phenology. Similar to slowly-developed or prolonged drought, flash drought causes direct effects on ecosystem function by modifying carbon assimilation (GPP) and release. Higher temperature and vapor pressure deficit (VPD), and water-limited conditions during droughts lead to stomatal closure, membrane damage, and disturbing activities of photosynthetic enzymes, and subsequently reduce carbon uptake by the ecosystems (Farooq et al. 2009; Reddy et al. 2004; Wagle and Kakani 2014). In addition, drought can trigger changes in vegetation structure, such as the decrease of green leaf area due to leaf angle change within canopy and leaf senescence, and shorten growing season length, and thus indirectly causing further decline in carbon assimilation (van der Molen et al. 2011). During the 2012 drought, in-situ observations, vegetation indices, and ecosystem modeling results showed the relative consistency in changing trends of vegetation phenology, greenness, and productivity across stand, biome, and regional levels. In spring, warm weather and close-to-normal precipitation triggered the growth of natural vegetation and encouraged farmers' planting activities resulting to the earlier shifting of planting and emergence dates for agricultural crops. In summer, on the other hand, high temperature and VPD, and soil water deficits inhibited plant photosynthesis and caused early senescence of vegetation, leading to lower productivity. Even though the warm spring with higher vegetation greenness and productivity offset the impact of summer drought in 2012, the summer drought caused

significant negative effects in vegetation greenness and productivity for both summer and the entire year in the U.S. Midwest.

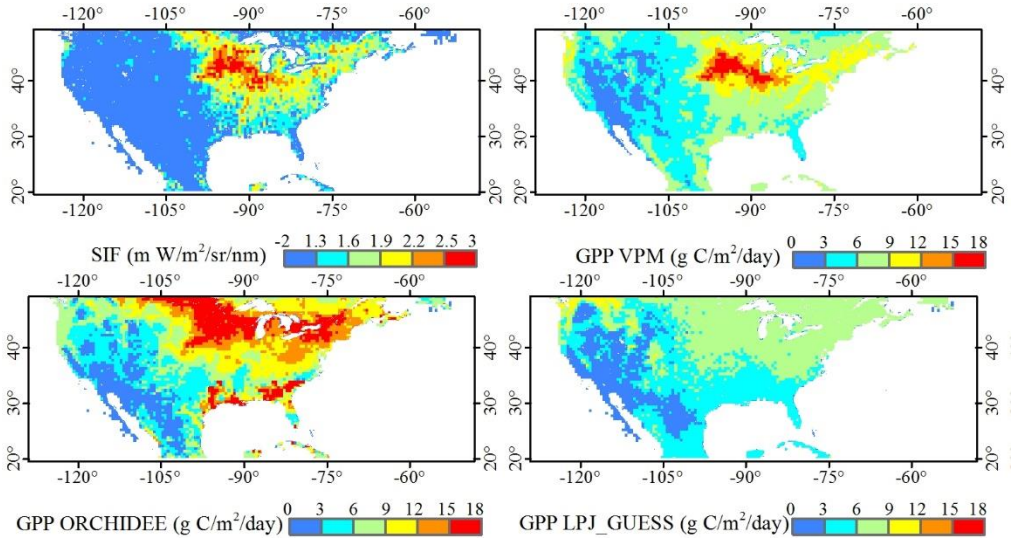
The vegetation greenness and productivity reacted differently to the 2012 flash drought depending on ecosystem and land cover types. Grassland and prairie regions rapidly responded as soon as drought started to develop (May), and exhibited the largest declines in greenness and productivity. For agricultural crops, even short periods of intense water stress can cause productivity reduction and yield loss if the stress happen during sensitive stage of crop development. Studies have reported soil water stress, happening at particular stages (i.g. sixth leaf stage, silking, blister, or dough stages), can reduce maize grain yield by up to 40 % - 80% (Cakir 2004; Calvino et al. 2003; Earl and Davis 2003; Hunt et al. 2014). In 2012 summertime, the simultaneous occurrences of soil water depletion and heat wave turned into stresses to crop growth from July in the U.S. Midwest, and their impacts on plant growth was more significant than the impact when stresses happens individually. Significant negative effects of drought were not found in forest ecosystems. One reason is that deep rooting system of forest ecosystems could relieve drought stress, and other factors, such as drought severity, timing of drought, drought-associated higher incident radiation, and dominant species, should also be accounted (Shi et al. 2014; Zeng et al. 2008). For example, forest ecosystems only experienced abnormal or moderate dry conditions in 2012.

5.4.3 Challenges in terrestrial ecosystem models for agroecosystems

Numerous studies have estimated ecosystem productivity at large scales and projected its changes in response to climate change and climate variability using either semi-empirical diagnostic models or process-based biogeochemistry models (Ciais et al.

2005; Reichstein et al. 2007; Sitch et al. 2008; Zhao and Running 2010). However, a large range of uncertainties related to cropland in these models were often ignored (Schwalm et al. 2010; van der Molen et al. 2011; Xiao et al. 2014a). One main reason is that these models fail to take into account specific crop growth modules, such as C4 crops. For example, it has been widely verified that MODIS standard GPP product (MOD17) assigns a universal ε_0 (1.04 gC MJ^{-1}) for all crop species under different photosynthetic pathway (C_3 and C_4) resulting to largely underestimate GPP for C_4 crops (Wagle et al. 2014; Xiao et al. 2014a; Xin et al. 2015; Zhang et al. 2008b). An intercomparison of 26 terrestrial ecosystem models in part by the North American Carbon Project (NACP) found that all models performed the worst when modeling GPP for crop and grassland (Schaefer et al. 2012). Recently, Guanter et al. (2014) inferred that the crop GPP derived from GOME-2 SIF datasets were 50 – 75% higher than GPP estimates from state-of-art carbon models over US Corn Belt, including ten process-based DGVMs (Dynamic Global Vegetation Models), MPI-BGC (Max Planck Institute for Biogeochemistry) model, and MOD17. To simulate regional GPP, this study used fine-resolution (30 m or 56 m) crop-specific land use maps from the NASS CDL for each calendar year to improve the parameterization of ε_0 in the VPM model for maize (C_4) and soybean (C_3), and took account for the sub-pixel variability for C_3 and C_4 photosynthetic pathways within individual 500 m pixel. The results indicated not only the great potential of VPM to reproduce the observed eddy-covariance GPP for maize, soybean, MF, DBF at site levels (Figure S5.1), but also the consistency of regional GPP estimates with GOME-2 SIF dataset on biome- and 0.5° grid- levels in 2010 - 2012 (see supplementary Figures. S5.2–S5.3). We further compared GPP estimates from three diagnostic models (VPM, MOD17, and MPI-BGC), four

DGVMs as part of the Trendy project ("Trends in net land-atmosphere carbon exchange over the period 1980−2010") with SIF measurement in July 2010 over the US (Figure 5.8). SIF measurement showed that the US Corn Belt, the intensively cultivated and highly productive region, had extremely high SIF signals in July, similar to the global analyses of Zeng et al. (2014) and (Guanter et al. 2014). Only the VPM and VEGAS captured this SIF pattern over the US Corn Belt, but not by other five models. In addition, the magnitudes of GPP derived from VPM in the primary maize production area was closer to the tower-derived GPP (12 – 18 g C m^{-2} day^{-1}) than the VEGAS GPP estimates (9 – 12 g C m^{-2} day^{-1}). Hence, results of this study illustrate that the incorporation of crop-specified module or parameterization can help improve the terrestrial ecosystem models for more accurate projections of agricultural productivity and the impacts of climate change on agroecosystems.



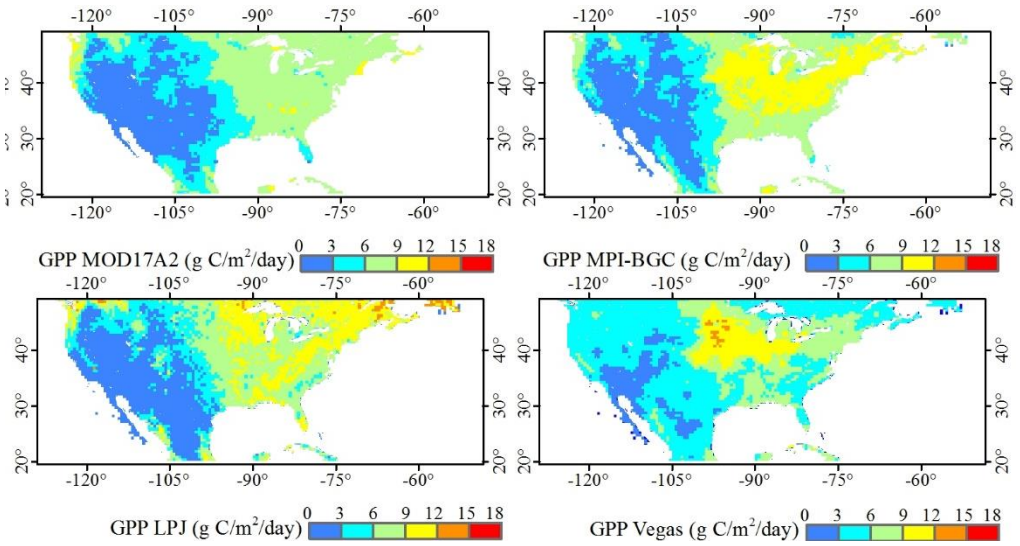


Figure 5.8 Comparison of GOME-2 SIF and GPP estimates from three diagnostic models (VPM, MOD17, and MPI-BGC), and four process-based DGVMs (ORCHIDEE, JPL_GUESS, JPL, and VEGAS - as part of TRENDY project, http://dgvm.ceh.ac.uk/node/21) in July 2010

5.5 Conclusion

The 2012 flash drought in the U.S. Midwest, characterized by high temperature, large cumulative rainfall deficit, and rapid depletion of soil moisture, was the most severe summer drought over the past hundred years. This study used an integrated spatial remote sensing observations, and scaled ecosystem modelling approaches, and demonstrated that the large-scale meteorological anomalous patterns in the 2012 growing season significantly affected the U.S. Midwest ecosystems, in particular agroecosystems. These extreme drought events in future will likely offset the enhancement effects of increased atmospheric CO_2 concentration, extended growing season length due to global warming, cultivar improvements, and higher sowing density on regional agriculture productivity. This study only investigated the direct and concurrent impacts of flash drought on ecosystems (i.e. phenology, vegetation greenness, and photosynthesis). Ecosystem responses, however, can exceed the duration of climate extremes through the time-lagged

effects, especially forest ecosystems. Thus, the underlying mechanisms of long-term consequences of flash droughts on ecophysiology and ecosystem dynamics, such as reduced plant growth and increase mortality, the changes in species competition, and the pest and pathogen outbreaks in the years following flash droughts, should be better understood in future studies.

Supplementary materials

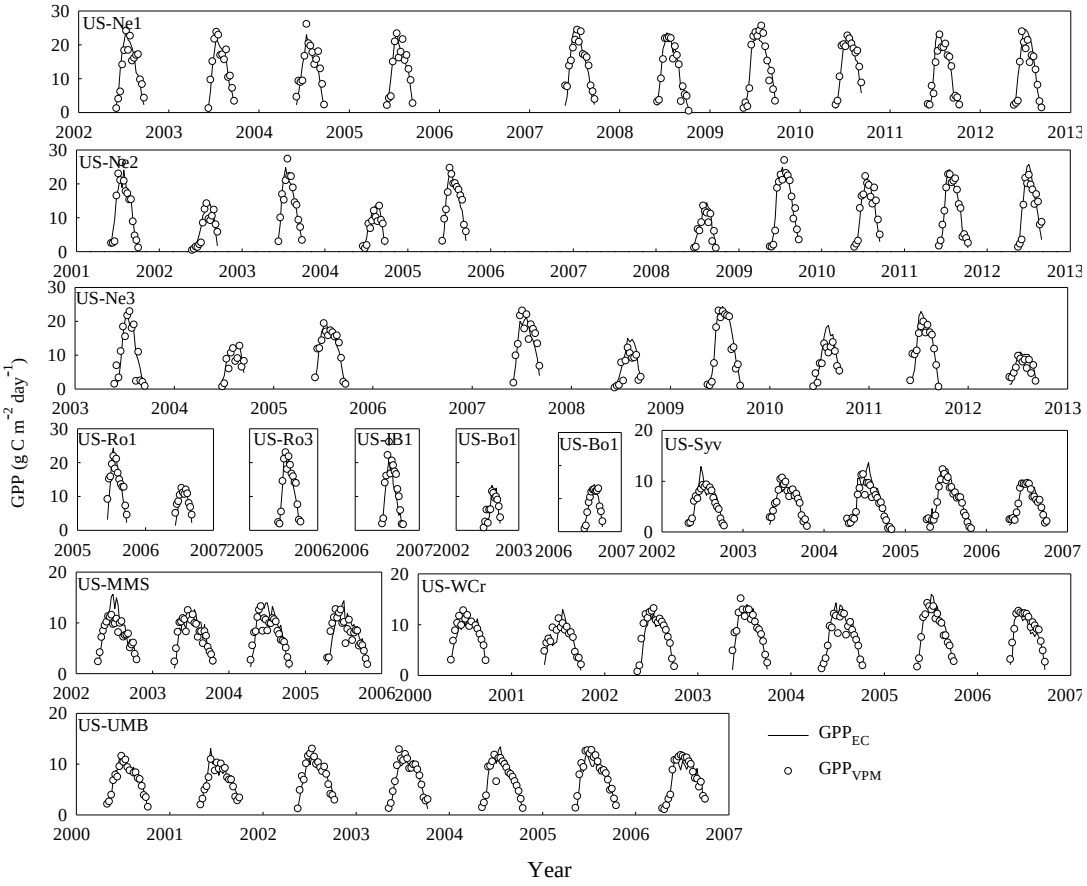
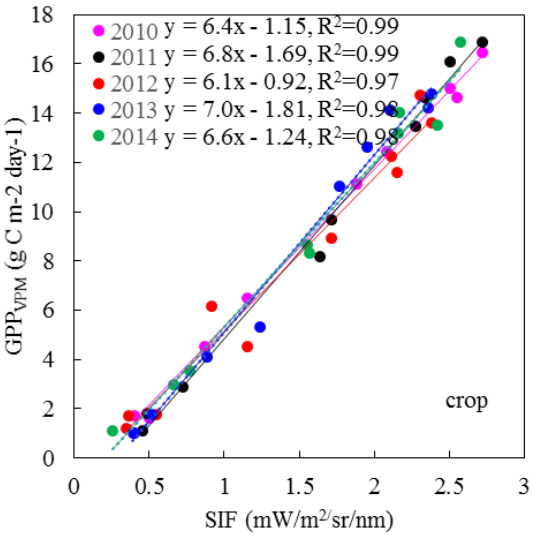
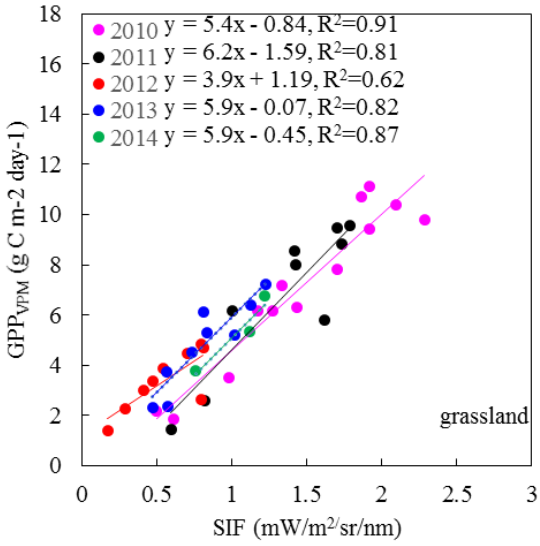


Figure S5.1 Seasonal dynamics of 8-day GPP at the AmeriFlux sites in the U.S. Midwest. US-Ne1, US-Ne2, US-Ne3, US-Ro1, US-Ro3, US-IB1, and US-Bo1 are CRO sites for maize and soybean (soybean was highlighted in grey); US-Syv is MF site; US-MMS, US-WCr, and US-UMB are DBF sites. GPP_{EC} - estimated GPP from in-situ eddy tower data; GPP_{VPM} - simulated GPP from the VPM


2010 y = 6.4x - 1.15, R2=0.99
2011 y = 6.8x - 1.69, R2=0.99
2012 y = 6.1x - 0.92, R2=0.97
2013 y = 7.0x - 1.81, R2=0.98
2014 y = 6.6x - 1.24, R2=0.98
crop
GPPVPM (g C m-2 day-1)
SIF (mW/m2/sr/nm)


2010 y = 5.4x - 0.84, R2=0.91
2011 y = 6.2x - 1.59, R2=0.81
2012 y = 3.9x + 1.19, R2=0.62
2013 y = 5.9x - 0.07, R2=0.82
2014 y = 5.9x - 0.45, R2=0.87
grassland
GPPVPM (g C m-2 day-1)
SIF (mW/m2/sr/nm)

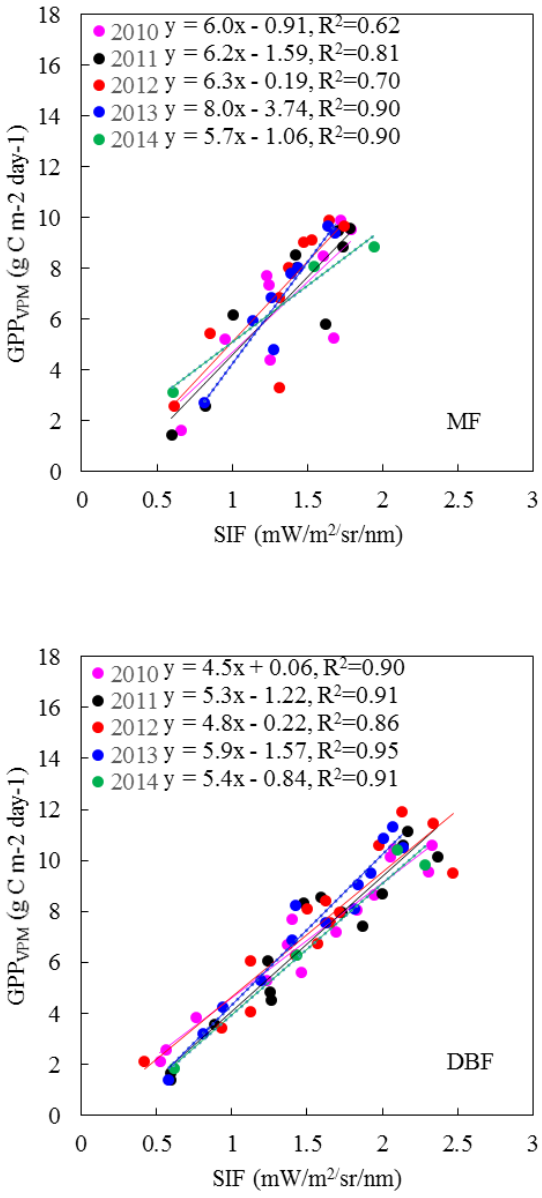


Figure S5.2 Scatter plot of biweekly SIF vs. GPP_{VPM} averaged for each biomes during 2010 – 2014

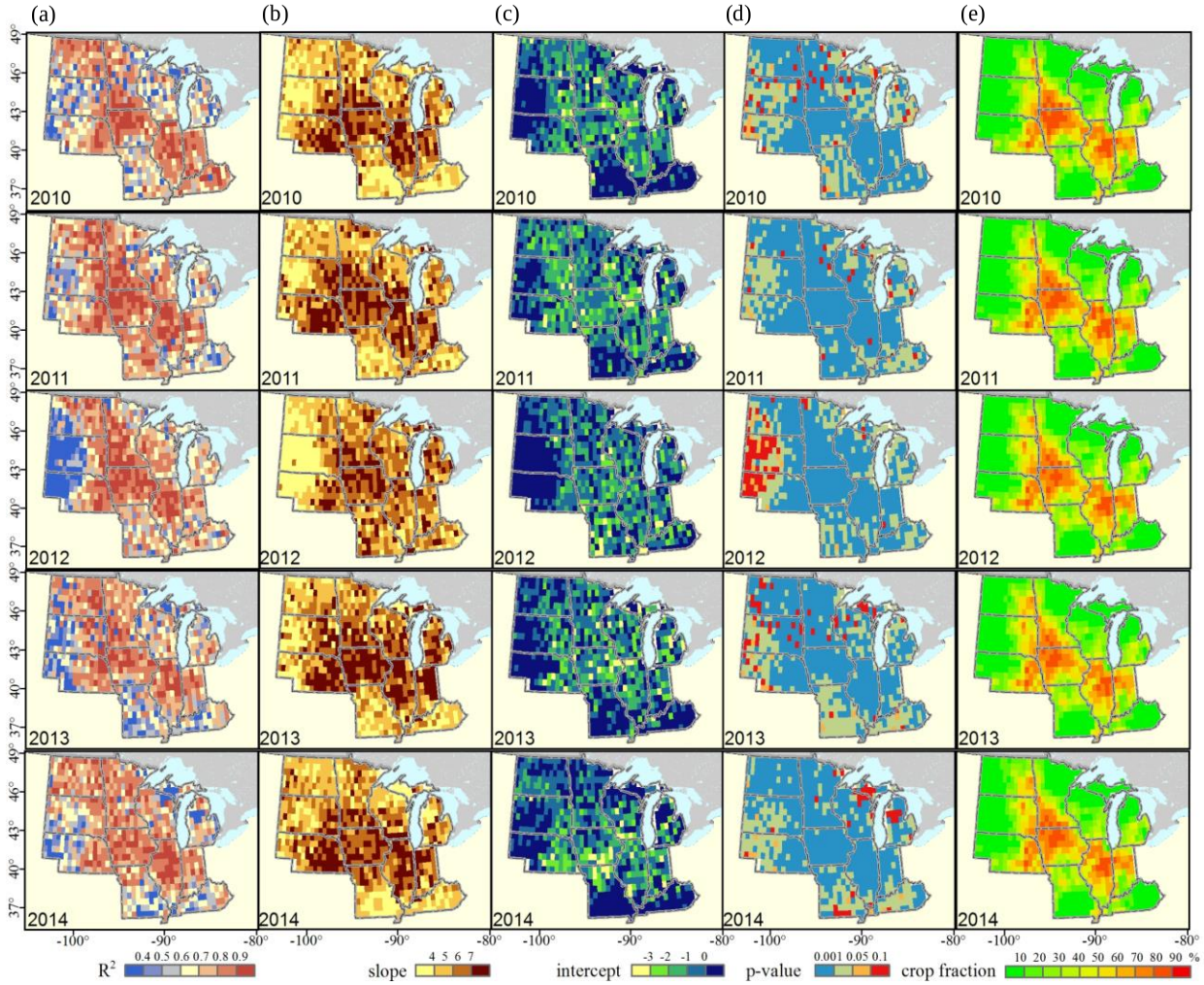


Figure S5.3 Spatial distribution of linear regression (R^2, slope, and intercept) between SIF and GPP_{VPM} and crop area fraction on 0.5 grid cell during 2010 – 2014

Chapter 6: Conclusions and perspectives

Remote sensing has been a useful tool of mapping land use and land cover change and simulating seasonal dynamics and interannual variations of primary productivity over agricultural regions. My dissertation selected three case studies, which related to three largest commodity crops (paddy rice, maize, soybean) and two dominant savanna woodlands across the typical agroecosystems of Northern Asia, Southern Africa, and Northern America, to highlight the potentials and strengthen the capacities of remote sensing to produce the high-quality products of crop type maps and primary productivity over large regions.

Chapter 2 demonstrated the potentials of 30 m multi-temporal Landsat imagery in regional-scale rice classification by integrating the phenological and spectral features of paddy rice in the flooding/transplanting and ripening phases. Future studies should investigate several factors such as non-cropland inundated land types, terrain conditions, and image availability when applying this methodology to rice field identification in other regions, particularly in Southeast Asia with its complex rice cultivation ecosystems. In addition to paddy rice, to acquire high-accuracy and high-spatial resolution LULCC maps for other main crops over large regions should also be explored in future.

The VPM has been proved to robust and reliable estimates of GPP across several biomes and geographic regions. Chapter 3 is the first study to evaluate the potential of the VPM to estimate the GPP in savanna woodland ecosystems. The results showed that the VPM well simulated the seasonal dynamics and interannual variation of GPP at two in-situ sites. However, savanna is a complex ecosystem, further evaluation of the VPM

for other savanna vegetation types is necessary before its application on savanna ecosystems at regional scales.

Chapter 4 emphasized the impacts of the accuracy of regional climate inputs on the PEM-based GPP simulation. The results showed that the NARR air temperature was accurate. The NARR radiation, however, was positively biased, and led to the overestimates of GPP by the VPM. It implies that the capability of the satellite-based PEMs for regional productivity monitoring would be enhanced if the radiation of the regional reanalysis product can be improved. Future research is required to address the uncertainties of the PEM-based GPP estimates caused by other model inputs such as satellite data.

Chapter 5 first demonstrated that the VPM was capable to accurately simulate seasonal dynamics, spatial variation, and interannual variation of GPP over the U.S. Midwest. With an integrated spatial remote sensing observations, and scaled ecosystem modelling approaches, this study then demonstrated that the large-scale meteorological anomalous patterns during 2012 flash drought significantly affected the U.S. Midwest ecosystems, in particular agroecosystems. Future studies should better understand the underlying mechanisms of long-term consequences of flash droughts on ecophysiology and ecosystem dynamics in the years following flash droughts.

References

Abatzoglou, J.T. (2013). Development of gridded surface meteorological data for ecological applications and modelling. *International Journal of Climatology, 33*, 121-131

Alberte, B., Pascalle C, S., SÖNke, Z., Sibyll, S., Wolfgang, L., Wolfgang, C., Dieter, G., Hermann, L.-C., Christoph, M., Markus, R., & Benjamin, S. (2007). Modelling the role of agriculture for the 20th century global terrestrial carbon balance. *Global Change Biology, 13*

Alcantara, C., Kuemmerle, T., Prishchepov, A.V., & Radeloff, V.C. (2012). Mapping abandoned agriculture with multi-temporal MODIS satellite data. *Remote Sensing of Environment, 124*, 334-347

Allen, C.D., Macalady, A.K., Chenchouni, H., Bachelet, D., McDowell, N., Vennetier, M., Kitzberger, T., Rigling, A., Breshears, D.D., Hogg, E.H., Gonzalez, P., Fensham, R., Zhang, Z., Castro, J., Demidova, N., Lim, J.H., Allard, G., Running, S.W., Semerci, A., & Cobb, N. (2010). A global overview of drought and heat-induced tree mortality reveals emerging climate change risks for forests. *Forest Ecology and Management, 259*, 660-684

Archibald, S., & Scholes, R.J. (2007). Leaf green-up in a semi-arid African savanna - separating tree and grass responses to environmental cues. *Journal of Vegetation Science, 18*, 583-594

Archibald, S.A., Kirton, A., van der Merwe, M.R., Scholes, R.J., Williams, C.A., & Hanan, N. (2009). Drivers of inter-annual variability in Net Ecosystem Exchange in a semi-arid savanna ecosystem, South Africa. *Biogeosciences, 6*, 251-266

Arneth, A., Veenendaal, E.M., Best, C., Timmermans, W., Kolle, O., Montagnani, L., & Shibistova, O. (2006). Water use strategies and ecosystem-atmosphere exchange of CO_2 in two highly seasonal environments. *Biogeosciences, 3*, 421-437

Asner, G.P., & Alencar, A. (2010). Drought impacts on the Amazon forest: the remote sensing perspective. *New Phytologist, 187*, 569-578

Babst, F., Mueller, R.W., & Hollmarm, R. (2008). Verification of NCEP reanalysis shortwave radiation with mesoscale remote sensing data. *Ieee Geoscience and Remote Sensing Letters, 5*, 34-37

Baldocchi, D., Falge, E., Gu, L.H., Olson, R., Hollinger, D., Running, S., Anthoni, P., Bernhofer, C., Davis, K., Evans, R., Fuentes, J., Goldstein, A., Katul, G., Law, B., Lee, X.H., Malhi, Y., Meyers, T., Munger, W., Oechel, W., U, K.T.P., Pilegaard, K., Schmid, H.P., Valentini, R., Verma, S., Vesala, T., Wilson, K., & Wofsy, S. (2001). FLUXNET: A new tool to study the temporal and spatial variability of ecosystem-scale carbon dioxide, water vapor, and energy flux densities. *Bulletin of the American Meteorological Society, 82*, 2415-2434

Baldocchi, D., Sturtevant, C., & Contributors, F. (2015). Does day and night sampling reduce spurious correlation between canopy photosynthesis and ecosystem respiration? *Agricultural and Forest Meteorology, 207*, 117-126

Bartholome, E., & Belward, A.S. (2005). GLC2000: a new approach to global land cover mapping from Earth observation data. *International Journal of Remote Sensing, 26*, 1959-1977

Basara, J.B., Maybourn, J.N., Peirano, C.M., Tate, J.E., Brown, P.J., Hoey, J.D., & Smith, B.R. (2013). Drought and associated impacts in the Great Plains of the United States—A review. *International Journal of Geosciences, 4*, 72

Batista, G.T., Shimabukuro, Y.E., & Lawrence, W.T. (1997). The long-term monitoring of vegetation cover in the Amazonian region of northern Brazil using NOAA-AVHRR data. *International Journal of Remote Sensing, 18*, 3195-3210

Beer, C., Reichstein, M., Tomelleri, E., Ciais, P., Jung, M., Carvalhais, N., Rodenbeck, C., Arain, M.A., Baldocchi, D., Bonan, G.B., Bondeau, A., Cescatti, A., Lasslop, G., Lindroth, A., Lomas, M., Luyssaert, S., Margolis, H., Oleson, K.W., Roupsard, O., Veenendaal, E., Viovy, N., Williams, C., Woodward, F.I., & Papale, D. (2010). Terrestrial gross carbon dioxide uptake: global distribution and covariation with climate. *Science, 329*, 834-838

Belder, P., Bouman, B.A.M., Cabangon, R., Lu, G., Quilang, E.J.P., Li, Y.H., Spiertz, J.H.J., & Tuong, T.P. (2004). Effect of water-saving irrigation on rice yield and water use in typical lowland conditions in Asia. *Agricultural Water Management, 65*, 193-210

Bigler, C., Gavin, D.G., Gunning, C., & Veblen, T.T. (2007). Drought induces lagged tree mortality in a subalpine forest in the Rocky Mountains. *Oikos, 116*, 1983-1994

Biradar, C.M., & Xiao, X.M. (2011). Quantifying the area and spatial distribution of double- and triple-cropping croplands in India with multi-temporal MODIS imagery in 2005. *International Journal of Remote Sensing, 32*, 367-386

Boryan, C., Yang, Z.W., Mueller, R., & Craig, M. (2011). Monitoring US agriculture: the US Department of Agriculture, National Agricultural Statistics Service, Cropland Data Layer Program. *Geocarto International, 26*, 341-358

Boyer, J.S., Byrne, P., Cassman, K.G., Cooper, M., Delmer, D., Greene, T., Gruis, F., Habben, J., Hausmann, N., Kenny, N., Lafitte, R., Paszkiewicz, S., Porter, D., Schlegel, A., Schussler, J., Setter, T., Shanahan, J., Sharp, R.E., Vyn, T.J., Warner, D., & Gaffney, J. (2013). The U.S. drought of 2012 in perspective: A call to action. *Global Food Security*, *2*, 139-143

Bradley, A.V., Gerard, F.F., Barbier, N., Weedon, G.P., Anderson, L.O., Huntingford, C., Aragao, L.E.O.C., Zelazowski, P., & Arai, E. (2011). Relationships between phenology, radiation and precipitation in the Amazon region. *Global Change Biology*, *17*, 2245-2260

Bradley, B.A., Jacob, R.W., Hermance, J.F., & Mustard, J.F. (2007). A curve fitting procedure to derive inter-annual phenologies from time series of noisy satellite NDVI data. *Remote Sensing of Environment, 106*, 137-145

Breshears, D.D., Cobb, N.S., Rich, P.M., Price, K.P., Allen, C.D., Balice, R.G., Romme, W.H., Kastens, J.H., Floyd, M.L., Belnap, J., Anderson, J.J., Myers, O.B., & Meyer, C.W. (2005). Regional vegetation die-off in response to global-change-type drought. *Proceedings of the National Academy of Sciences of the United States of America, 102*, 15144-15148

Brown, M.E., de Beurs, K.M., & Marshall, M. (2012). Global phenological response to climate change in crop areas using satellite remote sensing of vegetation, humidity and temperature over 26 years. *Remote Sensing of Environment, 126*, 174-183

Bush, B.C., Valero, F.P.J., Simpson, A.S., & Bignone, L. (2000). Characterization of thermal effects in pyranometers: A data correction algorithm for improved measurement of surface insolation. *Journal of Atmospheric and Oceanic Technology*, *17*, 165-175

Cai, H.Y., Zhang, S.W., Bu, K., Yang, J.C., & Chang, L.P. (2011). Integrating geographical data and phenological characteristics derived from MODIS data for improving land cover mapping. *Journal of Geographical Sciences, 21*, 705-718

Cai, W.W., Yuan, W.P., Liang, S.L., Zhang, X.T., Dong, W.J., Xia, J.Z., Fu, Y., Chen, Y., Liu, D., & Zhang, Q. (2014). Improved estimations of gross primary production using satellite-derived photosynthetically active radiation. *Journal of Geophysical Research-Biogeosciences, 119*, 110-123

Cakir, R. (2004). Effect of water stress at different development stages on vegetative and reproductive growth of corn. *Field Crops Research, 89*, 1-16

Calvino, P.A., Andrade, F.H., & Sadras, V.O. (2003). Maize yield as affected by water availability, soil depth, and crop management. *Agronomy Journal, 95*, 275-281

Caylor, K.K., & Shugart, H.H. (2004). Simulated productivity of heterogeneous patches in Southern African savanna landscapes using a canopy productivity model. *Landscape Ecology, 19*, 401-415

Chandrasekar, K., Sesha Sai, M.V.R., Roy, P.S., & Dwevedi, R.S. (2010). Land Surface Water Index (LSWI) response to rainfall and NDVI using the MODIS Vegetation Index product. *International Journal of Remote Sensing, 31*, 3987-4005

Chen, J.M., Liu, J., Cihlar, J., & Goulden, M.L. (1999). Daily canopy photosynthesis model through temporal and spatial scaling for remote sensing applications. *Ecological Modelling, 124*, 99-119

Chen, T., van der Werf, G.R., Gobron, N., Moors, E.J., & Dolman, A.J. (2014). Global cropland monthly gross primary production in the year 2000. *Biogeosciences, 11*, 3871-3880

Chen, T.X., van der Werf, G.R., Dolman, A.J., & Groenendijk, M. (2011). Evaluation of cropland maximum light use efficiency using eddy flux measurements in North America and Europe. *Geophysical Research Letters, 38*

Chidumayo, E.N. (2001). Climate and phenology of savanna vegetation in southern Africa. *Journal of Vegetation Science, 12*, 347-354

Ciais, P., Bombelli, A., Williams, M., Piao, S.L., Chave, J., Ryan, C.M., Henry, M., Brender, P., & Valentini, R. (2011). The carbon balance of Africa: synthesis of recent research studies. *Philosophical Transactions of the Royal Society a-Mathematical Physical and Engineering Sciences, 369*, 2038-2057

Ciais, P., Reichstein, M., Viovy, N., Granier, A., Ogee, J., Allard, V., Aubinet, M., Buchmann, N., Bernhofer, C., Carrara, A., Chevallier, F., De Noblet, N., Friend, A.D., Friedlingstein, P., Grunwald, T., Heinesch, B., Keronen, P., Knohl, A., Krinner, G., Loustau, D., Manca, G., Matteucci, G., Miglietta, F., Ourcival, J.M., Papale, D., Pilegaard, K., Rambal, S., Seufert, G., Soussana, J.F., Sanz, M.J., Schulze, E.D., Vesala,

T., & Valentini, R. (2005). Europe-wide reduction in primary productivity caused by the heat and drought in 2003. *Nature, 437*, 529-533

Ciais, P., Wattenbach, M., Vuichard, N., Smith, P., Piao, S.L., Don, A., Luyssaert, S., Janssens, I.A., Bondeau, A., Dechow, R., Leip, A., Smith, P.C., Beer, C., van der Werf, G.R., Gervois, S., Van Oost, K., Tomelleri, E., Freibauer, A., Schulze, E.D., & Team, C.S. (2010). The European carbon balance. Part 2: croplands. *Global Change Biology, 16*, 1409-1428

Cohen, W.B., Yang, Z.G., & Kennedy, R. (2010). Detecting trends in forest disturbance and recovery using yearly Landsat time series: 2. TimeSync - Tools for calibration and validation. *Remote Sensing of Environment, 114*, 2911-2924

Cook, B.I., Ault, T.R., & Smerdon, J.E. (2015). Unprecedented 21st century drought risk in the American Southwest and Central Plains. *Science Advances, 1*

Coops, N. (1999). Improvement in predicting stand growth of Pinus radiata (D. Don) across landscapes using NOAA AVHRR and Landsat MSS imagery combined with a forest growth process model (3-PGS). *Photogrammetric Engineering and Remote Sensing, 65*, 1149-1156

Couto, A.F., de Carvalho, O.A., Martins, E.D., Santana, O.A., de Souza, V.V., & Encinas, J.I. (2011). Denoising and caracterization of cerrado physiognomies using MODIS times series. *Revista Arvore, 35*, 699-705

Dai, A.G. (2011). Drought under global warming: a review. *Wiley Interdisciplinary Reviews-Climate Change, 2*, 45-65

Dai, A.G. (2013). Increasing drought under global warming in observations and models. *Nature Climate Change, 3*, 52-58

Daly, C., Taylor, G.H., Gibson, W.P., Parzybok, T.W., Johnson, G.L., & Pasteris, P.A. (2000). High-quality spatial climate data sets for the United States and beyond. *Transactions of the Asae, 43*, 1957-1962

de Bie, S., Ketner, P., Paasse, M., & Geerling, C. (1998). Woody plant phenology in the West Africa savanna. *Journal of Biogeography, 25*, 883-900

Decker, M., Brunke, M.A., Wang, Z., Sakaguchi, K., Zeng, X.B., & Bosilovich, M.G. (2012). Evaluation of the Reanalysis Products from GSFC, NCEP, and ECMWF Using Flux Tower Observations. *Journal of Climate, 25*, 1916-1944

DeFries, R., Hansen, M., & Townshend, J. (1995). Global discrimination of land cover types from metrics derived from AVHRR pathfinder data. *Remote Sensing of Environment, 54*, 209-222

Desai, A.R., Richardson, A.D., Moffat, A.M., Kattge, J., Hollinger, D.Y., Barr, A., Falge, E., Noormets, A., Papale, D., Reichstein, M., & Stauch, V.J. (2008). Cross-site evaluation of eddy covariance GPP and RE decomposition techniques. *Agricultural and Forest Meteorology, 148*, 821-838

Doll, P. (2002). Impact of climate change and variability on irrigation requirements: A global perspective. *Climatic Change, 54*, 269-293

Donald, P.F. (2004). Biodiversity impacts of some agricultural commodity production systems. *Conservation Biology, 18*, 17-37

Dong, J., Xiao, X., Wagle, P., Zhang, G., Zhou, Y., Jin, C., Torn, M.S., Meyers, T.P., Suyker, A.E., Wang, J., Yan, H., Biradar, C., & Moore Iii, B. (2015). Comparison of four EVI-based models for estimating gross primary production of maize and soybean croplands and tallgrass prairie under severe drought. *Remote Sensing of Environment, 162*, 154-168

Dong, J.W., Xiao, X.M., Chen, B.Q., Torbick, N., Jin, C., Zhang, G.L., & Biradar, C. (2013). Mapping deciduous rubber plantations through integration of PALSAR and multi-temporal Landsat imagery. *Remote Sensing of Environment, 134*, 392-402

Dunn, A.L., Barford, C.C., Wofsy, S.C., Goulden, M.L., & Daube, B.C. (2007). A long-term record of carbon exchange in a boreal black spruce forest: means, responses to interannual variability, and decadal trends. *Global Change Biology, 13*, 577-590

Earl, H.J., & Davis, R.F. (2003). Effect of drought stress on leaf and whole canopy radiation use efficiency and yield of maize. *Agronomy Journal, 95*, 688-696

Eck, T.F., & Dye, D.G. (1991). Satellite Estimation of Incident Photosynthetically Active Radiation Using Ultraviolet Reflectance. *Remote Sensing of Environment, 38*, 135-146

Ehleringer, J., & Björkman, O. (1977). Quantum Yields for CO_2 Uptake in C_3 and C_4 Plants: Dependence on Temperature, CO_2 , and O_2 Concentration. *Plant Physiology, 59*, 86-90

Falge, E., Baldocchi, D., Olson, R., Anthoni, P., Aubinet, M., Bernhofer, C., Burba, G., Ceulemans, R., Clement, R., Dolman, H., Granier, A., Gross, P., Grunwald, T., Hollinger, D., Jensen, N.O., Katul, G., Keronen, P., Kowalski, A., Lai, C.T., Law, B.E., Meyers, T., Moncrieff, H., Moors, E., Munger, J.W., Pilegaard, K., Rannik, U., Rebmann, C., Suyker, A., Tenhunen, J., Tu, K., Verma, S., Vesala, T., Wilson, K., & Wofsy, S. (2001). Gap filling strategies for defensible annual sums of net ecosystem exchange. *Agricultural and Forest Meteorology, 107*, 43-69

Farooq, M., Wahid, A., Kobayashi, N., Fujita, D., & Basra, S.M.A. (2009). Plant drought stress: effects, mechanisms and management. *Agronomy for Sustainable Development, 29*, 185-212

Feng, X., Liu, G., Chen, J.M., Chen, M., Liu, J., Ju, W.M., Sun, R., & Zhou, W. (2007). Net primary productivity of China's terrestrial ecosystems from a process model driven by remote sensing. *Journal of Environmental Management, 85*, 563-573

Ferreira, L.G., & Huete, A.R. (2004). Assessing the seasonal dynamics of the Brazilian Cerrado vegetation through the use of spectral vegetation indices. *International Journal of Remote Sensing, 25*, 1837-1860

Ferreira, L.G., Yoshioka, H., Huete, A., & Sano, E.E. (2003). Seasonal landscape and spectral vegetation index dynamics in the Brazilian Cerrado: An analysis within the Large-Scale Biosphere-Atmosphere Experiment in Amazonia (LBA). *Remote Sensing of Environment, 87*, 534-550

Field, C.B., Randerson, J.T., & Malmstrom, C.M. (1995). Global Net Primary Production - Combining Ecology and Remote-Sensing. *Remote Sensing of Environment, 51*, 74-88

Franca, H., & Setzer, A.W. (1998). AVHRR temporal analysis of a savanna site in Brazil. *International Journal of Remote Sensing, 19*, 3127-3140

Frank, D., Reichstein, M., Bahn, M., Thonicke, K., Frank, D., Mahecha, M.D., Smith, P., van der Velde, M., Vicca, S., Babst, F., Beer, C., Buchmann, N., Canadell, J.G., Ciais, P., Cramer, W., Ibrom, A., Miglietta, F., Poulter, B., Rammig, A., Seneviratne, S.I., Walz, A., Wattenbach, M., Zavala, M.A., & Zscheischler, J. (2015). Effects of

climate extremes on the terrestrial carbon cycle: concepts, processes and potential future impacts. *Glob Chang Biol, 21*, 2861-2880

Friedl, M.A., McIver, D.K., Hodges, J.C.F., Zhang, X.Y., Muchoney, D., Strahler, A.H., Woodcock, C.E., Gopal, S., Schneider, A., Cooper, A., Baccini, A., Gao, F., & Schaaf, C. (2002). Global land cover mapping from MODIS: algorithms and early results. *Remote Sensing of Environment, 83*, 287-302

Frouin, R., & Pinker, R.T. (1995). Estimating Photosynthetically Active Radiation (Par) at the Earths Surface from Satellite-Observations. *Remote Sensing of Environment, 51*, 98-107

Fuhrer, J. (2003). Agroecosystern responses to combinations of elevated CO2, ozone, and global climate change. *Agriculture Ecosystems & Environment, 97*, 1-20

Fuller, D.O. (1999). Canopy phenology of some mopane and miombo woodlands in eastern Zambia. *Global Ecology and Biogeography, 8*, 199-209

Fuller, D.O., & Prince, S.D. (1996). Rainfall and foliar dynamics in tropical southern Africa: Potential impacts of global climatic change on savanna vegetation. *Climatic Change, 33*, 69-96

Gitelson, A.A., Peng, Y., Masek, J.G., Rundquist, D.C., Verma, S., Suyker, A., Baker, J.M., Hatfield, J.L., & Meyers, T. (2012). Remote estimation of crop gross primary production with Landsat data. *Remote Sensing of Environment, 121*, 404-414

Gitelson, A.A., Vina, A., Verma, S.B., Rundquist, D.C., Arkebauer, T.J., Keydan, G., Leavitt, B., Ciganda, V., Burba, G.G., & Suyker, A.E. (2006). Relationship between gross primary production and chlorophyll content in crops: Implications for the synoptic monitoring of vegetation productivity. *Journal of Geophysical Research-Atmospheres, 111*

Gleckler, P.J., Taylor, K.E., & Doutriaux, C. (2008). Performance metrics for climate models. *Journal of Geophysical Research-Atmospheres, 113*

Goerner, A., Reichstein, M., Tomelleri, E., Hanan, N., Rambal, S., Papale, D., Dragoni, D., & Schmullius, C. (2011). Remote sensing of ecosystem light use efficiency with MODIS-based PRI. *Biogeosciences, 8*, 189-202

Gong, P., Wang, J., Yu, L., Zhao, Y., Zhao, Y., Liang, L., Niu, Z., Huang, X., Fu, H., Liu, S., Li, C., Li, X., Fu, W., Liu, C., Xu, Y., Wang, X., Cheng, Q., Hu, L., Yao, W., Zhang, H., Zhu, P., Zhao, Z., Zhang, H., Zheng, Y., Ji, L., Zhang, Y., Chen, H., Yan, A., Guo, J., Yu, L., Wang, L., Liu, X., Shi, T., Zhu, M., Chen, Y., Yang, G., Tang, P., Xu, B., Giri, C., Clinton, N., Zhu, Z., Chen, J., & Chen, J. (2013). Finer resolution observation and monitoring of global land cover: first mapping results with Landsat TM and ETM+ data. *International Journal of Remote Sensing, 34*, 2607-2654

Gonzalez, J.A., & Calbo, J. (2002). Modelled and measured ratio of PAR to global radiation under cloudless skies. *Agricultural and Forest Meteorology, 110*, 319-325

Granier, A., Reichstein, M., Breda, N., Janssens, I.A., Falge, E., Ciais, P., Grunwald, T., Aubinet, M., Berbigier, P., Bernhofer, C., Buchmann, N., Facini, O., Grassi, G., Heinesch, B., Ilvesniemi, H., Keronen, P., Knohl, A., Kostner, B., Lagergren, F., Lindroth, A., Longdoz, B., Loustau, D., Mateus, J., Montagnani, L., Nys, C., Moors, E., Papale, D., Peiffer, M., Pilegaard, K., Pita, G., Pumpanen, J., Rambal, S., Rebmann, C., Rodrigues, A., Seufert, G., Tenhunen, J., Vesala, I., & Wang, Q. (2007). Evidence for soil water control on carbon and water dynamics in European forests during the extremely dry year: 2003. *Agricultural and Forest Meteorology, 143*, 123-145

Griffis, T.J., Baker, J.M., & Zhang, J. (2005). Seasonal dynamics and partitioning of isotopic CO2 exchange in C-3/C-4 managed ecosystem. *Agricultural and Forest Meteorology, 132*, 1-19

Guanter, L., Zhang, Y.G., Jung, M., Joiner, J., Voigt, M., Berry, J.A., Frankenberg, C., Huete, A.R., Zarco-Tejada, P., Lee, J.E., Moran, M.S., Ponce-Campos, G., Beer, C., Camps-Valls, G., Buchmann, N., Gianelle, D., Klumpp, K., Cescatti, A., Baker, J.M., & Griffis, T.J. (2014). Global and time-resolved monitoring of crop photosynthesis with chlorophyll fluorescence. *Proceedings of the National Academy of Sciences of the United States of America, 111*, E1327-E1333

Gupta, H.V., Kling, H., Yilmaz, K.K., & Martinez, G.F. (2009). Decomposition of the mean squared error and NSE performance criteria: Implications for improving hydrological modelling. *Journal of Hydrology, 377*, 80-91

Haberl, H., Erb, K.H., Krausmann, F., Gaube, V., Bondeau, A., Plutzar, C., Gingrich, S., Lucht, W., & Fischer-Kowalski, M. (2007). Quantifying and mapping the human appropriation of net primary production in earth's terrestrial ecosystems. *Proceedings of the National Academy of Sciences of the United States of America, 104*, 12942-12945

Hanjra, M.A., & Qureshi, M.E. (2010). Global water crisis and future food security in an era of climate change. *Food Policy, 35*, 365-377

Hansen, M.C., Defries, R.S., Townshend, J.R.G., & Sohlberg, R. (2000). Global land cover classification at 1 km spatial resolution using a classification tree approach. *International Journal of Remote Sensing, 21*, 1331-1364

Hansen, M.C., Potapov, P.V., Moore, R., Hancher, M., Turubanova, S.A., Tyukavina, A., Thau, D., Stehman, S.V., Goetz, S.J., Loveland, T.R., Kommareddy, A., Egorov, A., Chini, L., Justice, C.O., & Townshend, J.R.G. (2013). High-Resolution Global Maps of 21st-Century Forest Cover Change. *Science, 342*, 850-853

He, M., Ju, W., Zhou, Y., Chen, J., He, H., Wang, S., Wang, H., Guan, D., Yan, J., Li, Y., Hao, Y., & Zhao, F. (2013). Development of a two-leaf light use efficiency model for improving the calculation of terrestrial gross primary productivity. *Agricultural and Forest Meteorology, 173*, 28-39

Heinsch, F.A., Zhao, M.S., Running, S.W., Kimball, J.S., Nemani, R.R., Davis, K.J., Bolstad, P.V., Cook, B.D., Desai, A.R., Ricciuto, D.M., Law, B.E., Oechel, W.C., Kwon, H., Luo, H.Y., Wofsy, S.C., Dunn, A.L., Munger, J.W., Baldocchi, D.D., Xu, L.K., Hollinger, D.Y., Richardson, A.D., Stoy, P.C., Siqueira, M.B.S., Monson, R.K., Burns, S.P., & Flanagan, L.B. (2006). Evaluation of remote sensing based terrestrial productivity from MODIS using regional tower eddy flux network observations. *Ieee Transactions on Geoscience and Remote Sensing, 44*, 1908-1925

Higgins, S.I., Delgado-Cartay, M.D., February, E.C., & Combrink, H.J. (2011). Is there a temporal niche separation in the leaf phenology of savanna trees and grasses? *Journal of Biogeography, 38*, 2165-2175

Hoerling, M., Eischeid, J., Kumar, A., Leung, R., Mariotti, A., Mo, K., Schubert, S., & Seager, R. (2014). Causes and Predictability of the 2012 Great Plains Drought. *Bulletin of the American Meteorological Society, 95*, 269-282

Hoffmann, W.A., da Silva, E.R., Machado, G.C., Bucci, S.J., Scholz, F.G., Goldstein, G., & Meinzer, F.C. (2005). Seasonal leaf dynamics across a tree density gradient in a Brazilian savanna. *Oecologia, 145*, 307-316

Huang, C.Q., Coward, S.N., Masek, J.G., Thomas, N., Zhu, Z.L., & Vogelmann, J.E. (2010a). An automated approach for reconstructing recent forest disturbance history using dense Landsat time series stacks. *Remote Sensing of Environment, 114*, 183-198

Huang, N., Wang, Z.M., Liu, D.W., & Niu, Z. (2010b). Selecting sites for converting farmlands to wetlands in the Sanjiang Plain, Northeast China, based on remote sensing and GIS. *Environmental Management, 46*, 790-800

Huete, A., Didan, K., Miura, T., Rodriguez, E.P., Gao, X., & Ferreira, L.G. (2002). Overview of the radiometric and biophysical performance of the MODIS vegetation indices. *Remote Sensing of Environment, 83*, 195-213

Huete, A.R., Liu, H.Q., Batchily, K., & vanLeeuwen, W. (1997a). A comparison of vegetation indices global set of TM images for EOS-MODIS. *Remote Sensing of Environment, 59*, 440-451

Huete, A.R., Liu, H.Q., Batchily, K., & vanLeeuwen, W. (1997b). A comparison of vegetation indices over a global set of TM images for EOS-MODIS. *Remote Sensing of Environment, 59*, 440-451

Hunt, E.D., Svoboda, M., Wardlow, B., Hubbard, K., Hayes, M., & Arkebauer, T. (2014). Monitoring the effects of rapid onset of drought on non-irrigated maize with agronomic data and climate-based drought indices. *Agricultural and Forest Meteorology, 191*, 1-11

Huntzinger, D.N., Schwalm, C., Michalak, A.M., Schaefer, K., King, A.W., Wei, Y., Jacobson, A., Liu, S., Cook, R.B., Post, W.M., Berthier, G., Hayes, D., Huang, M., Ito, A., Lei, H., Lu, C., Mao, J., Peng, C.H., Peng, S., Poulter, B., Riccuito, D., Shi, X., Tian, H., Wang, W., Zeng, N., Zhao, F., & Zhu, Q. (2013). The North American Carbon Program Multi-Scale Synthesis and Terrestrial Model Intercomparison Project - Part 1: Overview and experimental design. *Geoscientific Model Development, 6*, 2121-2133

Hutley, L.B., Beringer, J., Isaac, P.R., Hacker, J.M., & Cernusak, L.A. (2011). A sub-continental scale living laboratory: Spatial patterns of savanna vegetation over a rainfall gradient in northern Australia. *Agricultural and Forest Meteorology, 151*, 1417-1428

Hüttich, C., Gessner, U., Herold, M., Strohbach, B.J., Schmidt, M., Keil, M., & Dech, S. (2009). On the suitability of MODIS time series netrics to map vegetation types in dry savanna ecosystems: a case study in the Kalahari of NE Namibia. *Remote Sensing, 1*, 620-643

Huttich, C., Herold, M., Strohbach, B., & Dech, S. (2011). Integrating in-situ, Landsat, and MODIS data for mapping in Southern African savannas: experiences of LCCS-based land-cover mapping in the Kalahari in Namibia. *Environmental Monitoring and Assessment, 176*, 531-547

Jacovides, C.P., Timvios, F.S., Papaioannou, G., Asimakopoulos, D.N., & Theofilou, C.M. (2004). Ratio of PAR to broadband solar radiation measured in Cyprus. *Agricultural and Forest Meteorology, 121*, 135-140

Ji, L., & Peters, A.J. (2003). Assessing vegetation response to drought in the northern Great Plains using vegetation and drought indices. *Remote Sensing of Environment, 87*, 85-98

Jiang, X.Y., & Yang, Z.L. (2012). Projected changes of temperature and precipitation in Texas from downscaled global climate models. *Climate Research, 53*, 229-244

Jin, C., Xiao, X., Wagle, P., Griffis, T., Dong, J., Wu, C., Qin, Y., & Cook, D.R. (2015). Effects of in-situ and reanalysis climate data on estimation of cropland gross primary production using the Vegetation Photosynthesis Model. *Agricultural and Forest Meteorology, 213*, 240-250

Jin, H.A., Li, A.N., Bian, J.H., Zhang, Z.J., Huang, C.Q., & Li, M.X. (2013). Validation of global land surface satellite (GLASS) downward shortwave radiation product in the rugged surface. *Journal of Mountain Science, 10*, 812-823

John A. Richards, & Jia, X. (1999). *Remote Sensing Digital Image Analysis: An Introduction*. Berlin; New York: Springer

John, R., Chen, J., Noormets, A., Xiao, X., Xu, J., Lu, N., & Chen, S. (2013). Modelling gross primary production in semi-arid Inner Mongolia using MODIS imagery and eddy covariance data. *International Journal of Remote Sensing, 34*, 2829-2857

Joiner, J., Guanter, L., Lindstrot, R., Voigt, M., Vasilkov, A.P., Middleton, E.M., Huemmrich, K.F., Yoshida, Y., & Frankenberg, C. (2013). Global monitoring of terrestrial chlorophyll fluorescence from moderate-spectral-resolution near-infrared satellite measurements: methodology, simulations, and application to GOME-2. *Atmospheric Measurement Techniques, 6*, 2803-2823

Jolly, W.M., & Running, S.W. (2004). Effects of precipitation and soil water potential on drought deciduous phenology in the Kalahari. *Global Change Biology, 10*, 303-308

Jones, M.O., Kimball, J.S., Jones, L.A., & McDonald, K.C. (2012). Satellite passive microwave detection of North America start of season. *Remote Sensing of Environment, 123*, 324-333

Kalfas, J.L., Xiao, X.M., Vanegas, D.X., Verma, S.B., & Suyker, A.E. (2011a). Modeling gross primary production of irrigated and rain-fed maize using MODIS imagery and CO2 flux tower data. *Agricultural and Forest Meteorology, 151*, 1514-1528

Kalfas, J.L., Xiao, X.M., Vanegas, D.X., Verma, S.B., & Suyker, A.E. (2011b). Modeling gross primary production of irrigated and rain-fed maize using MODIS imagery and CO(2) flux tower data. *Agricultural and Forest Meteorology, 151*, 1514-1528

Kanniah, K.D., Beringer, J., & Hutley, L.B. (2011). Environmental controls on the spatial variability of savanna productivity in the Northern Territory, Australia. *Agricultural and Forest Meteorology, 151*, 1429-1439

Kanniah, K.D., Beringer, J., Hutley, L.B., Tapper, N.J., & Zhu, X. (2009). Evaluation of Collections 4 and 5 of the MODIS Gross Primary Productivity product and algorithm improvement at a tropical savanna site in northern Australia. *Remote Sensing of Environment, 113*, 1808-1822

Karnauskas, K.B., Ruiz-Barradas, A., Nigam, S., & Busalacchi, A.J. (2008). North American Droughts in ERA-40 Global and NCEP North American Regional Reanalyses: A Palmer Drought Severity Index Perspective. *Journal of Climate, 21*, 2102-2123

Karnieli, A., Agam, N., Pinker, R.T., Anderson, M., Imhoff, M.L., Gutman, G.G., Panov, N., & Goldberg, A. (2010). Use of NDVI and Land Surface Temperature for Drought Assessment: Merits and Limitations. *Journal of Climate, 23*, 618-633

Kellner, O., & Niyogi, D. (2014). Assessing drought vulnerability of agricultural production systems in context of the 2012 drought. *Journal of Animal Science, 92*, 2811-2822

Kennedy, A., Dong, X.Q., & Xi, B.K. (2011). A Comparison of MERRA and NARR Reanalyses with the DOE ARM SGP Data. *Journal of Climate, 24*, 4541-4557

Kennedy, R.E., Yang, Z.G., & Cohen, W.B. (2010). Detecting trends in forest disturbance and recovery using yearly Landsat time series: 1. LandTrendr - Temporal segmentation algorithms. *Remote Sensing of Environment, 114*, 2897-2910

Kim, Y., Kimball, J.S., Zhang, K., & McDonald, K.C. (2012). Satellite detection of increasing Northern Hemisphere non-frozen seasons from 1979 to 2008: Implications for regional vegetation growth. *Remote Sensing of Environment, 121*, 472-487

Kross, A., Fernandes, R., Seaquist, J., & Beaubien, E. (2011). The effect of the temporal resolution of NDVI data on season onset dates and trends across Canadian broadleaf forests. *Remote Sensing of Environment, 115*, 1564-1575

Kuenzer, C., & Knauer, K. (2013). Remote sensing of rice crop areas. *International Journal of Remote Sensing, 34*, 2101-2139

Kumar, A., Chen, M.Y., Hoerling, M., & Eischeid, J. (2013). Do extreme climate events require extreme forcings? *Geophysical Research Letters, 40*, 3440-3445

Kutsch, W.L., Hanan, N., Scholes, B., McHugh, I., Kubheka, W., Eckhardt, H., & Williams, C. (2008). Response of carbon fluxes to water relations in a savanna ecosystem in South Africa. *Biogeosciences, 5*, 1797-1808

Laba, M., Smith, S.D., & Degloria, S.D. (1997). Landsat-based land cover mapping in the lower Yuna River watershed in the Dominican Republic. *International Journal of Remote Sensing, 18*, 3011-3025

Landis, D.A., Gardiner, M.M., van der Werf, W., & Swinton, S.M. (2008). Increasing corn for biofuel production reduces biocontrol services in agricultural landscapes. *Proceedings of the National Academy of Sciences of the United States of America, 105*, 20552-20557

Larcher, W. (2003). *Larcher, W. Physiological plant ecology*. (4th ed.). Berlin: Springer

Li, C.S., Mosier, A., Wassmann, R., Cai, Z.C., Zheng, X.H., Huang, Y., Tsuruta, H., Boonjawat, J., & Lantin, R. (2004). Modeling greenhouse gas emissions from rice-based production systems: Sensitivity and upscaling. *Global Biogeochemical Cycles, 18*

Li, P., Feng, Z.M., Jiang, L.G., Liu, Y.J., & Xiao, X.M. (2012). Changes in rice cropping systems in the Poyang Lake Region, China during 2004-2010. *Journal of Geographical Sciences, 22*, 653-668

Li, Z.Q., Yu, G.R., Xiao, X.M., Li, Y.N., Zhao, X.Q., Ren, C.Y., Zhang, L.M., & Fu, Y.L. (2007). Modeling gross primary production of alpine ecosystems in the Tibetan

Plateau using MODIS images and climate data. *Remote Sensing of Environment, 107*, 510-519

Liu, J., Liu, M., Tian, H., Zhuang, D., Zhang, Z., Zhang, W., Tang, X., & Deng, X. (2005). Spatial and temporal patterns of China's cropland during 1990–2000: An analysis based on Landsat TM data. *Remote Sensing of Environment, 98*, 442-456

Liu, Y., Zhou, Y., Ju, W., Wang, S., Wu, X., He, M., & Zhu, G. (2014). Impacts of droughts on carbon sequestration by China's terrestrial ecosystems from 2000 to 2011. *Biogeosciences, 11*, 2583-2599

Lobell, D.B., & Asner, G.P. (2003). Climate and Management Contributions to Recent Trends in U.S. Agricultural Yields. *Science, 299*, 1032

Loveland, T.R., Reed, B.C., Brown, J.F., Ohlen, D.O., Zhu, Z., Yang, L., & Merchant, J.W. (2000). Development of a global land cover characteristics database and IGBP DISCover from 1 km AVHRR data. *International Journal of Remote Sensing, 21*, 1303-1330

Ludwig, F., de Kroon, H., Berendse, F., & Prins, H.H.T. (2004). The influence of savanna trees on nutrient, water and light availability and the understorey vegetation. *Plant Ecology, 170*, 93-105

Mallya, G., Zhao, L., Song, X.C., Niyogi, D., & Govindaraju, R.S. (2013). 2012 Midwest Drought in the United States. *Journal of Hydrologic Engineering, 18*, 737-745

Markovic, M., Jones, C.G., Winger, K., & Paquin, D. (2009). The surface radiation budget over North America: gridded data assessment and evaluation of regional climate models. *International Journal of Climatology, 29*, 2226-2240

Masek, J.G., Huang, C.Q., Wolfe, R., Cohen, W., Hall, F., Kutler, J., & Nelson, P. (2008). North American forest disturbance mapped from a decadal Landsat record. *Remote Sensing of Environment, 112*, 2914-2926

McCloy, K.R., Smith, F.R., & Robinson, M.R. (1987). Monitoring rice areas using LANDSAT MSS data. *International Journal of Remote Sensing, 8*, 741-749

McGuire, A.D., Melillo, J.M., Joyce, L.A., Kicklighter, D.W., Grace, A.L., Moore, B., III, & Vorosmarty, C.J. (1992). Interactions between carbon and nitrogen dynamics in

estimating net primary productivity for potential vegetation in North America. *Global Biogeochemical Cycles, 6*, 101-124

McKee, T.B., Doesken, N.J., & Kleist, J. (1993). The relationship of drought frequency and duration to time scales. In, *Proceedings of the Eighth conference on applied climatolog* (pp. 17 - 22). Anaheim, California

Merbold, L., Ardo, J., Arneth, A., Scholes, R.J., Nouvellon, Y., de Grandcourt, A., Archibald, S., Bonnefond, J.M., Boulain, N., Brueggemann, N., Bruemmer, C., Cappelaere, B., Ceschia, E., El-Khidir, H.A.M., El-Tahir, B.A., Falk, U., Lloyd, J., Kergoat, L., Le Dantec, V., Mougin, E., Muchinda, M., Mukelabai, M.M., Ramier, D., Roupsard, O., Timouk, F., Veenendaal, E.M., & Kutsch, W.L. (2009). Precipitation as driver of carbon fluxes in 11 African ecosystems. *Biogeosciences, 6*, 1027-1041

Merbold, L., Ziegler, W., Mukelabai, M.M., & Kutsch, W.L. (2011). Spatial and temporal variation of CO_2 efflux along a disturbance gradient in a miombo woodland in Western Zambia. *Biogeosciences, 8*, 147-164

Mesinger, F., DiMego, G., Kalnay, E., Mitchell, K., Shafran, P.C., Ebisuzaki, W., Jovic, D., Woollen, J., Rogers, E., Berbery, E.H., Ek, M.B., Fan, Y., Grumbine, R., Higgins, W., Li, H., Lin, Y., Manikin, G., Parrish, D., & Shi, W. (2006). North American regional reanalysis. *Bulletin of the American Meteorological Society, 87*, 343-360

Meyers, T.P., & Hollinger, S.E. (2004). An assessment of storage terms in the surface energy balance of maize and soybean. *Agricultural and Forest Meteorology, 125*, 105-115

Monfreda, C., Ramankutty, N., & Foley, J.A. (2008). Farming the planet: 2. Geographic distribution of crop areas, yields, physiological types, and net primary production in the year 2000. *Global Biogeochemical Cycles, 22*

Monteith, J.L. (1972a). Solar-Radiation and Productivity in Tropical Ecosystems. *Journal of Applied Ecology, 9*, 747-766

Monteith, J.L. (1972b). Solar radiation and productivity in tropical ecosystems. *Journal of Applied Ecology*, 747-766

Monteith, J.L., & Moss, C.J. (1977). *Climate and the Efficiency of Crop Production in Britain [and Discussion]*.

Montgomery, D.R. (2007). Soil erosion and agricultural sustainability. *Proceedings of the National Academy of Sciences of the United States of America, 104*, 13268-13272

Moody, A., & Johnson, D.M. (2001). Land-surface phenologies from AVHRR using the discrete fourier transform. *Remote Sensing of Environment, 75*, 305-323

Moureaux, C., Debacq, A., Hoyaux, J., Suleau, M., Tourneur, D., Vancutsem, F., Bodson, B., & Aubinet, M. (2008). Carbon balance assessment of a Belgian winter wheat crop (Triticum aestivum L.). *Global Change Biology, 14*, 1353-1366

Nguyen, N.V., & Ferrero, A. (2006). Meeting the challenges of global rice production. *Paddy and Water Environment, 4*, 1-9

Noormets, A., Gavazzi, M.J., Mcnulty, S.G., Domec, J.C., Sun, G., King, J.S., & Chen, J.Q. (2010). Response of carbon fluxes to drought in a coastal plain loblolly pine forest. *Global Change Biology, 16*, 272-287

Okamoto, K., & Fukuhara, M. (1996). Estimation of paddy field area using the area ratio of categories in each mixel of Landsat TM. *International Journal of Remote Sensing, 17*, 1735-1749

Okamoto, K., Yamakawa, S., & Kawashima, H. (1998). Estimation of flood damage to rice production in North Korea in 1995. *International Journal of Remote Sensing, 19*, 365-371

Oliveira, T., Carvalho, L., Oliveira, L., Lacerda, W., & J., A.F. (2012). NDVI time series for mapping phenological variability of forests across the cerrado biome in Minas Gerais, Brazil. *Phenology and Climate Change* (pp. 253-272): InTech

Otkin, J.A., Anderson, M.C., Hain, C., Mladenova, I.E., Basara, J.B., & Svoboda, M. (2013). Examining Rapid Onset Drought Development Using the Thermal Infrared-Based Evaporative Stress Index. *Journal of Hydrometeorology, 14*, 1057-1074

Panigrahy, S., & Parihar, J.S. (1992). Role of middle infrared bands of Landsat Thematic Mapper in determining the classification accuracy of rice. *International Journal of Remote Sensing, 13*, 2943-2949

Papaioannou, G., Papanikolaou, N., & Retalis, D. (1993). Relationships of Photosynthetically Active Radiation and Shortwave Irradiance. *Theoretical and Applied Climatology, 48,* 23-27

Papale, D., Reichstein, M., Aubinet, M., Canfora, E., Bernhofer, C., Kutsch, W., Longdoz, B., Rambal, S., Valentini, R., Vesala, T., & Yakir, D. (2006). Towards a standardized processing of Net Ecosystem Exchange measured with eddy covariance technique: algorithms and uncertainty estimation. *Biogeosciences, 3,* 571-583

Papale, D., & Valentini, A. (2003). A new assessment of European forests carbon exchanges by eddy fluxes and artificial neural network spatialization. *Global Change Biology, 9,* 525-535

Park, S., & Miura, T. (2011). Moderate-resolution imaging spectroradiometer-based vegetation indices and their fidelity in the tropics. *Journal of Applied Remote Sensing, 5*

Peng, Y., & Gitelson, A.A. (2011). Application of chlorophyll-related vegetation indices for remote estimation of maize productivity. *Agricultural and Forest Meteorology, 151,* 1267-1276

Peng, Y., & Gitelson, A.A. (2012). Remote estimation of gross primary productivity in soybean and maize based on total crop chlorophyll content. *Remote Sensing of Environment, 117,* 440-448

Peng, Y., Gitelson, A.A., Keydan, G., Rundquist, D.C., & Moses, W. (2011). Remote estimation of gross primary production in maize and support for a new paradigm based on total crop chlorophyll content. *Remote Sensing of Environment, 115,* 978-989

Phillips, O.L., van der Heijden, G., Lewis, S.L., Lopez-Gonzalez, G., Aragao, L.E.O.C., Lloyd, J., Malhi, Y., Monteagudo, A., Almeida, S., Davila, E.A., Amaral, I., Andelman, S., Andrade, A., Arroyo, L., Aymard, G., Baker, T.R., Blanc, L., Bonal, D., de Oliveira, A.C.A., Chao, K.J., Cardozo, N.D., da Costa, L., Feldpausch, T.R., Fisher, J.B., Fyllas, N.M., Freitas, M.A., Galbraith, D., Gloor, E., Higuchi, N., Honorio, E., Jimenez, E., Keeling, H., Killeen, T.J., Lovett, J.C., Meir, P., Mendoza, C., Morel, A., Vargas, P.N., Patino, S., Peh, K.S.H., Cruz, A.P., Prieto, A., Quesada, C.A., Ramirez, F., Ramirez, H., Rudas, A., Salamao, R., Schwarz, M., Silva, J., Silveira, M., Slik, J.W.F., Sonke, B., Thomas, A.S., Stropp, J., Taplin, J.R.D., Vasquez, R., & Vilanova, E. (2010). Drought-mortality relationships for tropical forests. *New Phytologist, 187,* 631-646

Pinker, R.T., Zhao, M.S., Wang, H.M., & Wood, E.F. (2010). Impact of satellite based PAR on estimates of terrestrial net primary productivity. *International Journal of Remote Sensing, 31*, 5221-5237

Potter, C., S. Klooster, V. Genovese, C. Hiatt, S. Boriah, V. Kumar, V. Mithal, A. Garg (2012). Terrestrial ecosystem carbon fluxes predicted from MODIS satellite data and large-scale disturbance modeling. *national Journal of Geosciences*

Potter, C.S., Randerson, J.T., Field, C.B., Matson, P.A., Vitousek, P.M., Mooney, H.A., & Klooster, S.A. (1993). Terrestrial Ecosystem Production - a Process Model-Based on Global Satellite and Surface Data. *Global Biogeochemical Cycles, 7*, 811-841

Prince, S.D., Goetz, S.J., & Goward, S.N. (1995). Monitoring Primary Production from Earth Observing Satellites. *Water Air and Soil Pollution, 82*, 509-522

Prince, S.D., & Goward, S.N. (1995). Global primary production: A remote sensing approach. *Journal of Biogeography, 22*, 815-835

Qian, T.T., Dai, A., Trenberth, K.E., & Oleson, K.W. (2006). Simulation of global land surface conditions from 1948 to 2004. Part I: Forcing data and evaluations. *Journal of Hydrometeorology, 7*, 953-975

Qiu, J., Tang, H., Frolking, S., Boles, S., Li, C., Xiao, X., Liu, J., Zhuang, Y., & Qin, X. (2003). Mapping single-, double‐, and triple‐crop agriculture in China at 0.5° × 0.5° by combining county‐scale census data with a remote sensing‐derived land cover map. *Geocarto International, 18*, 3-13

Raich, J.W., Rastetter, E.B., Melillo, J.M., Kicklighter, D.W., Steudler, P.A., Peterson, B.J., Grace, A.L., Moore, B., & Vorosmarty, C.J. (1991). Potential Net Primary Productivity in South-America - Application of a Global-Model. *Ecological Applications, 1*, 399-429

Ramankutty, N., Evan, A.T., Monfreda, C., & Foley, J.A. (2008a). Farming the planet: 1. Geographic distribution of global agricultural lands in the year 2000. *Global Biogeochemical Cycles, 22*

Ramankutty, N., Evan, A.T., Monfreda, C., & Foley, J.A. (2008b). Farming the planet: 1. Geographic distribution of global agricultural lands in the year 2000. *Global Biogeochemical Cycles, 22*, GB1003

Ramankutty, N., & Foley, J.A. (1998). Characterizing patterns of global land use: An analysis of global croplands data. *Global Biogeochemical Cycles, 12*, 667-685

Rao, P.P.N., & Rao, V.R. (1987). Rice crop identification and area estimation using remotely-sensed data from Indian cropping patterns. *International Journal of Remote Sensing, 8*, 639-650

Reda, I., Hickey, J., Long, C., Myers, D., Stoffel, T., Wilcox, S., Michalsky, J.J., Dutton, E.G., & Nelson, D. (2005). Using a blackbody to calculate net longwave responsivity of shortwave solar pyranometers to correct for their thermal offset error during outdoor calibration using the component sum method. *Journal of Atmospheric and Oceanic Technology, 22*, 1531-1540

Reddy, A.R., Chaitanya, K.V., & Vivekanandan, M. (2004). Drought-induced responses of photosynthesis and antioxidant metabolism in higher plants. *Journal of Plant Physiology, 161*, 1189-1202

Reichstein, M., Ciais, P., Papale, D., Valentini, R., Running, S., Viovy, N., Cramer, W., Granier, A., Ogee, J., Allard, V., Aubinet, M., Bernhofer, C., Buchmann, N., Carrara, A., Grunwald, T., Heimann, M., Heinesch, B., Knohl, A., Kutsch, W., Loustau, D., Manca, G., Matteucci, G., Miglietta, F., Ourcival, J.M., Pilegaard, K., Pumpanen, J., Rambal, S., Schaphoff, S., Seufert, G., Soussana, J.F., Sanz, M.J., Vesala, T., & Zhao, M. (2007). Reduction of ecosystem productivity and respiration during the European summer 2003 climate anomaly: a joint flux tower, remote sensing and modelling analysis. *Global Change Biology, 13*, 634-651

Reichstein, M., Falge, E., Baldocchi, D., Papale, D., Aubinet, M., Berbigier, P., Bernhofer, C., Buchmann, N., Gilmanov, T., Granier, A., Grunwald, T., Havrankova, K., Ilvesniemi, H., Janous, D., Knohl, A., Laurila, T., Lohila, A., Loustau, D., Matteucci, G., Meyers, T., Miglietta, F., Ourcival, J.M., Pumpanen, J., Rambal, S., Rotenberg, E., Sanz, M., Tenhunen, J., Seufert, G., Vaccari, F., Vesala, T., Yakir, D., & Valentini, R. (2005). On the separation of net ecosystem exchange into assimilation and ecosystem respiration: review and improved algorithm. *Global Change Biology, 11*, 1424-1439

Ren, J.Q., Chen, Z.X., Zhou, Q.B., & Tang, H.J. (2008). Regional yield estimation for winter wheat with MODIS-NDVI data in Shandong, China. *International Journal of Applied Earth Observation and Geoinformation, 10*, 403-413

Reyer, C.P., Leuzinger, S., Rammig, A., Wolf, A., Bartholomeus, R.P., Bonfante, A., de Lorenzi, F., Dury, M., Gloning, P., Abou Jaoude, R., Klein, T., Kuster, T.M., Martins,

M., Niedrist, G., Riccardi, M., Wohlfahrt, G., de Angelis, P., de Dato, G., Francois, L., Menzel, A., & Pereira, M. (2013). A plant's perspective of extremes: terrestrial plant responses to changing climatic variability. *Glob Chang Biol, 19*, 75-89

Richardson, A., Aubinet, M., Barr, A., Hollinger, D., Ibrom, A., Lasslop, G., & Reichstein, M. (2012). Uncertainty Quantification. In M. Aubinet, T. Vesala, & D. Papale (Eds.), *Eddy Covariance* (pp. 173-209): Springer Netherlands

Rubio, M.A., Lopez, G., Tovar, J., Pozo, D., & Batlles, F.J. (2005). The use of satellite measurements to estimate photosynthetically active radiation. *Physics and Chemistry of the Earth, 30*, 159-164

Ruimy, A., Dedieu, G., & Saugier, B. (1996). TURC: A diagnostic model of continental gross primary productivity and net primary productivity. *Global Biogeochemical Cycles, 10*, 269-285

Ruimy, A., Saugier, B., & Dedieu, G. (1994). Methodology for the estimation of terrestrial net primary production from remotely sensed data. *Journal of Geophysical Research-Atmospheres, 99*, 5263-5283

Running, S., Thornton, P., Nemani, R., & Glassy, J. (2000a). Global Terrestrial Gross and Net Primary Productivity from the Earth Observing System. In O. Sala, R. Jackson, H. Mooney, & R. Howarth (Eds.), *Methods in Ecosystem Science* (pp. 44-57): Springer New York

Running, S.W., Justice, C.O., Salomonson, V., Hall, D., Barker, J., Kaufmann, Y.J., Strahler, A.H., Huete, A.R., Muller, J.P., Vanderbilt, V., Wan, Z.M., Teillet, P., & Carneggie, D. (1994). Terrestrial Remote-Sensing Science and Algorithms Planned for Eos Modis. *International Journal of Remote Sensing, 15*, 3587-3620

Running, S.W., Nemani, R.R., Heinsch, F.A., Zhao, M.S., Reeves, M., & Hashimoto, H. (2004). A continuous satellite-derived measure of global terrestrial primary production. *Bioscience, 54*, 547-560

Running, S.W., Thornton, P.E., Nemani, R., & Glassy, J.M. (2000b). Global terrestrial gross and net primary productivity from the Earth Observing System. In O.E. Sala, R.B. Jackson, H.A. Mooney, & R.W. Howarth (Eds.), *Methods in Ecosystem Science* (pp. 44-57). New York: Springer Verlag

Sakamoto, T., Gitelson, A.A., Wardlow, B.D., Verma, S.B., & Suyker, A.E. (2011). Estimating daily gross primary production of maize based only on MODIS WDRVI and shortwave radiation data. *Remote Sensing of Environment, 115*, 3091-3101

Sakamoto, T., Van Nguyen, N., Ohno, H., Ishitsuka, N., & Yokozawa, M. (2006). Spatio–temporal distribution of rice phenology and cropping systems in the Mekong Delta with special reference to the seasonal water flow of the Mekong and Bassac rivers. *Remote Sensing of Environment, 100*, 1-16

Sakamoto, T., Van Phung, C., Kotera, A., Nguyen, K.D., & Yokozawa, M. (2009). Analysis of rapid expansion of inland aquaculture and triple rice-cropping areas in a coastal area of the Vietnamese Mekong Delta using MODIS time-series imagery. *Landscape and Urban Planning, 92*, 34-46

Sakamoto, T., Yokozawa, M., Toritani, H., Shibayama, M., Ishitsuka, N., & Ohno, H. (2005). A crop phenology detection method using time-series MODIS data. *Remote Sensing of Environment, 96*, 366-374

Scanlon, T.M., & Albertson, J.D. (2004). Canopy scale measurements of CO_2 and water vapor exchange along a precipitation gradient in southern Africa. *Global Change Biology, 10*, 329-341

Scholes, R.J., & Archer, S.R. (1997). Tree-grass interactions in savannas. *Annual Review of Ecology and Systematics, 28*, 517-544

Scholes, R.J., & Hall, D.O. (1996). *The carbon budget of tropical savannas, woodlands and grasslands*. New York: John Wiley and Sons

Schroeder, T.A., Hember, R., Coops, N.C., & Liang, S.L. (2009). Validation of Solar Radiation Surfaces from MODIS and Reanalysis Data over Topographically Complex Terrain. *Journal of Applied Meteorology and Climatology, 48*, 2441-2458

Schwalm, C.R., Williams, C.A., Schaefer, K., Arneth, A., Bonal, D., Buchmann, N., Chen, J.Q., Law, B.E., Lindroth, A., Luyssaert, S., Reichstein, M., & Richardson, A.D. (2010). Assimilation exceeds respiration sensitivity to drought: A FLUXNET synthesis. *Global Change Biology, 16*, 657-670

Schwalm, C.R., Williams, C.A., Schaefer, K., Baldocchi, D., Black, T.A., Goldstein, A.H., Law, B.E., Oechel, W.C., Kyaw, T.P.U., & Scott, R.L. (2012). Reduction in

carbon uptake during turn of the century drought in western North America. *Nature Geoscience, 5*, 551-556

Shalaby, A., & Tateishi, R. (2007). Remote sensing and GIS for mapping and monitoring land cover and land-use changes in the Northwestern coastal zone of Egypt. *Applied Geography, 27*, 28-41

Shi, Z., Thomey, M.L., Mowll, W., Litvak, M., Brunsell, N.A., Collins, S.L., Pockman, W.T., Smith, M.D., Knapp, A.K., & Luo, Y. (2014). Differential effects of extreme drought on production and respiration: synthesis and modeling analysis. *Biogeosciences, 11*, 621-633

Sims, D.A., Rahman, A.F., Cordova, V.D., El-Masri, B.Z., Baldocchi, D.D., Flanagan, L.B., Goldstein, A.H., Hollinger, D.Y., Misson, L., Monson, R.K., Oechel, W.C., Schmid, H.P., Wofsy, S.C., & Xu, L.K. (2006). On the use of MODIS EVI to assess gross primary productivity of North American ecosystems. *Journal of Geophysical Research-Biogeosciences, 111*

Sitch, S., Huntingford, C., Gedney, N., Levy, P.E., Lomas, M., Piao, S.L., Betts, R., Ciais, P., Cox, P., Friedlingstein, P., Jones, C.D., Prentice, I.C., & Woodward, F.I. (2008). Evaluation of the terrestrial carbon cycle, future plant geography and climate-carbon cycle feedbacks using five Dynamic Global Vegetation Models (DGVMs). *Global Change Biology, 14*, 2015-2039

Sjostrom, M., Ardo, J., Arneth, A., Boulain, N., Cappelaere, B., Eklundh, L., de Grandcourt, A., Kutsch, W.L., Merbold, L., Nouvellon, Y., Scholes, R.J., Schubert, P., Seaquist, J., & Veenendaal, E.M. (2011). Exploring the potential of MODIS EVI for modeling gross primary production across African ecosystems. *Remote Sensing of Environment, 115*, 1081-1089

Sjostrom, M., Ardo, J., Eklundh, L., El-Tahir, B.A., El-Khidir, H.A.M., Hellstrom, M., Pilesjo, P., & Seaquist, J. (2009). Evaluation of satellite based indices for gross primary production estimates in a sparse savanna in the Sudan. *Biogeosciences, 6*, 129-138

Sjöström, M., Zhao, M., Archibald, S., Arneth, A., Cappelaere, B., Falk, U., de Grandcourt, A., Hanan, N., Kergoat, L., Kutsch, W., Merbold, L., Mougin, E., Nickless, A., Nouvellon, Y., Scholes, R.J., Veenendaal, E.M., & Ardö, J. (2013). Evaluation of MODIS gross primary productivity for Africa using eddy covariance data. *Remote Sensing of Environment, 131*, 275-286

Skarpe, C. (1992). Dynamics of savanna ecosystems. *Journal of Vegetation Science, 3*, 293-300

Smith, P., Martino, D., Cai, Z., Gwary, D., Janzen, H., Kumar, P., McCarl, B., Ogle, S., O'Mara, F., Rice, C., Scholes, B., & Sirotenko, O. (2007). Agriculture. In Climate Change 2007: Mitigation. Contribution of Working Group III to the Fourth Assessment Report of the Intergovernmental Panel on Climate Change. Cambridge University Press, Cambridge, United Kingdom and New York, NY, USA

Spiegelaar, N.F., & Tsuji, L.J.S. (2013). Impact of Euro-Canadian agrarian practices: in search of sustainable import-substitution strategies to enhance food security in subarctic Ontario, Canada. *Rural and Remote Health, 13*

Stanhill, G., & Cohen, S. (2001). Global dimming: a review of the evidence for a widespread and significant reduction in global radiation with discussion of its probable causes and possible agricultural consequences. *Agricultural and Forest Meteorology, 107*, 255-278

Stoy, P.C., Katul, G.G., Siqueira, M.B.S., Juang, J.Y., Novick, K.A., Uebelherr, J.M., & Oren, R. (2006). An evaluation of models for partitioning eddy covariance-measured net ecosystem exchange into photosynthesis and respiration. *Agricultural and Forest Meteorology, 141*, 2-18

Sun, H., Huang, J., Huete, A.R., Peng, D., & Zhang, F. (2009). Mapping paddy rice with multi-date moderate-resolution imaging spectroradiometer (MODIS) data in China. *Journal of Zhejiang University-Science A, 10*, 1509-1522

Suyker, A.E., Verma, S.B., Burba, G.G., & Arkebauer, T.J. (2005). Gross primary production and ecosystem respiration of irrigated maize and irrigated soybean during a growing season. *Agricultural and Forest Meteorology, 131*, 180-190

Svoboda, M., LeComte, D., Hayes, M., Heim, R., Gleason, K., Angel, J., Rippey, B., Tinker, R., Palecki, M., Stooksbury, D., Miskus, D., & Stephens, S. (2002). The drought monitor. *Bulletin of the American Meteorological Society, 83*, 1181-1190

Taylor, K.E. (2001). Summarizing multiple aspects of model performance in a single diagram. *Journal of Geophysical Research-Atmospheres, 106*, 7183-7192

Tian, Y.H., Zhou, L.M., Romanov, P., Yu, B., & EK, M. (2012). Improving monitoring of tropical forests and their characterizations in NCEP models. In, *NOAA Satellite Science Week Meeting*. Kansas City, MO

Tilman, D., Fargione, J., Wolff, B., D'Antonio, C., Dobson, A., Howarth, R., Schindler, D., Schlesinger, W.H., Simberloff, D., & Swackhamer, D. (2001). Forecasting agriculturally driven global environmental change. *Science, 292*, 281-284

Townsend, P.A., Singh, A., Foster, J.R., Rehberg, N.J., Kingdon, C.C., Eshleman, K.N., & Seagle, S.W. (2012). A general Landsat model to predict canopy defoliation in broadleaf deciduous forests. *Remote Sensing of Environment, 119*, 255-265

Troy, T.J., & Wood, E.F. (2009). Comparison and evaluation of gridded radiation products across northern Eurasia. *Environmental Research Letters, 4*

Tucker, C.J. (1979a). Comparison of satellite sensor bands for vegetation monitoring. *Photogrammetric Engineering and Remote Sensing, 45*, 655-655

Tucker, C.J. (1979b). Red and photographic infrared linear combinations for monitoring vegetation. *Remote Sensing of Environment, 8*, 127-150

Turner, M.D., & Congalton, R.G. (1998). Classification of multi-temporal SPOT-XS satellite data for mapping rice fields on a West African floodplain. *International Journal of Remote Sensing, 19*, 21-41

van der Molen, M.K., Dolman, A.J., Ciais, P., Eglin, T., Gobron, N., Law, B.E., Meir, P., Peters, W., Phillips, O.L., Reichstein, M., Chen, T., Dekker, S.C., Doubková, M., Friedl, M.A., Jung, M., van den Hurk, B.J.J.M., de Jeu, R.A.M., Kruijt, B., Ohta, T., Rebel, K.T., Plummer, S., Seneviratne, S.I., Sitch, S., Teuling, A.J., van der Werf, G.R., & Wang, G. (2011). Drought and ecosystem carbon cycling. *Agricultural and Forest Meteorology, 151*, 765-773

Van Oost, K., Quine, T.A., Govers, G., De Gryze, S., Six, J., Harden, J.W., Ritchie, J.C., McCarty, G.W., Heckrath, G., Kosmas, C., Giraldez, J.V., da Silva, J.R.M., & Merckx, R. (2007). The impact of agricultural soil erosion on the global carbon cycle. *Science, 318*, 626-629

Veenendaal, E.M., Kolle, O., & Lloyd, J. (2004). Seasonal variation in energy fluxes and carbon dioxide exchange for a broad-leaved semi-arid savanna (Mopane woodland) in Southern Africa. *Global Change Biology, 10*, 318-328

Veenendaal, E.M., Mantlana, K.B., Pammenter, N.W., Weber, P., Huntsman-Mapila, P., & Lloyd, J. (2008). Growth form and seasonal variation in leaf gas exchange of Colophospermum mopane savanna trees in northwest Botswana. *Tree Physiology, 28*, 417-424

Verma, S.B., Dobermann, A., Cassman, K.G., Walters, D.T., Knops, J.M., Arkebauer, T.J., Suyker, A.E., Burba, G.G., Amos, B., Yang, H.S., Ginting, D., Hubbard, K.G., Gitelson, A.A., & Walter-Shea, E.A. (2005). Annual carbon dioxide exchange in irrigated and rainfed maize-based agroecosystems. *Agricultural and Forest Meteorology, 131*, 77-96

Vermote, E.F., ElSaleous, N., Justice, C.O., Kaufman, Y.J., Privette, J.L., Remer, L., Roger, J.C., & Tanre, D. (1997). Atmospheric correction of visible to middle-infrared EOS-MODIS data over land surfaces: Background, operational algorithm and validation. *Journal of Geophysical Research-Atmospheres, 102*, 17131-17141

Veroustraete, F., Sabbe, H., & Eerens, H. (2002). Estimation of carbon mass fluxes over Europe using the C-Fix model and Euroflux data. *Remote Sensing of Environment, 83*, 376-399

Vicente-Serrano, S.M. (2007). Evaluating the impact of drought using remote sensing in a Mediterranean, semi-arid region. *Natural Hazards, 40*, 173-208

Vrieling, A., de Beurs, K.M., & Brown, M.E. (2011). Variability of African farming systems from phenological analysis of NDVI time series. *Climatic Change, 109*, 455-477

Wagenseil, H., & Samimi, C. (2006). Assessing spatio-temporal variations in plant phenology using Fourier analysis on NDVI time series: results from a dry savannah environment in Namibia. *International Journal of Remote Sensing, 27*, 3455-3471

Wagle, P., & Kakani, V.G. (2014). Environmental control of daytime net ecosystem exchange of carbon dioxide in switchgrass. *Agriculture Ecosystems & Environment, 186*, 170-177

Wagle, P., Xiao, X.M., & Suyker, A.E. (2015). Estimation and analysis of gross primary production of soybean under various management practices and drought conditions. *Isprs Journal of Photogrammetry and Remote Sensing, 99*, 70-83

Wagle, P., Xiao, X.M., Torn, M.S., Cook, D.R., Matamala, R., Fischer, M.L., Jin, C., Dong, J.W., & Biradar, C. (2014). Sensitivity of vegetation indices and gross primary production of tallgrass prairie to severe drought. *Remote Sensing of Environment, 152*, 1-14

Wagle, P., Zhang, Y., Jin, C., & Xiao, X. (2016). Comparison of solar-induced chlorophyll fluorescence, light-use efficiency, and process-based GPP models in maize. *Ecological Applications*, n/a-n/a

Walsh, J.E. (2009). Arctic Cloud Fraction and Radiative Fluxes in Atmospheric Reanalyses. *Journal of Climate, 22*, 2316-2334

Wang, H.S., Jia, G.S., Fu, C.B., Feng, J.M., Zhao, T.B., & Ma, Z.G. (2010a). Deriving maximal light use efficiency from coordinated flux measurements and satellite data for regional gross primary production modeling. *Remote Sensing of Environment, 114*, 2248-2258

Wang, X.H., Piao, S.L., Ciais, P., Li, J.S., Friedlingstein, P., Koven, C., & Chen, A.P. (2011). Spring temperature change and its implication in the change of vegetation growth in North America from 1982 to 2006. *Proceedings of the National Academy of Sciences of the United States of America, 108*, 1240-1245

Wang, Z., Xiao, X.M., & Yan, X.D. (2010b). Modeling gross primary production of maize cropland and degraded grassland in northeastern China. *Agricultural and Forest Meteorology, 150*, 1160-1167

Weber, U., Jung, M., Reichstein, M., Beer, C., Braakhekke, M.C., Lehsten, V., Ghent, D., Kaduk, J., Viovy, N., Ciais, P., Gobron, N., & Odenbeck, C.R. (2009). The interannual variability of Africa's ecosystem productivity: a multi-model analysis. *Biogeosciences, 6*, 285-295

Wehner, M., Easterling, D.R., Lawrimore, J.H., Heim, R.R., Vose, R.S., & Santer, B.D. (2011). Projections of Future Drought in the Continental United States and Mexico. *Journal of Hydrometeorology, 12*, 1359-1377

Wei, Y., Liu, S., Huntzinger, D.N., Michalak, A.M., Viovy, N., Post, W.M., Schwalm, C.R., Schaefer, K., Jacobson, A.R., Lu, C., Tian, H., Ricciuto, D.M., Cook, R.B., Mao, J., & Shi, X. (2013). The North American Carbon Program Multi-scale Synthesis and Terrestrial Model Intercomparison Project – Part 2: Environmental driver data. *Geosci. Model Dev. Discuss., 6*, 5375-5422

West, T.O., & Marland, G. (2002). Net carbon flux from agricultural ecosystems: methodology for full carbon cycle analyses. *Environmental Pollution, 116*, 439-444

Wheeler, T., & von Braun, J. (2013). Climate Change Impacts on Global Food Security. *Science, 341*, 508-513

White, M.A., de Beurs, K.M., Didan, K., Inouye, D.W., Richardson, A.D., Jensen, O.P., O'Keefe, J., Zhang, G., Nemani, R.R., van Leeuwen, W.J.D., Brown, J.F., de Wit, A., Schaepman, M., Lin, X.M., Dettinger, M., Bailey, A.S., Kimball, J., Schwartz, M.D., Baldocchi, D.D., Lee, J.T., & Lauenroth, W.K. (2009). Intercomparison, interpretation, and assessment of spring phenology in North America estimated from remote sensing for 1982-2006. *Global Change Biology, 15*, 2335-2359

Whitley, R.J., Macinnis-Ng, C.M.O., Hutley, L.B., Beringer, J., Zeppel, M., Williams, M., Taylor, D., & Eamus, D. (2011). Is productivity of mesic savannas light limited or water limited? Results of a simulation study. *Global Change Biology, 17*, 3130-3149

Williams, C.A., Hanan, N., Scholes, R.J., & Kutsch, W. (2009). Complexity in water and carbon dioxide fluxes following rain pulses in an African savanna. *Oecologia, 161*, 469-480

Williams, C.A., Hanan, N.P., Neff, J.C., Scholes, R.J., Berry, J.A., Denning, A.S., & Baker, D.F. (2007). Africa and the global carbon cycle. *Carbon Balance and Management, 2*

Williams, I.N., Torn, M.S., Riley, W.J., & Wehner, M.F. (2014). Impacts of climate extremes on gross primary production under global warming. *Environmental Research Letters, 9*

Wolf, S., Eugster, W., Ammann, C., Hani, M., Zielis, S., Hiller, R., Stieger, J., Imer, D., Merbold, L., & Buchmann, N. (2013). Contrasting response of grassland versus forest carbon and water fluxes to spring drought in Switzerland. *Environmental Research Letters, 8*

Woollen, E., Ryan, C.M., & Williams, M. (2012). Carbon Stocks in an African Woodland Landscape: Spatial Distributions and Scales of Variation. *Ecosystems, 15*, 804-818

Wu, C., & Chen, J.M. (2012). The use of precipitation intensity in estimating gross primary production in four northern grasslands. *Journal of Arid Environments, 82*, 11-18

Wu, C.Y. (2012). Use of a vegetation index model to estimate gross primary production in open grassland. *Journal of Applied Remote Sensing, 6*

Wu, C.Y., Chen, J.M., & Huang, N. (2011). Predicting gross primary production from the enhanced vegetation index and photosynthetically active radiation: Evaluation and calibration. *Remote Sensing of Environment, 115*, 3424-3435

Wu, C.Y., Munger, J.W., Niu, Z., & Kuang, D. (2010). Comparison of multiple models for estimating gross primary production using MODIS and eddy covariance data in Harvard Forest. *Remote Sensing of Environment, 114*, 2925-2939

Wu, C.Y., & Niu, Z. (2012). Modelling light use efficiency using vegetation index and land surface temperature from MODIS in Harvard Forest. *International Journal of Remote Sensing, 33*, 2261-2276

Wu, C.Y., Niu, Z., Tang, Q., Huang, W.J., Rivard, B., & Feng, J.L. (2009). Remote estimation of gross primary production in wheat using chlorophyll-related vegetation indices. *Agricultural and Forest Meteorology, 149*, 1015-1021

Wu, W.X., Wang, S.Q., Xiao, X.M., Yu, G.R., Fu, Y.L., & Hao, Y.B. (2008). Modeling gross primary production of a temperate grassland ecosystem in Inner Mongolia, China, using MODIS imagery and climate data. *Science in China Series D-Earth Sciences, 51*, 1501-1512

Wuebbles, D., Meehl, G., Hayhoe, K., Karl, T.R., Kunkel, K., Santer, B., Wehner, M., Colle, B., Fischer, E.M., Fu, R., Goodman, A., Janssen, E., Kharin, V., Lee, H., Li, W.H., Long, L.N., Olsen, S.C., Pan, Z.T., Seth, A., Sheffield, J., & Sun, L.Q. (2014). CMIP5 CLIMATE MODEL ANALYSES Climate Extremes in the United States. *Bulletin of the American Meteorological Society, 95*, 571-583

Xiao, J., Davis, K.J., Urban, N.M., Keller, K., & Saliendra, N.Z. (2011). Upscaling carbon fluxes from towers to the regional scale: Influence of parameter variability and land cover representation on regional flux estimates. *Journal of Geophysical Research: Biogeosciences, 116*, G00J06

Xiao, J., Ollinger, S.V., Frolking, S., Hurtt, G.C., Hollinger, D.Y., Davis, K.J., Pan, Y., Zhang, X., Deng, F., Chen, J., Baldocchi, D.D., Law, B.E., Arain, M.A., Desai, A.R., Richardson, A.D., Sun, G., Amiro, B., Margolis, H., Gu, L., Scott, R.L., Blanken, P.D., & Suyker, A.E. (2014a). Data-driven diagnostics of terrestrial carbon dynamics over North America. *Agricultural and Forest Meteorology, 197*, 142-157

Xiao, J.F., Ollinger, S.V., Frolking, S., Hurtt, G.C., Hollinger, D.Y., Davis, K.J., Pan, Y.D., Zhang, X.Y., Deng, F., Chen, J.Q., Baldocchi, D.D., Law, B.E., Arain, M.A., Desai, A.R., Richardson, A.D., Sun, G., Amiro, B., Margolis, H., Gu, L.H., Scott, R.L., Blanken, P.D., & Suyker, A.E. (2014b). Data-driven diagnostics of terrestrial carbon dynamics over North America. *Agricultural and Forest Meteorology, 197*, 142-157

Xiao, X., Boles, S., Frolking, S., Salas, W., Moore, B., Li, C., He, L., & Zhao, R. (2002a). Observation of flooding and rice transplanting of paddy rice fields at the site to landscape scales in China using VEGETATION sensor data. *International Journal of Remote Sensing, 23*, 3009-3022

Xiao, X., Hollinger, D., Aber, J.D., Goltz, M., Davidson, E.A., & Zhang, Q.Y. (2004a). Satellite-based modeling of gross primary production in an evergreen needleleaf forest. *Remote Sensing of Environment, 89*, 519-534

Xiao, X.M. (2006). Light absorption by leaf chlorophyll and maximum light use efficiency. *Ieee Transactions on Geoscience and Remote Sensing, 44*, 1933-1935

Xiao, X.M., Boles, S., Frolking, S., Li, C.S., Babu, J.Y., Salas, W., & Moore, B. (2006a). Mapping paddy rice agriculture in South and Southeast Asia using multi-temporal MODIS images. *Remote Sensing of Environment, 100*, 95-113

Xiao, X.M., Boles, S., Liu, J.Y., Zhuang, D.F., Frolking, S., Li, C.S., Salas, W., & Moore, B. (2005a). Mapping paddy rice agriculture in southern China using multi-temporal MODIS images. *Remote Sensing of Environment, 95*, 480-492

Xiao, X.M., Boles, S., Liu, J.Y., Zhuang, D.F., & Liu, M.L. (2002b). Characterization of forest types in Northeastern China, using multi-temporal SPOT-4 VEGETATION sensor data. *Remote Sensing of Environment, 82*, 335-348

Xiao, X.M., Hagen, S., Zhang, Q.Y., Keller, M., & Moore, B. (2006b). Detecting leaf phenology of seasonally moist tropical forests in South America with multi-temporal MODIS images. *Remote Sensing of Environment, 103*, 465-473

Xiao, X.M., Hollinger, D., Aber, J., Goltz, M., Davidson, E.A., Zhang, Q.Y., & Moore, B. (2004b). Satellite-based modeling of gross primary production in an evergreen needleleaf forest. *Remote Sensing of Environment, 89*, 519-534

Xiao, X.M., Zhang, Q.Y., Braswell, B., Urbanski, S., Boles, S., Wofsy, S., Berrien, M., & Ojima, D. (2004c). Modeling gross primary production of temperate deciduous broadleaf forest using satellite images and climate data. *Remote Sensing of Environment, 91*, 256-270

Xiao, X.M., Zhang, Q.Y., Hollinger, D., Aber, J., & Moore, B. (2005b). Modeling gross primary production of an evergreen needleleaf forest using modis and climate data. *Ecological Applications, 15*, 954-969

Xiao, X.M., Zhang, Q.Y., Saleska, S., Hutyra, L., De Camargo, P., Wofsy, S., Frolking, S., Boles, S., Keller, M., & Moore, B. (2005c). Satellite-based modeling of gross primary production in a seasonally moist tropical evergreen forest. *Remote Sensing of Environment, 94*, 105-122

Xie, J. (2013). Classification of wetlands using object-oriented method and multi-season remote sensing images in Sanjiang Plain. In: University of Chinese Academy of Sciences (Northeast Institute of Geography and Agroecology)

Xin, Q.C., Broich, M., Suyker, A.E., Yu, L., & Gong, P. (2015). Multi-scale evaluation of light use efficiency in MODIS gross primary productivity for croplands in the Midwestern United States. *Agricultural and Forest Meteorology, 201*, 111-119

Yan, H.M., Fu, Y.L., Xiao, X.M., Huang, H.Q., He, H.L., & Ediger, L. (2009). Modeling gross primary productivity for winter wheat-maize double cropping System using MODIS time series and CO2 eddy flux tower data. *Agriculture Ecosystems & Environment, 129*, 391-400

Yuan, W., Cai, W., Xia, J., Chen, J., Liu, S., Dong, W., Merbold, L., Law, B., Arain, A., Beringer, J., Bernhofer, C., Black, A., Blanken, P.D., Cescatti, A., Chen, Y., Francois, L., Gianelle, D., Janssens, I.A., Jung, M., Kato, T., Kiely, G., Liu, D., Marcolla, B., Montagnani, L., Raschi, A., Roupsard, O., Varlagin, A., & Wohlfahrt, G. (2014). Global comparison of light use efficiency models for simulating terrestrial vegetation gross primary production based on the LaThuile database. *Agricultural and Forest Meteorology, 192–193*, 108-120

Yuan, W.P., Liu, S., Zhou, G.S., Zhou, G.Y., Tieszen, L.L., Baldocchi, D., Bernhofer, C., Gholz, H., Goldstein, A.H., Goulden, M.L., Hollinger, D.Y., Hu, Y., Law, B.E.,

Stoy, P.C., Vesala, T., Wofsy, S.C., & AmeriFlux, C. (2007). Deriving a light use efficiency model from eddy covariance flux data for predicting daily gross primary production across biomes. *Agricultural and Forest Meteorology, 143*, 189-207

Yuan, W.P., Liu, S.G., Yu, G.R., Bonnefond, J.M., Chen, J.Q., Davis, K., Desai, A.R., Goldstein, A.H., Gianelle, D., Rossi, F., Suyker, A.E., & Verma, S.B. (2010). Global estimates of evapotranspiration and gross primary production based on MODIS and global meteorology data. *Remote Sensing of Environment, 114*, 1416-1431

Zeng, N., Yoon, J.H., Marengo, J.A., Subramaniam, A., Nobre, C.A., Mariotti, A., & Neelin, J.D. (2008). Causes and impacts of the 2005 Amazon drought. *Environmental Research Letters, 3*

Zeng, N., Zhao, F., Collatz, G.J., Kalnay, E., Salawitch, R.J., West, T.O., & Guanter, L. (2014). Agricultural Green Revolution as a driver of increasing atmospheric CO2 seasonal amplitude. *Nature, 515*, 394-+

Zhang, F., Chen, J.M., Chen, J., Gough, C.M., Martin, T.A., & Dragoni, D. (2012a). Evaluating spatial and temporal patterns of MODIS GPP over the conterminous U.S. against flux measurements and a process model. *Remote Sensing of Environment, 124*, 717-729

Zhang, F.M., Chen, J.M., Chen, J.Q., Gough, C.M., Martin, T.A., & Dragoni, D. (2012b). Evaluating spatial and temporal patterns of MODIS GPP over the conterminous US against flux measurements and a process model. *Remote Sensing of Environment, 124*, 717-729

Zhang, K., Kimball, J.S., Zhao, M.S., Oechel, W.C., Cassano, J., & Running, S.W. (2007). Sensitivity of pan-Arctic terrestrial net primary productivity simulations to daily surface meteorology from NCEP-NCAR and ERA-40 reanalyses. *Journal of Geophysical Research-Biogeosciences, 112*

Zhang, L., Xiao, J.F., Li, J., Wang, K., Lei, L.P., & Guo, H.D. (2012c). The 2010 spring drought reduced primary productivity in southwestern China. *Environmental Research Letters, 7*

Zhang, M.W., Zhou, Q.B., Chen, Z.X., Liu, J., Zhou, Y., & Cai, C.F. (2008a). Crop discrimination in Northern China with double cropping systems using Fourier analysis of time-series MODIS data. *International Journal of Applied Earth Observation and Geoinformation, 10*, 476-485

Zhang, Q.Y., Cheng, Y.B., Lyapustin, A.I., Wang, Y.J., Xiao, X.M., Suyker, A., Verma, S., Tan, B., & Middleton, E.M. (2014a). Estimation of crop gross primary production (GPP): I. impact of MODIS observation footprint and impact of vegetation BRDF characteristics. *Agricultural and Forest Meteorology, 191*, 51-63

Zhang, Q.Y., Cheng, Y.B., Lyapustin, A.I., Wang, Y.J., Zhang, X.Y., Suyker, A., Verma, S., Shuai, Y.M., & Middleton, E.M. (2015). Estimation of crop gross primary production (GPP): II. Do scaled MODIS vegetation indices improve performance? *Agricultural and Forest Meteorology, 200*, 1-8

Zhang, X., Friedl, M.A., & Schaaf, C.B. (2006). Global vegetation phenology from Moderate Resolution Imaging Spectroradiometer (MODIS): Evaluation of global patterns and comparison with in situ measurements. *Journal of Geophysical Research-Biogeosciences, 111*

Zhang, Y., Guanter, L., Berry, J.A., Joiner, J., van der Tol, C., Huete, A., Gitelson, A., Voigt, M., & Köhler, P. (2014b). Estimation of vegetation photosynthetic capacity from space-based measurements of chlorophyll fluorescence for terrestrial biosphere models. *Global Change Biology, 20*, 3727-3742

Zhang, Y., Xiao, X.M., Jin, C., Dong, J.W., Zhou, S., Wagle, P., Joiner, J., Guanter, L., Zhang, Y.G., Zhang, G.L., Wang, J., & Moore, B. (2016). Consistency between sun-induced chlorophyll fluorescence and gross primary production of vegetation in North America. *Remote Sensing of Environment, (under revision)*

Zhang, Y.Q., Yu, Q., Jiang, J., & Tang, Y.H. (2008b). Calibration of Terra/MODIS gross primary production over an irrigated cropland on the North China Plain and an alpine meadow on the Tibetan Plateau. *Global Change Biology, 14*, 757-767

Zhangcai, Q., Qianlai, Z., & Min, C. (2012). Impacts of land use change due to biofuel crops on carbon balance, bioenergy production, and agricultural yield, in the conterminous United States. *GCB Bioenergy, 4*

Zhao, L., Lee, X.H., & Liu, S.D. (2013a). Correcting surface solar radiation of two data assimilation systems against FLUXNET observations in North America. *Journal of Geophysical Research-Atmospheres, 118*, 9552-9564

Zhao, M., Running, S.W., & Nemani, R.R. (2006). Sensitivity of Moderate Resolution Imaging Spectroradiometer (MODIS) terrestrial primary production to the accuracy of meteorological reanalyses. *Journal of Geophysical Research-Biogeosciences, 111*

Zhao, M.S., & Running, S.W. (2010). Drought-Induced Reduction in Global Terrestrial Net Primary Production from 2000 Through 2009. *Science, 329*, 940-943

Zhao, X., Liang, S.L., Liu, S.H., Yuan, W.P., Xiao, Z.Q., Liu, Q., Cheng, J., Zhang, X.T., Tang, H.R., Zhang, X., Liu, Q., Zhou, G.Q., Xu, S., & Yu, K. (2013b). The Global Land Surface Satellite (GLASS) Remote Sensing Data Processing System and Products. *Remote Sensing, 5*, 2436-2450

Zhong, L., Gong, P., & Biging, G.S. (2014). Efficient corn and soybean mapping with temporal extendability: A multi-year experiment using Landsat imagery. *Remote Sensing of Environment, 140*, 1-13

Zhu, W.Q., Pan, Y.Z., He, H., Yu, D.Y., & Hu, H.B. (2006). Simulation of maximum light use efficiency for some typical vegetation types in China. *Chinese Science Bulletin, 51*, 457-463

Zhu, Z., & Woodcock, C.E. (2012). Object-based cloud and cloud shadow detection in Landsat imagery. *Remote Sensing of Environment, 118*, 83-94

Zhu, Z., Woodcock, C.E., & Olofsson, P. (2012). Continuous monitoring of forest disturbance using all available Landsat imagery. *Remote Sensing of Environment, 122*, 75-91

Zib, B.J., Dong, X.Q., Xi, B.K., & Kennedy, A. (2012). Evaluation and Intercomparison of Cloud Fraction and Radiative Fluxes in Recent Reanalyses over the Arctic Using BSRN Surface Observations. *Journal of Climate, 25*, 2291-2305

Zscheischler, J., Mahecha, M.D., von Buttlar, J., Harmeling, S., Jung, M., Rammig, A., Randerson, J.T., Scholkopf, B., Seneviratne, S.I., Tomelleri, E., Zaehle, S., & Reichstein, M. (2014). A few extreme events dominate global interannual variability in gross primary production. *Environmental Research Letters, 9*